UNIVERSITÀ DEGLI STUDI DI CATANIA

Dottorato di Ricerca in Scienza e Tecnologia dei Materiali - XXVI ciclo

**Salvatore Cosentino**

# *Germanium Nanostructures for Efficient Light Harvesting Devices*

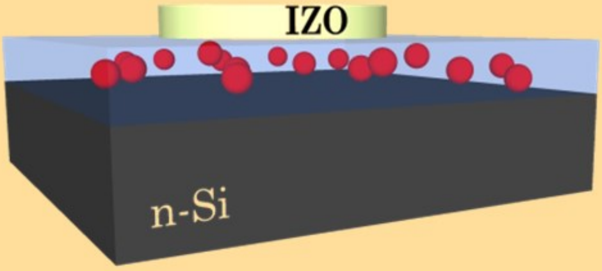

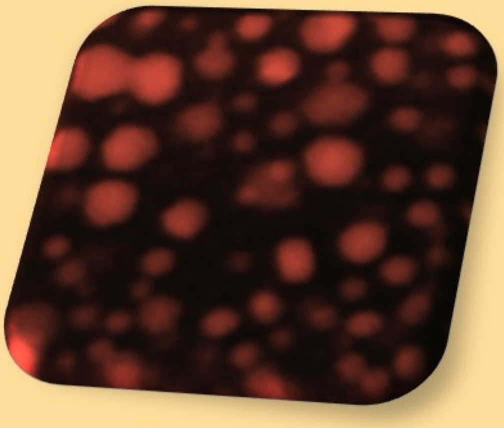

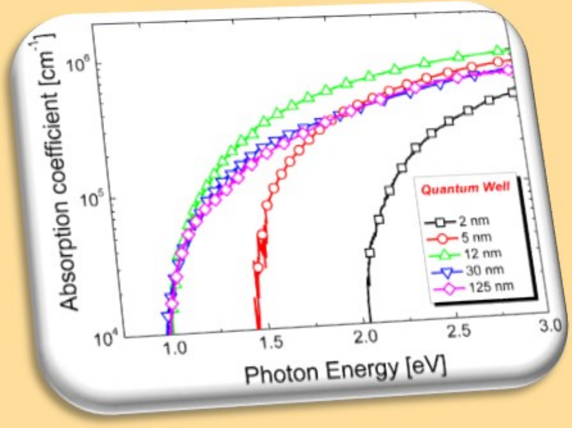

Tesi per il conseguimento del titolo

UNIVERSITÀ DEGLI STUDI DI CATANIA

Dottorato di Ricerca in Scienza e Tecnologia dei Materiali - XXVI ciclo

Salvatore Cosentino

# Germanium Nanostructures for Efficient Light Harvesting Devices

Tutor: Prof. A. Terrasi
Supervisor: Dr. S. Mirabella
Coordinatore: Prof.ssa M.G. Grimaldi

Tesi per il conseguimento del titolo

To my Family

## COVER

**TOP:** *Schematic illustration of a metal-insulating-semiconductor photodetector with an active layer of Ge quantum dots embedded in $SiO_2$. More details can be found within this thesis in section 4.3.*

**LEFT:** *Cross sectional Transmission Electron Microscopy of Ge quantum dots embedded in $SiO_2$ matrix. More details can be found within this thesis in section 3.2.2.*

**RIGHT:** *Absorption spectra of single amorphous Ge quantum wells of different thicknesses. More details can be found within this thesis in section 2.1.1.*

**Germanium Nanostructures for Efficient Light Harvesting Devices**

Salvatore Cosentino

Ph.D. Thesis, University of Catania

Printed in Catania, December 2013

Out of the night that covers me,
Black as the Pit from pole to pole,
I thank whatever gods may be
For my unconquerable soul.

In the fell clutch of circumstance
I have not winced nor cried aloud.
Under the bludgeonings of chance
My head is bloody, but unbowed.

Beyond this place of wrath and tears
Looms but the Horror of the shade,
And yet the menace of the years
Finds, and shall find, me unafraid.

It matters not how strait the gate,
How charged with punishments the scroll.
I am the master of my fate:
I am the captain of my soul.

**Invictus** by William Ernest Henley

# Contents

**Chapter 1**

## Chapter 2

## Chapter 3

**Chapter 4**

# Abstract

The growing World energy demand is setting new challenges toward the use of alternative and green resources as well as for the development of more efficient and low-power consuming devices. Thanks to their unique optical properties, group IV (such as: Si, Ge, C) nanostructures (NS) show promising applications for cheap multi-junction solar cells and, in general, for efficient energy-tunable light harvesting devices. Among them, Ge reveals interesting optical properties due to its quasi-direct bandgap and larger absorption coefficient that make it intrinsically more suitable than Si for what concerns light harvesting applications. Moreover, the larger exciton Bohr radius of Ge (~24 nm) with respect to Si, gives the chance to easily tune the optical properties of Ge NSs by varying their size. However, the properties of Ge NS depends not only by size through quantum confinement effects, but many other parameters can concur in controlling their optical behavior, especially for what concerns the optical bandgap.

Discerning the role of these parameters and controlling their effects in the light absorption process contains not only a fundamental research theme, but represents a key-factor toward the implementation of Ge NS in any type of light harvesting device. For this reason, this thesis reports a detailed study on the synthesis, structural and optical properties of Ge nanostructures (quantum well, QW, or quantum dots, QDs) embedded in a dielectric matrix as well as the investigations of photo-conduction properties in prototypal light harvesting devices employing Ge NSs. Although the optical behavior of a single amorphous Ge QW can be fully modeled within the quantum confinement effect theory, this situation dramatically changes for a 3-dimensional confinement, as in an ensemble of QDs. In this last case, the effects of quantum confinement can be hidden or weakened by other parameters, such as: QD spacing and distribution, type and quality of the hosting matrix and abundance of defects related to the synthesis technique used. For this reason, we will investigate in detail the synthesis and optical properties of Ge QDs embedded in $SiO_2$ or $Si_3N_4$ matrices, grown after thermal annealing of Ge-rich films synthesized by co-sputtering deposition; plasma enhanced chemical vapour deposition (PECVD) and ion implantation. We will give evidences of the strength of quantum confinement effects occurring in these systems as well as discerning the contributions coming from other concomitant effects. Finally, we will demonstrate that Ge nanostructures can be effectively used as active absorber and conductive medium in light harvesting devices. In particular, we will report on the spectral response of metal-insulating-semiconductor (MIS) photodetectors employing a single amorphous Ge QW or a packed array of Ge QDs as active light sensitizer and conductive medium. Both types of NSs have a fundamental role on the performances of these prototypal devices, demonstrating the large potentiality of such nanostructures for the development of high efficiency photodetectors and low cost solar cells.

# Chapter 1

# Nano for Energy

## 1.1 Global Energy demand: The TW challenge

The Energy issue has always dealt a leading position in the economy and development of human society. The energy consumption of a country is directly related to both its economic output and the individual quality of life of its citizens. Both population growth and the desire to maintain and increase our current standards of living result in an increased energy consumption. In fact, the current global primary energy consumption per year is estimated to be of about 16 TWy (corresponding to ~ $1.45 \cdot 10^{5} TWh = 5.41 \cdot 10^{20} J$), with a yearly growth rate of about 3% that will led to a doubling of energy demand in next twenty years, as reported in figure 1.1 [1], [2].

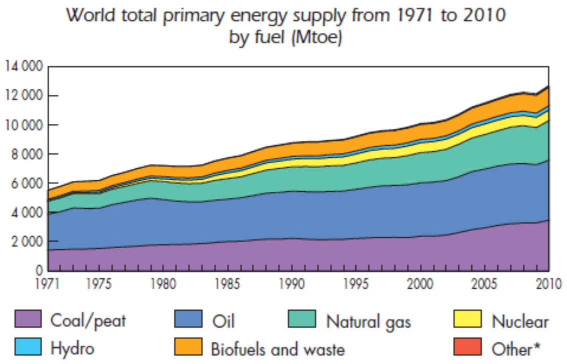

**Fig 1.1:** World primary energy consumption by fuel type in Mtoe (million tonnes of oil equivalent) (from ref. [1], [2]. The category "Other" includes geothermal, solar, wind and heat. Note that 1 Mtoe is equivalent to $4.476 \times 10^{16}$ J = 12 TWh)

Feeding, clothing and housing a continuously growing world population will be a significant challenge in terms of energy sustainability. In fact, the growing global energy demand, combined with the durability problem of supplying from fossil fuels, is setting new economic, politic and environmental problems. Today, almost 90% of the global energy is produced by burning coal, oil, natural gas or using nuclear plants [1]. These traditional technologies have strong potential impact on environment, both for the global growing threat of pollution and for the potential risk for the people and the economy of the affected areas (e.g., the Chernobyl and Fukushima nuclear disaster of 1986 and 2011 respectively, the Gulf of Mexico oil spill of 2010). Moreover, the rapid increase of the energy price, also favoured by financial speculations, has been one of the main reason of the recent international economic crisis. Last but not the least, the large quantities of carbon dioxide released in the atmosphere by the consuming of fossil fuels are causing strong consequences for the climate balance of our planet.

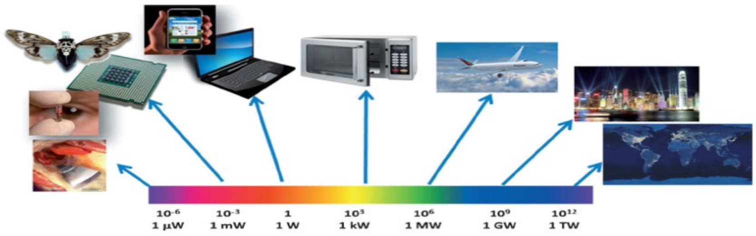

**Figure 1.2:** Power requirements for different applications [3].

An interesting marker of the growing energy demand is given by the rapid growth of personal and mobile electronics devices, which profoundly entered in our daily life. Individually, the power consumption of these technologies is rather low: from some $\mu W$ to $W$ per single electronic device, as shown in figure 1.2. However, the number of such devices, integrated over the entire world population consumers, is huge and is expected to increase with the standards of human living. Moreover, the powering of most electronic devices still relies on rechargeable batteries. Of course, the amount of required batteries increases in proportion with the increase of the number and density of electronic devices. This may result in challenges for recycling and replacement of the batteries (usually made of environmentally unfriendly and cost-effective products) as well as an increased energy consumption.

Therefore, our future quality of life greatly depends on how successful we are in developing a sustainable energy technology that can meet our future energy needs. The development of novel materials and innovative technologies to replace the traditional oil and carbon fuels will be a milestone in the future research and political agenda. In this scenario, solar energy could be a viable and environmentally conscious solution to the growing global demand for energy. Moreover, also the development of high-efficiency and low-power consuming devices is highly desired for a better energy consumption. For this reason, a focus of active research in this field is the exploration and the study of new materials to enhance the performance of more efficient energy harvesting devices.

### 1.1.1 Solar Energy

Energy from the Sun is the basis of life on Earth. Both active (i.e. solar cells) or passive (i.e. green houses) solar energy harvesting have always been close to human development. Solar energy is by far the most abundant and sustainable source for Earth. Figure 1.3 compares the current annual energy consumption of the world to the known planetary reserves of fossil fuels and nuclear resources and to the yearly potential of the renewable alternatives [4]. The solar resource is orders of magnitude larger than all the others combined. More energy is provided to the Earth by sunlight irradiation within one hour than is consumed by human society globally in one year.

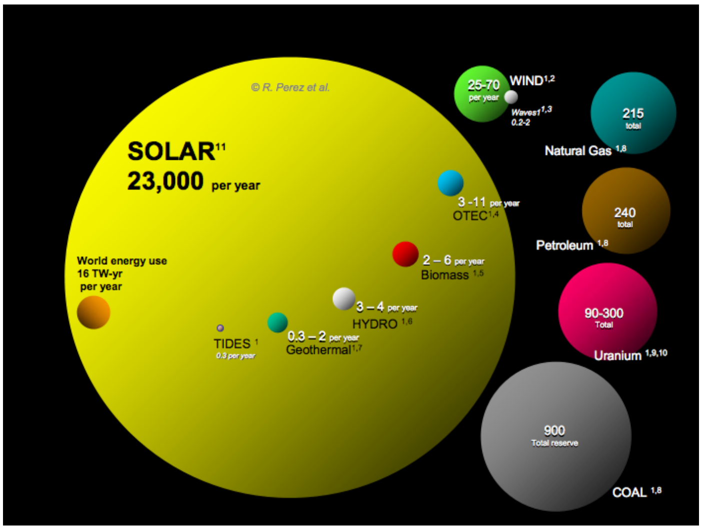

**Figure 1.3:** Comparing finite and renewable planetary energy reserves (Terawatt-years). Total recoverable reserves are shown for the finite resources. Yearly potential is shown for the renewable sources [4].

The energy output from the Sun that reaches the Earth can be calculated by applying some fundamentals rules of Physics. As shown on Figure 1.4, the spectral irradiance *I*(λ) of Sun outside the Earth's atmosphere can be approximated to the spectral thermal radiation of a blackbody emitter held at a temperature *T* of about 5800 *K*, given by Planck's formula:

$$I(\lambda)=2\pi\frac{hc^{2}}{\lambda^{5}\cdot\left(e^{\frac{hc}{k_BT}}-1\right)} \tag{1.1}$$

where $h$ is the Planck's constant, $c$ is the speed of light and $k_B$ is the Boltzmann constant. The terrestrial atmosphere attenuates the sunlight, mainly because of the water-vapor and ozone absorption or by scattering phenomena. The degree to which the atmosphere affects the sunlight is quantified by the air mass unit, defined as the secant between the sun and the zenith ($AM \approx 1/\cos\theta$). Thus, AM0 represents the solar spectrum outside the earth's atmosphere, while AM1.5 (commonly used as a standard reference for solar cell efficiency) represents the sunlight at the Earth's surface when the sun is at $\theta = 48.2^\circ$ from zenith.

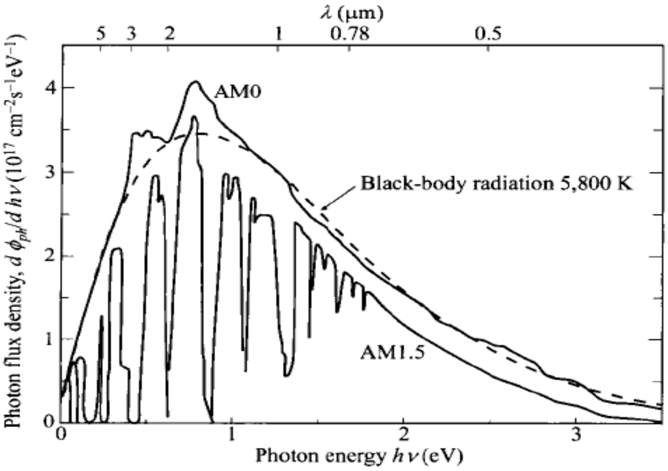

**Figure 1.4:** Solar spectrum in photon flux density per photon energy for AM0 and AM1.5 conditions, together with the black body radiation spectrum at 5800 *K* [5].

Integrating $I(\lambda)$ over all wavelengths gives a power density of about 63.3 MWm$^{-2}$ [2]. Considering that the intensity of electromagnetic waves decreases with the inverse square of the distance from the source, we can estimate an irradiance of as 1327 Wm$^{-2}$ reaching the Earth's atmosphere. From this value, one can estimate an average of about 35000 TW arriving just above the Earth atmosphere. This is an enormous amount of energy, even if we take into account of the attenuations due to the scattering and optical absorption of the incident light by the atmosphere, which reduce the incident energy to around 23000 TWy. Thus, the exploitation of even a very small fraction of the Earth's solar potential could meet the global energy demands. Sunlight-electricity conversion devices exploiting photovoltaic (PV) effect have experienced a rapid development in the past few decades. PV market has shown annual growth rates between 40% and 90% since 2000 [6], with strong similarities with the Moore's law for the integrated circuits. In sharp contrast to the huge amount of energy we receive from the sun, only less than 0.1% of the total energy production (about 80 GW by the end of 2012) comes from the sunlight conversion [6]. This is mainly due to the fact that the existing PV technologies have yet not been able to produce electricity at a comparable price with conventional generation methods. In this regard, a lot of efforts have been invested toward development of PV technologies that operate with enhanced efficiency and lower cost. In this scenario a key-role is represented by the research on new materials and optimized device structure to increase the performances and reduce the fabrication costs of these devices.

### 1.1.2 Sunlight-energy conversion

As a result of a photoelectric-based phenomenon, the exploitation of solar energy in PV devices relies on two basic steps: photon absorption and photo-carrier collection. In nearly all types of solar cells the absorber medium is a semiconductor. Figure 1.5 illustrates the principle of a conventional single *p-n* junction solar cell. Incident photons that have energies above the semiconductor bandgap ($E_g$) are absorbed, creating electron-hole pairs. These electron-hole pairs are separated and collected at the output of the PV device through the action of an electric field, giving rise to an external power. Such electric field is usually created by a *p-n* junction (connection of *p*- and *n*-type doped semiconductor, figure 1.5) or Schottky junction (connection of a metal and a doped semiconductor).

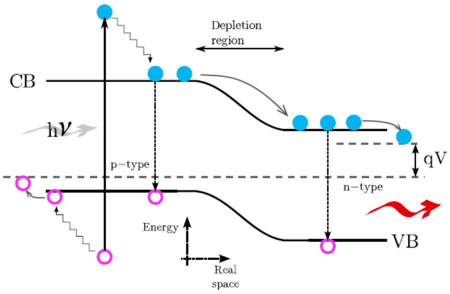

**Figure 1.5:** Schematic diagram of a conventional single-junction semiconductor solar cell. Absorbed light with photon energies greater than the bandgap produces carriers, electrons and holes. Loss processes are: non-absorption of below-bandgap photons, heat losses, and radiative recombination. Adapted from ref. [7].

A conventional *p-n* junction solar cell is assumed to have a ideal diode *I-V* characteristics. When such a device is illuminated, the total *I-V* characteristics can be written as a summation of the dark diode current and the photocurrent $I_L$ due to generated electron-hole pairs.

$$I = I_s\left[\exp\left(\frac{qV}{kT}\right) - 1\right] - I_L \tag{1.2}$$

where $I_s$ is the diode saturation current [5].

From eq. (1.2), we obtain the open-circuit voltage by setting $I = 0$, while the short-circuit current $I_{sc}$ represents the photocurrent extracted at $V = 0$. The *I-V* characteristic under illumination passes through the fourth quadrant and, therefore, power can be extracted from the device to a load. We can define the quantities $I_m$ and $V_m$ that correspond to the current and the voltage that maximize the power output $P_m = I_m V_m$. In this regard, the ideal conversion efficiency of a solar cell is defined as the ratio of the maximum power output to the incident light power Pin: $\eta = P_m / P_{in}$.

Large part of the current photovoltaic technology utilizes single *p-n* junctions of mono- or poly-crystalline bulk silicon or thin films of amorphous silicon, cadmium telluride (CdTe), or copper indium gallium selenide (CIS) as active absorber. The semiconductor material has to be able to absorb a large part of the solar spectrum, which is primarily determined by its bandgap, and at the same time guarantee an efficient photo-carrier extraction. Nevertheless, the requirements to optimize both optical absorption and carrier collection can be in conflict. For example, in a standard *p-n* junction solar cell, a thick material (~*μm*) is needed to achieve a consistent fraction of photon absorbed. However, this can lead to a lower photo-carrier collection because of the increased path for minority carriers and the resulting larger probability of electron-hole recombination, and vice versa. In principle, a thin active layer (~100 nm thick) of a material with high absorption coefficient (>$10^5$ $cm^{-1}$) would be largely desired to reduce the production costs and maintain high photo-carrier collection capability.

Indeed, the sunlight-electricity conversion process in *p-n* junction solar cells suffers of some intrinsic losses that strongly limit the efficiency in these systems. As illustrated in figure 1.5, the primary losses in a *p-n* junction solar cell are: photons with energy below the semiconductor bandgap do not contribute to electrical current (*sub-bandgap losses*); *thermalization losses* of photons with energy exceeding the bandgap and *radiative recombination* of electron-hole pairs. Considering these limitations, the maximum thermodynamic efficiency for single bandgap devices is about 31%, according to the detailed balance limit of Shockley–Queisser (SQ) [8].

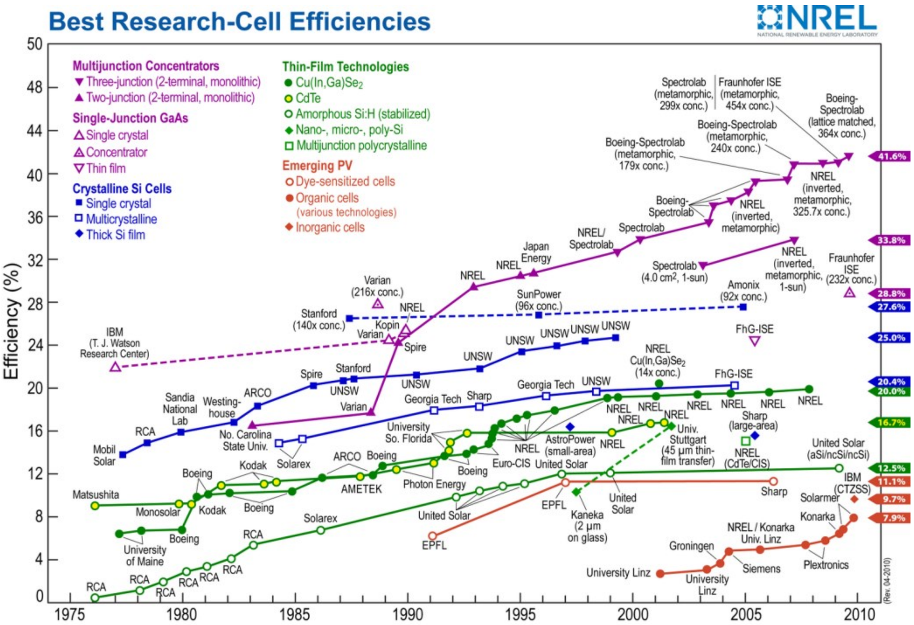

**Figure 1.6:** Yearly trend of solar cells record efficiency. Different colors and symbols define the different generations and technologies [9].

Figure 1.6 shows the evolution of efficiency for various solar cell technologies over the last three decades. Up to date, the highest 1-sun efficiency of a single crystal (sc) sc-Si cells is ~25%, while that of polycrystalline Si (poly-Si) cells is 20.4%. The record efficiency for all solar cell technologies is held at 41.6% by triple-junction solar cell. This cell stacks three p-n junctions made of $Ga_xIn_{1-x}As$ or $Ga_yIn_{1-y}P$ with different compositions. Each junction has a different band gap and is responsible for light absorption in a certain portion of the solar spectrum. The efficiency is measured with a concentrator under 326 Suns. Under one Sun, the efficiency of this triple-junction cell is 33.8%. Besides wafer Si, several thin-film solar cell technologies have been commercialized, including Si in either amorphous (a-Si) or microcrystalline ($\mu c$-Si) form and metal chalcogenides

(CdTe and $CuIn_xGa_{1-x}Se_2$ (CIGS)). Their record efficiencies range between 12% and 20%.

While the progress in the efficiencies of these solar cells has been remarkable, new approaches are needed in order to boost the performance of these devices beyond the SQ limit. Closing (and overcoming) this efficiency gap is the main subject of ongoing PV research. In this regard, new approaches in the light absorption management and in the optimization of the photocarrier extraction would be largely desired for the development of more efficient solar cells.

### 1.1.3 New approaches for efficient light conversion

As described previously, one of the main limit of current PV technology are intrinsically connected with the capability of the material to absorb the incident light. In this regard, several possible strategies have been put forward to reduce sub-bandgap and thermalization losses and achieve higher conversion efficiencies.

- In *multi-junction* approach (figure 1.7a), the use of several band-gap materials allow to convert different portions of the spectrum, reducing the thermalization and the sub-bandgap losses. Multi-junction solar cells are made in a series- or parallel- connected architecture, with each sub-cell acting as a ‘filter’ and absorbing only above-energy bandgap photons. The detailed balance limit for optimized multi-junction cells under 1 Sun illumination shifts from the SQ limit to 42%, 49% and 53% for 2, 3, and 4 cells, respectively. For the hypothetical system with infinite number of sub-cells the limit efficiency is 68.2%. Triple-junction solar cells made of

GaInP/GaAs/InGaAs or GaInP/GaInAs/Ge already demonstrated record conversion efficiencies of over 40%, as shown in figure 1.6) [9]. However, the disadvantage of this approach relies on the complexity and the high cost of the structure that limit its applicability on large scale.

- In *intermediate band* (IB) approach (figure 1.7b), sub-bandgap energy photons can be absorbed by intermediate energy levels located in the forbidden gap. In this way, sub-bandgap energy photons are absorbed through transitions from the valence band (v.b.) to the intermediate band (IB) and from the IB to the conduction band (c.b.), enabling, at least in principle, IBSCs to achieve both high current and high voltage. The theoretical limiting efficiency of IB solar cells is 63% under 1 Sun isotropic illumination [7]. The principal ways to obtain IB is by introducing in the host semiconductor extended defects, impurities, mismatched alloys, or superlattices of quantum dots. However, the main issue of this approach is achieving a strong absorption from IB without increasing non-radiative recombination processes. In addition, IB must be electronically separated from valence and conduction bands, otherwise the photo-voltage would be reduced.

- In *carrier multiplication* approach (figure 1.7c), one high energy photon excites two or more lower energy excitons. Such an inverse Auger process is usually called *multiple exciton generation* (MEG) and has been observed in bulk semiconductors (such as Si-Ge alloys) as well as in quantum dots (PbSe, CdTe, CdSe, Si) [11][12][14]. This process is inefficient and not exploitable in bulk semiconductors because the MEG rate is much slower than radiative recombination process and also because high energy photons lying outside the solar spectrum ($E > 3.5$ eV) are needed to create extra carriers in bulk semiconductors. It was proposed that MEG process might be more efficient in quantum dots made from Si, PbSe, InAs and CdSe. Numerous experiments have confirmed the existence of MEG in these systems [11], [12][14]. However, multi-excitons tend to recombine very fast (*ps* time scale), limiting the carrier extraction process in a future device.

- In *wavelength conversion* approach (figure 1.7d), several low energy photons are converted into one high-energy photon (*up-conversion*) or, alternatively, one high-energy photon is divided into several low-energy photons (*down conversion*). These approaches enable to reduce losses due to transmitted light or thermalization processes, respectively. The incident spectrum can also be modified by *down shifting* photon process, where one high-energy photon is absorbed by a luminescent center and then re-emitted at a longer wavelength. Most data on this approach have been achieved using rare-earth ions such as $Er^{3+}$, $Yb^{3+}$, $Eu^{3+}$ based compounds [15], [16]. The disadvantage of this approach relies on the low optical cross section of radiative transitions and on the relatively narrow bands of absorption as well as the very high cost of rare-earth elements.

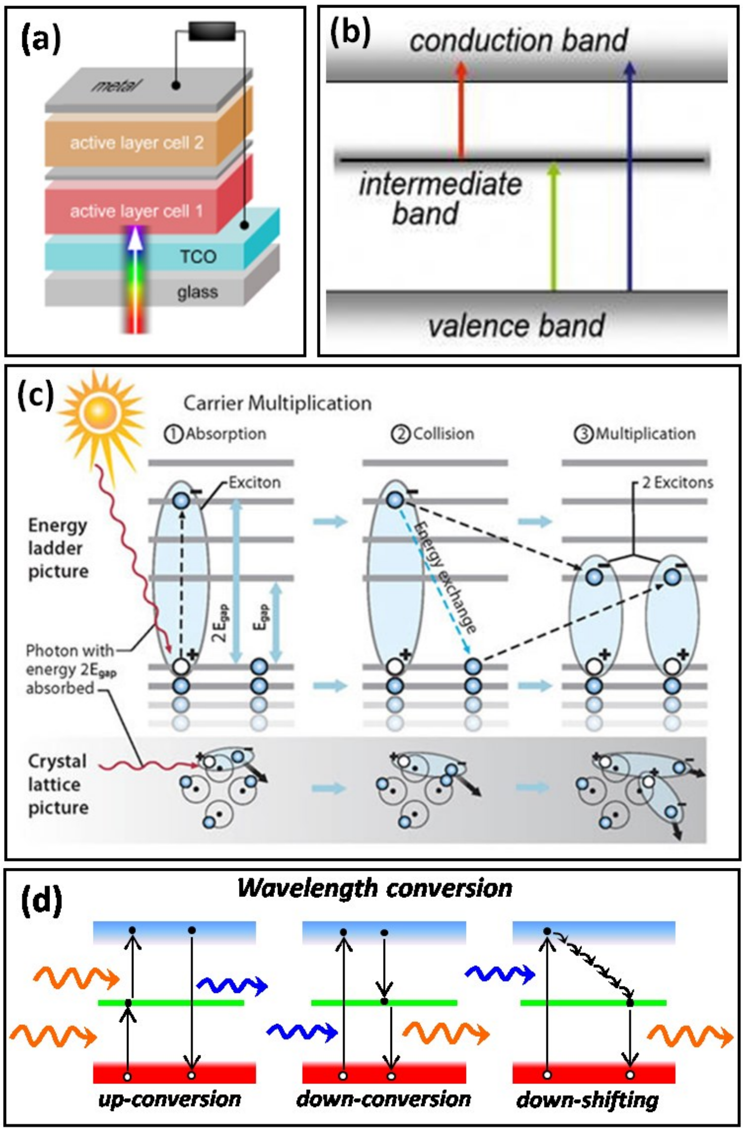

**Figure 1.7:** Main approaches for new generation PV cells: (a) Multi-junction; (b) intermediate-band solar cell; (c) Carrier multiplication process (called impact ionization in bulk semiconductor); (d) wavelength conversion for “shaping” of the incoming solar radiation.

As evident from the above examples, the improvement of the performances in light harvesting devices largely relies both on the optimization of photon absorption and photo-carrier extraction mechanisms. However, the simultaneous optimization of both processes is non trivial for solar cells based on conventional structures, also for the needing to maintain low fabrication costs. Efficiency and cost can be considered as the two sides of the same coin. Any efficiency improvement is often accompanied by additional costs, so it has to be done in a cost-effective manner.

In this regard, the exploitation of novel physical properties in *"new materials"* could meet the requirements of optimized light-conversion efficiency and low production costs. In particular, the usage of semiconductor nanostructures and the exploitation of their unique optical and electrical properties have been proposed as possible solution not only for boosting energy-conversion efficiency beyond the actual SQ limit of conventional solar cells, but also for the development of novel high efficiency optoelectronic devices and light harvesters.

## 1.2 Exploiting Quantum Confinement Effects

The field of Nanotechnology has seen an extraordinary explosion of interest in the few decades, particularly due to the possibility to exploit the fundamental rule of quantum mechanism in many applications. The seminal event of the Nanotechnology era is considered to be the famous talk "There is Plenty of Room at the Bottom" given by the physicist R. Feynman at the annual meeting of the American Physical Society at Caltech on 29th December, 1959 [17]:

> *"Now, the name of this talk is "There is Plenty of Room at the Bottom" – not just "There is Room at the Bottom." What I have demonstrated is that there is room – that you can decrease the size of things in a practical way. I now want to show that there is plenty of room. […] Atoms on a small scale behave like nothing on a large scale, for they satisfy the laws of quantum mechanics. So, as we go down and fiddle around with the atoms down there, we are working with different laws, and we can expect to do different things. […] At the atomic level, we have new kinds of forces and new kinds of possibilities, new kinds of effects. […] The principles of physics, as far as I can see, do not speak against the possibility of maneuvering things atom by atom. It is not an attempt to violate any laws; it is something, in principle, that can be done; but in practice, it has not been done because we are too big."*

The study and application of nanostructures have the interest of many generation of scientists up to now, giving origin to what it is now known as nanotechnology. Due to strong changes of structural, electrical, optical and chemical properties of materials at the nanoscale length, nanotechnology opened the way to a new era in many fields, most of which have a huge impact on our current the daily life, from nano-optoelectronic [18] [19] nano-biology [21], chemical sensors [20] to new concepts for high efficient light harvesters and solar cells [22] - [24].

### 1.2.1 Playing with Quantum Confinement

A nanostructure (NS) is, for definition, any material which spatial dimensions are confined to the nanometer scale (1 - 10 nm). In the following paragraphs, we will refer to NS based on semiconductor materials. If the dimension of the system becomes comparable or smaller than the Bohr radius $r_B$ of charge carriers ($r_B = a_0 \varepsilon / m^*$, where $\varepsilon$ is the dielectric constant and $m^*$ the reduced mass of carriers), the carries "feel" the confinement due to the boundaries of the material and are said to be confined. This phenomenon, which is known as *quantum confinement effect* (QCE), dramatically changes the valence and conduction bands of the system [25]. As drawn in Figure 1.8 (a), when the carriers are spatially confined in one dimension the system is defined as quantum well (QW), a two dimension-confinement produces a quantum wire (Q-wire), while a confinement in all the three dimensions confinement structure is defined as quantum dot (QD). Nanostructures can be successfully modeled as a particle in a box model system by considering a nanometer size inclusion embedded in an insulating matrix with a potential barrier *V*, as shown in Figure 1.8(b).

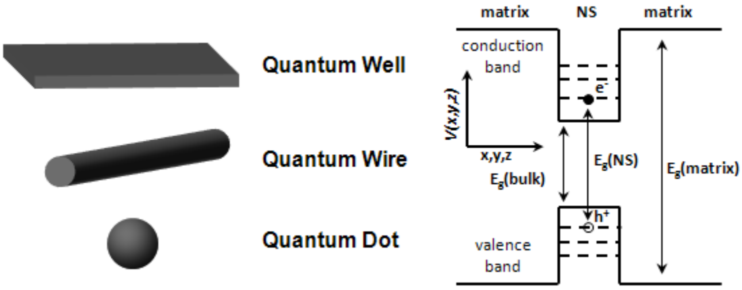

**Figure 1.8: (a)** Schematic representation of quantum wells, wires and dots. (b) Potential well formed in any dimension (x, y, or z) in the conduction and valence bands. The energy levels of the excited carriers (electrons and holes) become quantized due to the finite size of the nanostructure.

One of the most important property of a nanostructure is that by lowering the dimensionality, the energy levels of the systems collapse from continuous energy bands, typical of bulk materials, into discrete energy levels. In particular, the density of states (DOS) and the energy levels for the different degrees of quantization are described by the following equations, valid in the case of an infinite potential barrier *V*:

$$\rho_{bulk}(E)=\frac{1}{\pi^2}\left(\frac{m^*}{\hbar^2}\right)^{3/2}\sqrt{2E}\,; \qquad E_{bulk}(k)=\frac{\hbar^2k^2}{2m^*}$$

$$\rho_{QW}(E)=\frac{m^*}{\pi\hbar^2}\sum_{n_x}\Theta\left(E-E_{n_x}\right); \qquad E_n\left(k_xk_y\right)=\frac{\pi^2\hbar^2n^2}{2m^*L_z^2}+\frac{\hbar^2\left(k_x^2+k_y^2\right)}{2m^*} \qquad (1.3)$$

$$\rho_{Q-Wire}(E)=\frac{1}{\pi\hbar}\sum_{n_x,n_y}\left(E-E_{n_x,}\right)^{-1/2}; \qquad E_{n,m}\left(k_x\right)=\frac{\pi^2\hbar^2}{2m^*}\left(\frac{n^2}{L_z^2}+\frac{m^2}{L_y^2}\right)+\frac{\hbar^2k_x^2}{2m^*}$$

$$\rho_{QD}(E)=\frac{1}{\pi\hbar}\sum_{n_x,n_y,n_z}\delta\left(E-E_{n_x,n_y,n_z}\right); \qquad E_{n,m,l}=\frac{\pi^2\hbar^2}{2m^*}\left(\frac{n^2}{L_z^2}+\frac{m^2}{L_y^2}+\frac{l^2}{L_x^2}\right)$$

where $k_i$ *is the momentum vector*, $\Theta(E)$ is the step function, $L_i$ and $E_{ni}$ (with *i=x,y,z*) are respectively the system dimensions and the quantized energy levels along the directions of confinement, while $n$, $m$, $l \in N$ are the quantum numbers. The energy values in equations (1.3) are offset by the bandgap energy value of the bulk semiconductor. A plot of the DOS for the different degrees of confinement is shown in Figure 1.9, considering Si as material ($m^*$=1.08) and a confinement dimension $L_i$ of 2 nm [26]. The decrease of system dimensionality strongly modifies the DOS and the energy occupation levels. In particular, more discrete and energy-spaced states can be found as the degree of confinement gets higher.

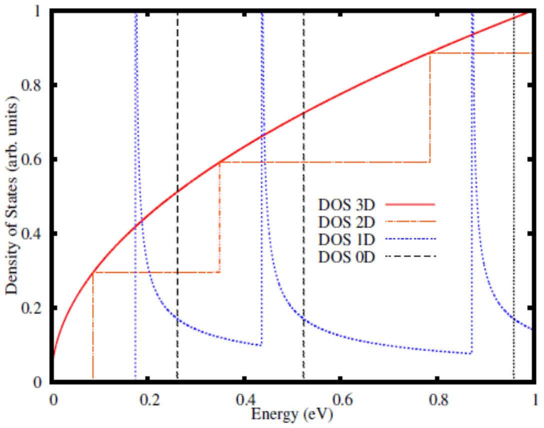

**Figure 1.9:** Plot of the DOS for a bulk (3D) or QW (2D), Q-Wire (1D) and QD (0D) Si structures [26].

More generally, the bandgap $E_g$ of a nanostructure (defined as difference between the lowest unoccupied level in *c.b.* and the highest occupied level in *v.b.*) along the confinement direction can be modeled within the effective mass approach (EMA) theory by the following relation [25]:

$$E_g(NS) = E_g(bulk) + \frac{\pi^2\hbar^2}{2m^*L^2} \tag{1.4}$$

where $E_g(bulk)$ is the bandgap of the unconfined material and $A = \frac{\pi^2\hbar^2}{2m^*}$ is the confinement parameter. Eq. (1.4) is a simplified formula of the actual energy gap of a NS, since does not take in account of the corrective factors due, for example, to the electrostatic Coulomb interaction between electron and hole or the energy level splitting caused by the spin-orbit interaction. However, the magnitude of such factors usually produces variations from the values obtained by using Eq. (1.4) of the order of 10 - 50 meV. Eq. (1.4) shows that the bandgap of a NS is increased with respect to the bulk material by a quantity which is inversely proportional to the square of its size $L$ and to the effective mass of the electron-hole pair $m^*$. In addition, the value of $A$ is larger as more reduced the system dimensionality is, giving rise to a larger tuning of the band-gap with the size $L$. Moreover, Eq. (1.4) is valid in the case of an infinite confining barrier potential. In a real dielectric matrix with a finite barrier height $V_0$, the value of $E_g$ given in Eq. (1.4) is reduced by the factor $\left[1+\frac{\hbar}{r\sqrt{2m^*\cdot V_0}}\right]^2$ [27]. Hence, lower potential barriers reduce the effectiveness of quantum confinement.

The gap tailoring with NS size is one of the most important and potentially useful properties of a nanostructure, in particular for what concerns the light management in future optoelectronic devices and light harvesters. One of the most famous example of a light harvesting device based on the exploitation of QCE is the "*all Si tandem solar cell*", proposed by Green et al. [27], [28]. This solar cell consists in a multiple stack of QD-based cells where the $E_g$ of each sub-cell is tuned with the QD size. Such a type of solar cell gives the possibility to absorb a larger portion of the solar spectrum, as in multi-junction solar cells, but using just one type of material with a potential high reduction of production costs. Actually, such a band-gap engineering can be performed not only by varying the NS size, but also playing with other parameters, like: the height of the confinement barriers where NS are embedded, the degree of confinement, the use different materials or alloys. As an example, Figure 1.10 shows the theoretical values of bandgap (calculated by using the values of $A$ given in ref. [29]) for Si or Ge NS and the role played by the NS size, degree of confinement and embedding matrix. All these parameters strongly affect the effectiveness of the QCE occurring at the nanoscale, giving the chance to span more or less gently the optical band-gap over the entire UV-NIR range.

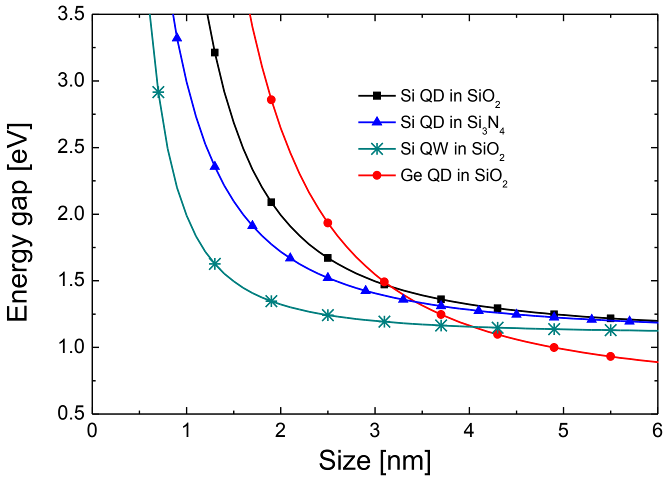

**Figure 1.10:** Theoretical size-dependent shift of the optical band-gap for Si and Ge NS calculated by using the EMA relationship in eq. 1.4.

This means that, starting from a bulk system and playing with QCE, is possible to “create” totally new materials and finely engineer their optical properties. Such a possibility opens a new route toward the optimization of light management in novel nanostructure-based optoelectronics: from light emitting devices operating at telecommunication wavelengths to energy tunable light harvesters and multi-junction solar cells.

### 1.2.2 Beyond bandgap tuning

Besides the band-gap tailoring due to QCE, other important effects can lead to an increased light harvesting and improved performances in NS-based devices in respect to bulk systems. First of all, the reduction of the system dimensions leads also to the breaking of the ***k***-conservation rule for optical transitions. This effect is a direct consequence of the Heisenberg uncertainty relation. The confinement of electron-hole pairs in the real space causes a spread-out in the momentum space of their electronic wavefunction, as shown in figure 1.11 for the case of Si QW [26]. As the confinement dimension $L_x$ is reduced, the dispersion in momentum space is increased, resulting in a larger overlap of the electron-hole wavefunctions. This, in turn, leads to an increased optical transition probability between electron and hole states. This effect is particularly important for indirect gap materials, such as Si or Ge. In this kind of systems optical absorption/emission requires phonon scattering in order to maintain momentum conservation. Such a three bodies event (electron, hole and phonon) is significantly less probable than a direct band-to-band transition and result in a low optical transition probability, typical of indirect-gap bulk materials. However, due to the breaking of ***k***-selection rule, optical transitions can happen without the assistance of phonons in NS, which implies an increased probability of radiative transitions.

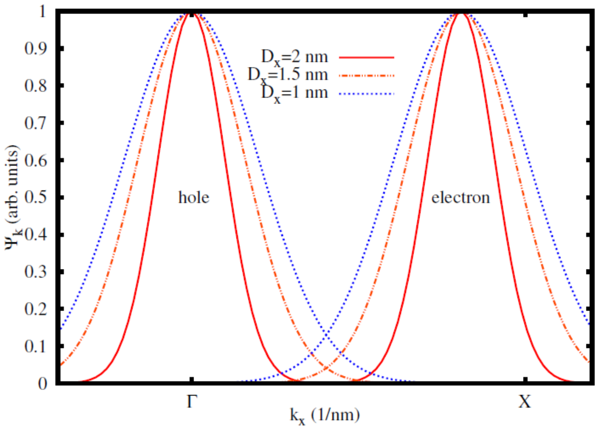

**Figure 1.11:** Plot of a Gaussian envelope function for a single confinement direction in ***k***-space with an electron centred at 0.8 × X-point and a hole at the Γ-point in the Brillouin zone for Si. The plot is not normalized and is shown for three different confinement dimensions, $L_x$, [26].

Therefore, the carrier confinement in NS produces also an increase of the oscillator strength of the optical transitions. This is because the transition probability depends on the coupling between states in the conduction (*c*) and valence (*v*) bands through the dipole matrix element: $\left|\left\langle v\middle|\vec{p}\middle|c\right\rangle\right|^2$. Such a quantity increases as the dimension of the system is reduced, due to the larger wavefunction overlap of electron-hole pair, as depicted in Figure 1.11 [26]. A detailed theoretical and experimental discussion of the enhanced oscillator strength occurring in NS will be given in chapter 2.

Another important effect derived from the overlapping of confined levels in NS is the formation of minibands in closely packed array of NS. Such effect has been extensively studied for application in IR photodetectors, resonant tunneling diodes, as well as intermediate band solar cells [30] - [31][32]. In particular, the coupling among quantum dots leads to a splitting of the quantized carrier energy levels of single dots and formation of three-dimensional minibands. Very recently, Hu et al. demonstrated that the formation of minibands in Si QD superlattices (QDS) embedded in SiO2 or SiC strongly enhances both optical and electrical collection [33]. As shown in figure 1.12 (a), the lower band-offset between QD and embedding matrix increases the wavefunction overlapping between adjacent QDs, inducing additional optical transitions [31], [33]. In addition, the classic quantum confinement effect provide the possibility to further engineering the electronic band structure of this QD-based material by changing QD size, QD-QD distance or barrier height. As shown in figure 1.12 (b) and (c), miniband energy position decreases inverse-squarely with increasing size of QDs, while the inter-dot spacing affects the miniband width (figure 1.12d).

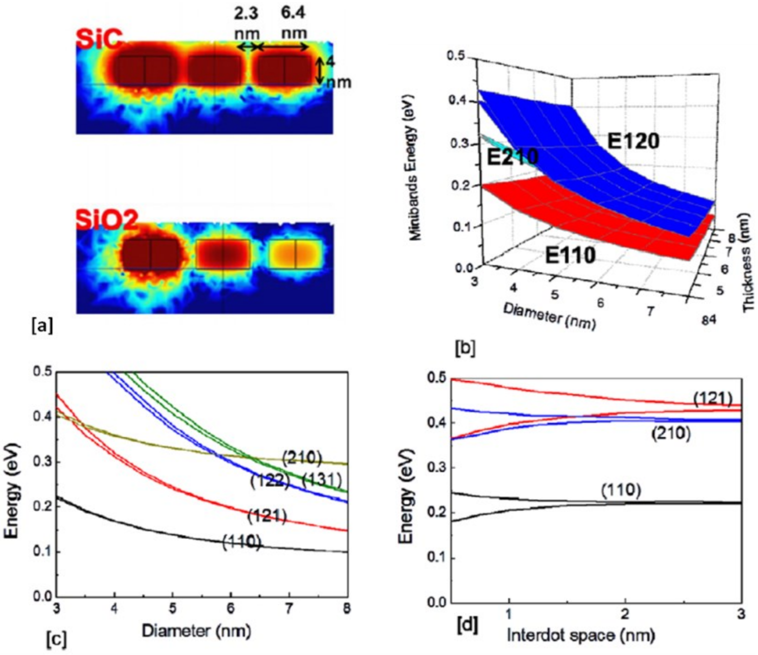

**Figure 1.12:** (a) Ground-state electron wavefunction distribution in the Si ND superlattice embedded in a SiC matrix and $SiO_2$ matrix. (b) Systematic miniband engineering diagram in Si QDs embedded in the SiC matrix. Minibands dependence on (c) Si QD diameter and (d) inter-dot space distance for different quantum numbers. Adapted from ref. [33].

Therefore, the usage of nanostructured materials allows not only to properly engineer the bandgap via QCE, but also enables the chance to overcome the current optoelectronic limitations of bulk Si and Ge semiconductors and to strongly enhance the light absorption/emission process in these materials. Thus, the exploitation of the optical and electronic properties of nanostructures could open a route for the development of high-performance optoelectronic and light harvesting devices.

In this regard, a key-factor toward an easier implementation of nanostructures in novel devices is the compatibility with the current Si technology. For this reasons, a lot of efforts among scientific community have regarded the investigation of the structural and optoelectronic properties of group IV materials (such as Si, Ge, C). While a lot of research exists on Si NS ([34] and references therein), Ge NS have been often underrated because of the lower abundance, higher costs and poor oxide quality of the bulk Ge. However, Ge evidence even better potentiality than Si at the nanoscale, in particular for what concern the bandgap tuning and the capability to absorb light. In the following paragraphs, the main properties of Ge will be shown as well as the state of the art regarding the exploitation of the optical properties of Ge NS in novel optoelectronic and light harvesting devices

## 1.3 Germanium: a promising material for light harvesting

Germanium (Ge) played a primary role since the beginning of the solid state electronics age. The first transistor, invented at Bell Laboratories in 1947 by William Shockley, John Bardeen and Walter Brattain, was fabricated on crystalline Ge substrate [35]. However, the usage of such material in microelectronic industry has been limited only to some niche markets. This is historically due to the poor quality and high instability of the Ge oxide ($GeO_2$) that limited its use in complementary-metal-oxide-semiconductor (CMOS) technology in favor of Si. In addition, another large drawback regards the material availability. In contrast to Si, the second most abundant element on Earth’s crust (27.7%), Ge is pretty rare and widely dispersed (~6.7 parts per million [36]). For these reasons, a large-scale use of bulk Ge in microelectronic industry would be very challenging and cost-effective.

Recently Germanium gained a renewed attention because of its attractive properties that can provide solutions for some of the major issues of silicon toward the development of miniaturized and high-efficiency devices and optoelectronic devices.

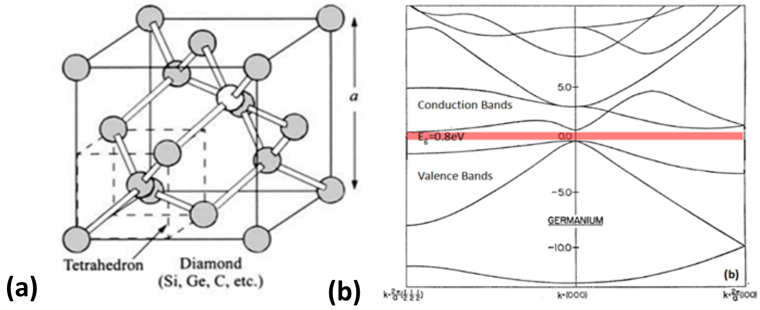

**Figure 1.13:** (a) Primitive cell relative to the diamond lattice characteristic of Si and Ge crystals. In this configuration each atom is bonded with other four identical atoms placed at the corner of a tetrahedron. The lattice constant of the cell is indicated with *a*. (b) Representation of the energy-***k*** dispersion of Ge calculated by the ***k•p*** method [5].

One of the most important features of Ge regards its high compatibility with the current Si technology. In fact, both Si and Ge belong to the group IV of elements and have the same crystalline diamond-type structure [see figure 1.13 (a)]. The diamond structure consists of two interpenetrated face centered (FCC) lattices having a the lattice parameter *a*. The same crystalline structure and the similar values of *a* in Si (0.5657 nm) and Ge (0.5431 nm) lead to a fully miscibility of these two elements over the complete concentration range and for a sufficiently large atomic fraction [36]. This has important consequence for the optoelectronic properties of SiGe alloys [37]. In fact, the strain related to the lattice mismatch between Ge and Si (~4.2%) allows to engineer the bandgap by varying the concentration of Ge in Si (or vice versa). Figure 1.13(b) shows the energy-***k*** dispersion calculated by ***k•p*** method for bulk Ge. Relaxed bulk

Ge has an indirect gap of ~0.67 V at the L valley and a direct gap of 0.8 eV at the Γ valley (*k* = 0). When a biaxial tensile stress is applied, Ge changes from an indirect to a direct gap material with the increase of tensile strain and its capability to absorb/emit light are greatly enhanced [38] - [41]. The engineering of Ge bandgap through tensile strain gives the possibility to develop novel optoelectronic devices (such as LED, laser, optical modulators, etc) fully compatible with Si technology [37] - [41].

Moreover, Ge absorbs light much better than Si. As shown in figure 1.14, the absorption coefficient of crystalline Ge is more than one order of magnitude larger than Si up to 3 eV. This peculiarity is related to the lower value and the nearly-direct nature of its band-gap with respect to Si. The capability to absorb light also in NIR range (where bulk Si is optically blind), combined with its high carrier mobility (related to the lower $m^*$ for electrons and hole in Ge [36]) proposed Germanium as a viable candidate for the fabrication of IR photodetectors, high-speed optical modulators as well as high efficiency multi-junction solar cells [38]- [42].

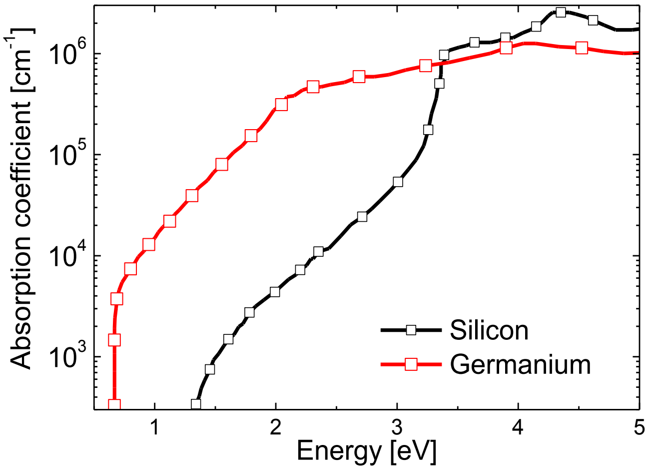

**Figure 1.14:** Absorption coefficient of crystalline Silicon and Germanium, from ref. [25].

For the above mentioned properties, Ge is intrinsically more suitable than Si for what concerns the capability to absorb light. However, the usage of such material in the bulk form has been quite limited in the past because of the high production costs. In this regard, the usage of Ge in form of nanostructures could meet the scarcity issue of this element, giving also the chance to exploit the QCE occurring in these systems. In particular, Ge shows an exciton Bohr radius (~24 nm) well larger than that of Si (~ 5 nm) [43]. This means that it should be possible to easily tune the absorption edge of Ge NS from the IR across the visible range without the needing to shrink too much the NS size, as already shown in figure 1.10.

Such opportunity, together with the larger absorption capability and the quasi-direct bandgap of Ge, make Ge NS very attractive for the application in a large variety of devices, spanning from energy-tunable light harvesters (e.g. multi-junction solar cells and photodetectors) to efficient optoelectronic devices. In the following paragraphs an overview of the state of the art regarding the exploitation of such properties most interesting properties of Ge NS and their possible applications will be shown. These include: optical modulators, efficient photodetectors and solar cells.

### 1.3.1 Light Absorption Modulation

Modulating light absorption is an essential characteristic for the development of novel Si-compatible optoelectronic devices for telecommunications and computer interconnections. High-speed silicon optical modulators based on metal-oxide-semiconductor capacitor have already been demonstrated, but because the light modulation mechanisms in silicon are relatively weak, several mm-long devices or sophisticated high-quality factor resonators have been necessary [44]. A successful approach toward the fabrication of optical modulators is to exploit the quantum confinement Stark effect (QCSE) occurring in confined system.

QCSE is a strong change of the optical absorption of a material when an external electric field is applied. Such effect is typically observed in III/V semiconductor quantum wells, due to their strong direct optical transitions [45]. However the demonstration of QCSE, in a silicon-compatible materials such as Ge QWs could open up many new possibilities for electrical modulation of light absorption [46]. In fact, though germanium has an indirect bandgap (~0.67 eV), it is possible to exploit the stronger optical transitions associated to its direct bandgap at 0.8 eV.

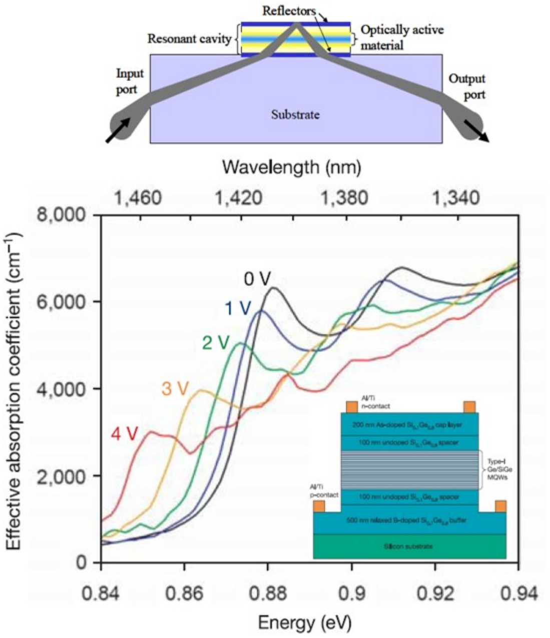

**Figure 1.15:** (Top figure) Side-entry optoelectronic modulator schematic. (Bottom figure) Strong QCSE is observed at room temperature with reverse bias from zero to 4V. The inset shows the cross-sectional view shows the structure of strained Ge/SiGe multiple quantum wells (MQWs) grown on silicon on relaxed SiGe direct buffers. Adapted from [46], [47].

As shown in the inset of figure 1.15, strong QCSE have been demonstrated in strain balanced Ge/SiGe multiple QWs (QW 10 nm thick) grown on a relaxed Ge-rich SiGe buffer layer on Si in a *p-i-n* configuration [46]. When an electric field is applied a clear shift due to QCSE occurs. In particular, the absorption curve at zero bias (0 V) consists of two exciton peaks at 0.88 and 0.91 eV, corresponding to the heavy hole and light hole to Γ electron transitions. The strong electric field provided by the applied voltage produces a shift of the electron states toward lower energies, while the hole states shift to higher energies. This produces a shift of the absorption edge to lower energies, as shown in Figure 1.15. The strong electro-absorption observed in Ge/SiGe multi QWs is comparable to that of QCSE III/V QW structures and is very promising for electro-absorption modulators operating at high speed, low power and operating voltage and with small device areas.

### 1.3.2 High efficiency photodetectors

Due to its high absorption coefficient in the NIR region and the advantage of ease integration with Si, photodetectors based on bulk Ge has been already largely utilized for light detection in the telecommunication wavelength range of 1300 - 1600 nm, but the cost and the device speed are issues. In recent years, various configurations of thin-film Ge-based photodetectors (*p-i-n*, waveguide coupled or avalanche gain detector design) have been developed and demonstrated high values of performance (0.5 - 1 A/W at 1550 nm) [38]. However, further miniaturization of the components design and optimization of the performance at low or zero bias is essential to achieve high energy efficiency and reduced costs for a large-scale electronic-photonic integration. In this scenario, the discrete levels produced in Ge NS by quantum confinement can guarantee promising applications for light detection in narrow spectral IR and compatibility with CMOS technology as well as reduce production costs. In particular, due to the band offset at the

Ge/Si heterojunction, discrete energy levels can be formed inside Ge at the nanoscale. With this approach, different configurations can be used to extend the cut-off wavelength and exploit the absorption between discrete states in Ge QDs. For example, metal-semiconductor-metal photodetectors having a Ge QDs/Si ML as active region already demonstrated potentiality at 1.3 and 1.55 µm, with responsivity of about 0.1 A/W [48]. The use of Ge QDs in waveguide-coupled *p-i-n* photodetectors showed a larger photoresponse compared to *p-i-n* Si photodetectors, with responsivity of ~210 mA/W at 1.3 µm (see figure 1.16b). Another study on metal–oxide–semiconductor (MOS) tunneling photodetectors with Ge quantum dots embedded in the Si semiconductor region showed high responsivity (~600 mA/W) at 820 nm, but only a limited photoresponse (< 1 mA/W) in the NIR [49].

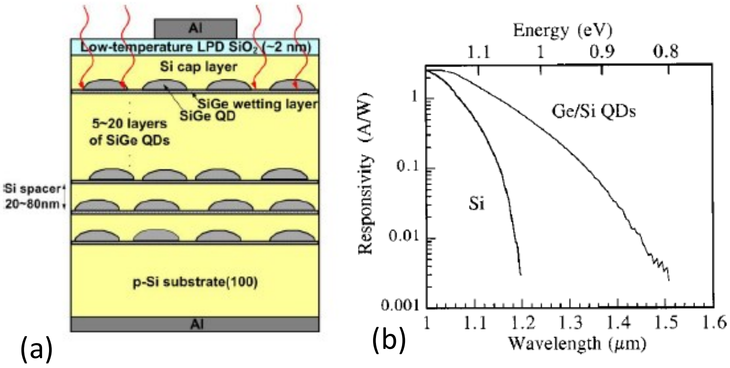

**Figure 1.16:** (a) Schematic structure of MIS SiGe/Si QD photodetector [48]. (b) NIR response of a silicon *p-i-n* photodetectors with Ge/Si QDs multilayer in the intrinsic region. The response of a silicon *p-i-n* photodiode is given for comparison [50].

Though QD-based photodetectors show promises for integration in CMOS technology, further efforts are required to improve the performances towards successful fabrication of sensitive imaging systems.

Only recently, MOSFET-like PDs based on Si QDs embedded in the oxide layer showed responsivity up to 2.8 A/W at 1.55 $\mu$m and an internal photoconductive gain efficiency of 200% [51], [52], whereas Ge QD-based PDs reached even higher photoresponse in the VIS region with photo-conversion efficiency of ~400% [53][54]. We recently reported on MOS PDs with a ~250 nm active layer of 2 nm-diameter amorphous Ge NCs in $SiO_2$ with even better performance: very high values of responsivity (up to 4 A/W) and quantum conversion efficiencies up to 700% in the VIS-NIR wavelength range [55]. In addition, this type of PD demonstrated to achieve a time response down to ~40 ns, with minimal loss in responsivity [56]. These results open new fascinating routes toward the development of high-efficiency light harvesters based on Ge QDs and will be extensively investigated on chapter 4.

### 1.3.3 Group IV nanostructures solar cells

Quantum dots have attracted much attention for their possible use in photovoltaic applications because of the potentiality to overcome the limits of conventional single-junction devices. In particular, by exploiting the size-dependent band-gap tuning that occurs in confined system is theoretically possible to increase the fraction of absorbed light from solar spectrum in multi-junction QD-based solar cells. For a terrestrial solar spectrum (AM1.5G, 1000 W $m^{-2}$) the optimal band-gap of the top cell required to maximize energy conversion efficiency is 1.7–1.8 eV for a two-cell tandem combined with a crystalline Si (c-Si) bottom cell [5]. Cho et al. demonstrated solar cells consisting of phosphorus-doped Si QDs in a $SiO_2$ matrix deposited on p-type crystalline Si substrates (c-Si) have demonstrated conversion efficiency of about 10%, with open-circuit voltage ($V_{oc}$) increasing proportionally with the reduction of QD size [57]. However, up to date, all the reported experiments on such a type of cells evidenced a reduced $V_{oc}$ and a lower short circuit current ($I_{sc}$) with respect to single-junction solar cells, due to photocarriers recombination at the QD/bulk interface. In order to improve the light absorption in conventional solar cell and increase the overall conversion efficiency, especially in the IR part or the spectrum, another promising approach could be to use NS for intermediate band solar cells. Recently, *p-i-n* solar cells with the intrinsic layer composed by multilayers of Ge QDs embedded in Si demonstrated an enhanced conversion efficiency for λ> 1400 nm, reflecting the fact that the Ge QDs cause additional photon absorption at longer wavelengths of the solar spectrum [58], [59].

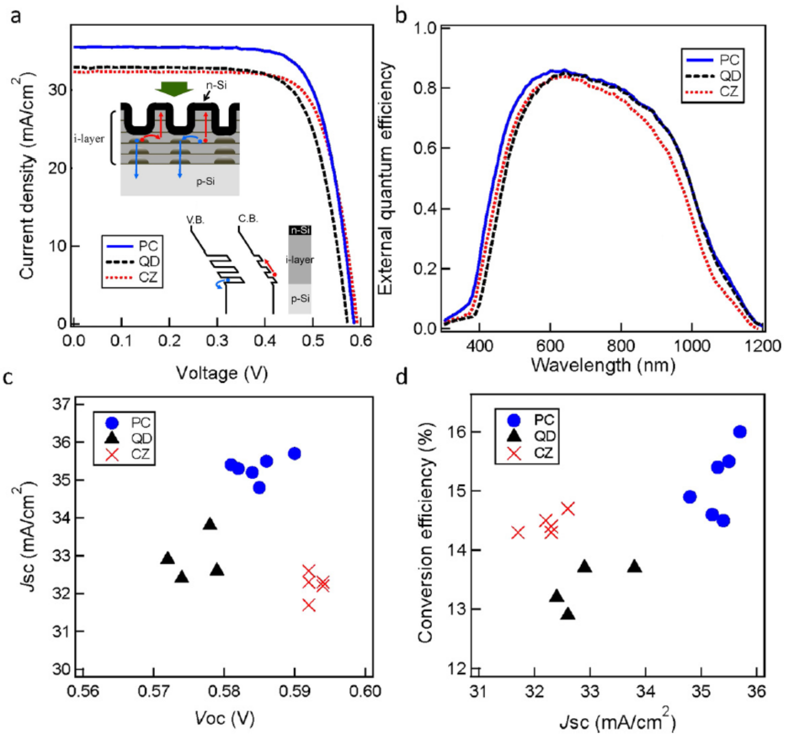

**Figure 1.17:** Comparison of the performances of solar cells with photonic nanocrystals coupled with Ge QDs (PC), with Ge QDs only (QD) and the control CZ Si solar cell. The insets in (a) illustrate the fundamental structure and the band alignment of the device. Adapted from ref [60].

In addition, the performance of solar cells can benefit also of innovative design architectures. Very recently, an enhanced photon capture and carrier generation has been demonstrated in p-i-n solar cells employing two-dimensional photonic nanocrystals coupled with Ge QDs (see inset in figure 1.17a). As shown in figure 1.17, this type of solar cells showed a marked increase of the conversion efficiency with respect to a reference Si *p-i-n* cell, due to the coupling of Ge QDs with photonic crystals that guarantee an enhanced light trapping and photoconversion. Therefore, an optimized light management and a proper control of the optical and electronic properties of QDs-based solar cells can effectively boost the photo-conversion performance beyond the actual limit of conventional solar cells.

Though these results are very exciting, some concerns still rely on the multi-step fabrication processes of QD-based solar cells that could not be compatible with a large-scale production in terms of time and costs. The price of a solar module represents around half of an installed solar-energy producing system. Therefore, increasing the conversion efficiency and reducing the cost of solar module are both effective ways to make photovoltaic technology competitive with the energy production sources. An alternative simpler and low cost fabrication approach is represented by solution processing techniques, where colloidal nanoparticles are synthesized in thin films from a liquid phase solution. Solar cells based on semiconducting nanoparticles ($TiO_2$/ZnO nanowires) fabricated with this approach have recently demonstrated conversion efficiency as high of 7% [61], [62]. Though the firsts colloidal solar cells employed mainly group III-V NS (PbSe, PbS, CdTe, CdSe, [62], [63]), the focus on group IV colloidal NS for solar cells is increasing in recent years. Recently Liu et al. reported on Schottky diodes, fabricated by spin coating intrinsic silicon nanocrystals (Si NCs) from colloidal suspension. Such a devices showed a photovoltaic response with a short circuit-current density of 0.148 mA/cm$^2$, and open-circuit voltage of 0.51 V [64]. In a similar way, Schottky solar cells fabricated by a solution process of Ge NWs demonstrated and enhanced photovoltaic performance with respect to similar devices employing Si NWs due to the high absorption capability of Ge [65].

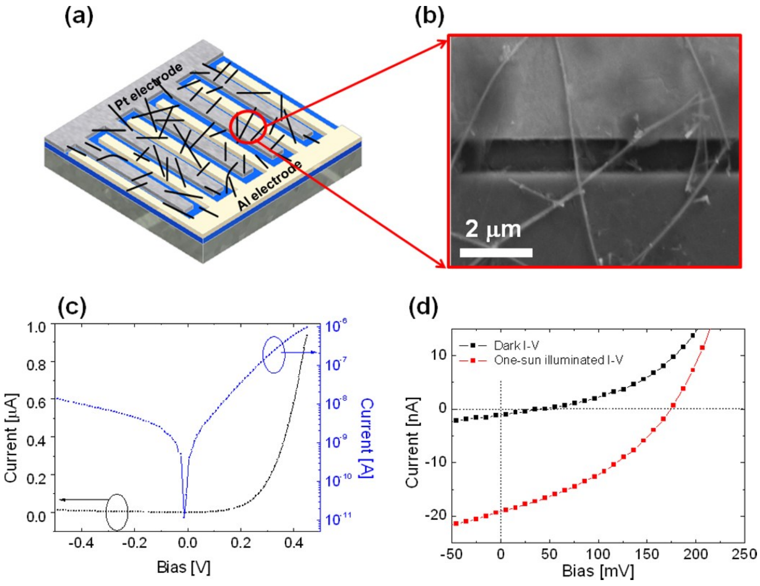

**Figure 1.18:** Schematic of the Ge NWs Schottky solar cell (Al-Ge NWs-pt) (a). SEM image showing Ge NWs in contact with the Pt and Al electrodes (b). Dark *I-V* characteristics of the Schottky device. *I-V* characteristic under one sun illumination, the Ge NW Schottky solar cell yields a Voc of 177 mV and an $I_{sc}$ of 19.2 nA. Adapted from ref. [65].

Moreover, solar cells can benefit of the use of hybrid materials such as in organic – inorganic compounds because of the advantage to improve carrier transport through the organic layer. Recently, Liu et al. fabricated a hybrid solar cells based on blend films of Si NCs/poly(3-hexylthiophene) (P3HT). These devices behaves like excitonic solar cells, with Si NCs taking the role of electron acceptor, and exhibited $J_{sc}$ of 3.3 mA/cm2, $V_{oc}$ of 0.75 V and yielding a conversion efficiency of around 1.15% after thermal treatment [66]. Similar hybrid devices, based on P3HT and silicon Si NWs arrays demonstrated external quantum efficiency (EQE) of 76% at 800 nm and a power conversion efficiency (PCE) of 5.9% under AM1.5 solar irradiation at 100 mW $cm^{-2}$ [67]. Despite the interesting optical properties of Ge NS less reports are present in literature for Ge NS-based solar cells. Recently, Sun et al. reported on Schottky PV solar cells based on hybrid QDs/P3HT composites having broadband photoresponse and open circuit voltage up to 0.45 V. However, the poor crystallinity of Ge QDs and the large amount of defects limited the electron transport photocarrier extraction in the active hybrid film to 41.5 μA/$cm^2$, corresponding to a total power conversion of only 0.013%. in these devices is limited by due recombination. Holman et al. reported very preliminary results on Ge NC/Si wafer junction prototype solar cells, showing open-circuit voltages as large as 0.25 V and short-circuit current density of nearly 4 mA/$cm^2$, with a significant improvement over previous reports [68]. Therefore, though solution processed group IV nanomaterials demonstrated interesting photo-conversion capability, a further research is needed to optimize the carrier transport and collection for PV applications. By rationally modifying the group IV nanomaterials with functional groups, better surface passivation and optimized band alignment with organic materials are expected to further boost the performance of hybrid PV devices.

For this reason, a detailed investigation of the light absorption and photo-carrier extraction process in Ge NS based films is of essential importance not only for the knowledge and control of the fundamental physical processes occurring in these systems at the nanoscale, but also for the optimization of the performances of any type of light harvesting device employing Ge NS.

## 1.4 Motivations of this thesis

The aim of this thesis is devoted to a detailed investigation of the structural and optical properties of germanium nanostructures and their application in efficient light harvesting devices. Particular attention is given to the investigation of the strength of the quantum confinement occurring in these systems and in the contributions coming from concomitant effects.

This thesis is organized as follows:

The second chapter provides a general overview of the theory governing the light absorption process in bulk semiconductors and its extension in confined materials. Theoretical and experimental arguments on the validity of Tauc model, commonly used to describe the optical absorption in bulk amorphous material, will be given for what concerns the light absorption in amorphous Ge nanostructures. To experimentally prove this, we will investigate the optical absorption of single amorphous Ge quantum wells (QWs, 2 to 30 nm thick) deposited at room temperature on fused silica substrate by magnetron sputtering technique. The confined dimensions clearly modifies the photon absorption, inducing a clear blue-shift of the bandgap and an enhanced oscillator strength with reducing QW thickness. The good agreement between experimental data, extracted by using Tauc model, and effective mass theory calculations demonstrates the dominant role of quantum confinement in the light absorption of Ge QW and confirms the validity of Tauc model in the description of the fundamental optical properties of confined systems.

In the third chapter is presented a detailed experimental investigation on the synthesis, structural characterization and optical absorption properties of ensembles of Ge quantum dots (QDs) embedded in a dielectric matrix. Ge QDs embedded in $SiO_2$ or $Si_3N_4$ matrices have been synthesized through thermal annealing of Ge-rich films deposited by plasma enhanced chemical vapour deposition (PECVD), co-sputtering deposition or Ge implantation technique. We will demonstrate that the type and stoichiometric quality of the hosting matrix has a fundamental role in controlling both the growth and the optical properties of Ge QDs. In particular, the optical properties of these systems appear to be quite complex and not always can be described only by their size through quantum confinement effects. For this reason, we studied the contributions coming from other structural parameters such as: QD density and spacing, distribution, hosting matrix and amount of defects. We will give evidence that such parameters have a strong role in the light absorption process of Ge QDs and clearly affect both the bandgap and the optical oscillator strength of these systems with respect to a pure quantum confinement regime.

The fourth chapter is devoted to the investigation of the conduction mechanism and photo-carrier extraction efficiency of prototypal devices using Ge nanostructures. We will demonstrate that Ge nanostructures can be effectively used as active absorber and conductive medium in light harvesting devices. In particular, we will report on the spectral response of metal-insulating-semiconductor (MIS) devices employing single amorphous Ge QW or packed arrays of Ge QDs as active photo-conductive medium. Devices with Ge QWs exhibit a clear enhancement of the photocurrent with the QW thickness, indicating a key role of Ge in the electron-hole pair generation. When Ge QDs are used even larger performances are achieved due to a large photoconductive gain mechanism activated by the presence of Ge QDs. We will investigate the role of Ge QDs in the performances of these type of photodetectors and explain such a large photoresponse as the result of a photoconductive gain mechanism assisted by trapping of photo-generated holes in Ge QDs. These results clearly demonstrate the large applicability of Ge QDs for the fabrication of high-efficiency and fast Si-compatible photodetectors and their potential application as active light-sensitizer medium in future PV cells.

# Chapter 2

# Light Absorption at the nanoscale: the ideal case of Ge quantum well

*In this chapter, we will give a brief overview of the theory of the light absorption in bulk semiconductor and NS materials. In particular, we will provide more details on the Tauc approach theory, used to evaluate the optical properties of bulk amorphous materials (such as bandgap, DOS, optical oscillator strength) from absorption spectroscopy measurements and the validity of this method also in describing amorphous NS. Then, we will investigate the optical absorption of single amorphous Ge quantum wells (QWs, 2 to 30 nm thick) deposited at room temperature on fused silica substrate. As the result of the confinement of this system, the optical absorption shows a marked size-dependent blue-shift and an enhanced oscillator strength with reducing the QW thickness. Such a behavior is sign of a strong quantum confinement of excitons occurring at room temperature and for a disordered material as amorphous Ge QW is. Still, the optical bandgap and the oscillator strength, extracted by Tauc method, are fully in agreement with the theoretical values calculated within the effective mass approximation (EMA), confirming the validity and the effectiveness of our approach based on optical absorption spectroscopy.*

## 2.1 Light Absorption: from bulk to confined materials

The two main fundamental (and complementary) processes describing the interaction of light with matter are the photon absorption and emission (see schematic diagram in figure 2.1). Both these fundamental processes have been extensively employed in the past decades for the understanding of the intrinsic optical behavior of materials at the nanoscale and to directly measure the effects of quantum confinement in these systems. However, it has been shown, both experimentally and theoretically, that the optical properties of NS are very sensitive to the presence of defects, strain effects, impurities that can reduce or even hide the quantum confinement occurring in these systems, especially at room temperature.

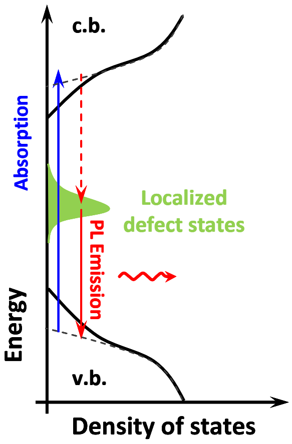

**Figure 2.1:** Schematic representation of the typical band diagram in semiconductors and intra-band absorption/emission processes.

Due to the importance of this field, both for fundamental studies or for light harvesting applications, a proper modelling of the light-matter interaction is required, especially for what concerns the optical absorption. The optical properties of a semiconductor are defined by the inter-band transitions in the 1 – 10 eV range and can be studied within the semi-classical theory of the light-matter interaction. We consider a radiation of frequency ω, wave vector ***q*** and amplitude $A_0$:

$$A(r,t) = A_0 e^{i(q \cdot r - \omega t)} \tag{2.1}$$

One of the most important figure of merit to study for the optical behavior of a material is the absorption coefficient. When a radiation of intensity $I_0 = |A|^2$ passes through a material of thickness *x* and absorption coefficient *α*, it comes out with a lower intensity *I* given by the Beer-Lambert law:

$$I = I_0 e^{-\alpha x} \tag{2.2}$$

The absorption coefficient *α* is defined as the ratio between the energy absorbed per unit volume and time and the incident flux of electromagnetic energy $u\left(\frac{c}{n}\right)$:

$$\alpha(\omega) = \frac{\hbar\omega W(\omega)}{u\left(\frac{c}{n}\right)} \tag{2.3}$$

where *n* is the refractive index of the medium and *W(ω)* is the rate of interband transitions per unit volume.

The transition probability *P* of an electron from the initial state $\boldsymbol{k_i}$ in the valence band to the final state $\boldsymbol{k_f}$ in the conduction band, induced by absorption of a photon with energy $\hbar\omega$, is calculated from the “Fermi Golden Rule” [69], [70]:

$$P_{vk_i \to ck_f} = \frac{2\pi}{\hbar}\left(\frac{eA_0}{mc}\right)^2 \cdot \left|\left\langle \varphi_{ck_f} \left| e^{iqr} e_0 \cdot p \right| \varphi_{vk_i} \right\rangle\right|^2 \delta\left(E_f - E_i - \hbar\omega\right) \tag{2.4}$$

The total rate of interband transitions per unit volume *W(ω)* is obtained by summing over all the allowed ***k*** in the Brillouin zone (BZ) between valence and conduction band:

$$W(\omega) = \sum_{v,c} \int_{BZ}^{\forall k} \frac{2dk}{(2\pi)^3} P_{vk_i \to ck_f} \tag{2.5}$$

While the density of electromagnetic energy *u(c/n)* is given by:

$$u\left(\frac{c}{n}\right) = \frac{n^2 A_0^2 \omega^2}{2\pi c^2} \tag{2.6}$$

From eqs. 2.2 to 2.5, the absorption coefficient of a semiconductor material can be written as:

$$\alpha(\omega) = \frac{4\pi^2 e^2}{ncm^2\omega} \sum_{v,c} \int_{BZ}^{\forall k} \frac{2dk}{(2\pi)^3} \left|e_0 \cdot M_{cv}(k)\right|^2 \delta\left(E_f - E_i - \hbar\omega\right) \tag{2.7}$$

where $M_{cv}(k) = \left\langle \varphi_{ck_f} \left| e^{iqr} e_0 \cdot p \right| \varphi_{vk_i} \right\rangle$ is the optical dipole matrix element, which describes the effective probability of the electronic transition. Since $\left|\left\langle \varphi_{ck_f} \left| e^{iqr} e_0 \cdot p \right| \varphi_{vk_i} \right\rangle\right|^2$ is slowly varying with ***k***, it is convenient to neglect the ***k*** dependence of $M_{cv}(k)$ [25],[69], [70]. Then, eq. (2.7) can be rewritten in a simplified version as:

$$\alpha(\omega) = \frac{4\pi^2 e^2}{ncm^2\omega} \cdot J_{cv}(k) \cdot \left|M_{cv}\right|^2 \tag{2.8}$$

where $J_{cv}(k)=\int_{BZ}^{\forall k}\frac{2dk}{(2\pi)^3}\delta\left(E_f-E_i-\hbar\omega\right)$ is the joint density of states (JDOS) in valence and conduction bands involved in the absorption of a photon with energy $\hbar\omega$. In eq. (2.8) the quantity $O_s=\frac{2|M_{cv}|^2}{m\hbar\omega}$ defines the oscillator strength of the optical transition [25], which gives a measurement of the magnitude of the coupling between states in valence and conduction bands involved in the light absorption process.

The above formalism, used to describe the optical absorption in bulk semiconductors, is valid also in NS if the dipole approximation is fulfilled. Such approximation is based on the assumption that the wavelength of the excitation light is much larger than the exciton Bohr radius of the NS [26]. Such approximation is fully justified if we consider that the typical Bohr radius is in the order of few to some ten of nanometers (~4.9 nm for Si and ~24 nm for Ge, [71]), while the typical wavelength of light excitation is of several hundred of nm. Thus, the main effect that is expected when the dimensionality of the system is reduced regards the shift of the absorption edge towards higher energies due to QCE, in agreement with eq. (1.4). Moreover, since $\alpha$ is proportional to the JDOS, we should expect to see features in the absorption spectra related to the discrete optical transitions between quantic states. In addition, the optical absorption efficiency at the nanoscale can be largely enhanced with respect to the bulk system by the excitonic effect. In fact, as the consequence of the reduced dimensionality occurring in NS, electron-hole pairs become confined in a tight space, giving rise to larger overlap of their wavefunctions. This, in turn, leads to a larger oscillator strength and an increased optical transition process rate that can be exploited for novel devices, spanning from efficient optical absorbers to lasers. For example, electro-tuning of the oscillator strength by QCSE in GaAs-based MQW structures demonstrated the possibility of lasing [72]. A similar effect holds also for Si nanocrystals that showed enhanced radiative optical transition rate due to exciton coupling and larger oscillator strength [19], [73][74]. Recently, the same effect has been investigated also for crystalline (c-) Ge QW [75],[76]. Figure 2.2 shows variational calculations on the exciton radius and optical oscillator strength of the direct-band-edge (e1-hh1) transition for c-Ge QW as a function of thickness. As the QW thickness is decreased, the exciton radius decreases due to the strong confinement while the oscillator strength almost doubles.

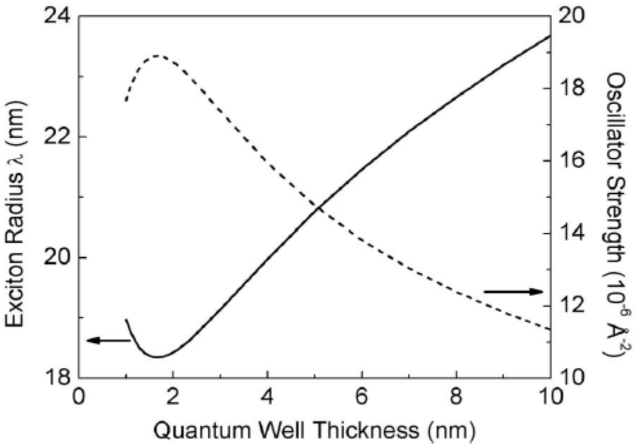

**Figure 2.2:** The exciton radius and oscillator strength as functions of well thickness in Ge/$Si_{0.15}Ge_{0.85}$ quantum well using the 2D variational model. Adapted from ref. [75].

On the basis of this scenario, quantum confinement effects offer the great chance to modify the fundamental optical and electronic properties of bulk materials. Eq. 2.8 gives the possibility to directly extract such fundamental information from experimental measurement of the absorption coefficient of not-confined systems. Indeed, it would be very important to extract the same quantities also for confined systems and to measure the effects of quantum confinement on the optical absorption. This would be extremely beneficial in the nano-material engineering as well as for the physical understanding. In this regard, some important assumptions have to be made in the description of the optical absorption process when passing from bulk to confined materials.

### 2.1.1 Tauc model

In a bulk semiconductor inter-band transitions due to light absorption start at the absorption edge $E_g$, which corresponds to the minimum energy difference between the lowest free state in the conduction band and the highest occupied state in the valence band. As described by eq. (2.8), the absorption coefficient $\alpha$ of a semiconductor depends on the product of the optical transition oscillator strength and the joint density of states involved in the photon absorption process. Therefore, from the experimental measurement of the absorption coefficient one can extract information on the intrinsic optical parameters of a material, such as the optical bandgap $E_g$, the JDOS and the oscillator strength $O_s$. Such important quantities can be derived from eq. (2.8) by using the Tauc approximation, conceived for amorphous indirect semiconductors [77]. Such materials have no long-range atomic ordering, but typically preserve a short-range order with nearly the same atomic arrangement of the corresponding crystal. As result of this effect, electronic wave-functions are more spatially localized and the quasi-momentum vector $\boldsymbol{k}$ is not conserved. In this regard, under the assumptions of parabolic band edges for valence and conduction bands ( $DOS_{c,v} \propto \sqrt{E}$ ), $\boldsymbol{k}$-independent matrix element $M_{cv}$ (as in the case for phonon-assisted indirect transitions in crystalline semiconductors) and optical transitions between extended states from valence band toward the conduction band (usually valid for values of $\alpha$ larger than $1 \times 10^4$ cm$^{-1}$) eq. (2.8) can be re-written as:

$$\alpha = \frac{B}{\hbar\omega}\left(\hbar\omega - E_g\right)^2 \tag{2.9}$$

where $E_g$ is the optical bandgap of the material, while the Tauc coefficient $B$ is proportional, through the optical matrix element $M^2$, to the oscillator strength ($O_s$) of the optical transition [77]. Eq. 2.9 is known as Tauc law and is successfully used to describe the higher part of $\alpha$ (>1×10$^4$ cm$^{-1}$) in amorphous semiconductors [77], [78]. In particular, by plotting $\sqrt{\alpha \cdot \hbar\omega}$ vs. $\hbar\omega$ is possible to extract the values of $E_g$ and $B$ as energy-axis intercept and slope of the linear fit respectively. Such a method was successfully used for the first time to describe the absorption behavior of thin films of amorphous (a-) Ge by Tauc [79]. As shown in figure 2.3 , for low values of $\alpha$ the trend of $\sqrt{\alpha \cdot \hbar\omega}$ is super-linear because of the contribution of transitions related to distorted (more or less localized) states near the band edges (Urbach region) [77], [78]. For larger values of $\alpha$ (typically > 10$^4$ cm$^{-1}$) the trend is linear and gives an optical bandgap for a-Ge of $E_g \sim 0.85\ eV$ [79].

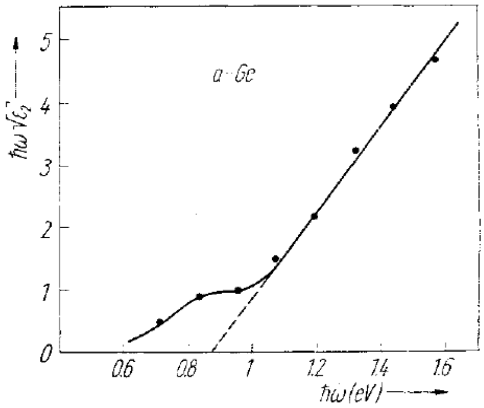

**Figure 2.3:** Tauc plot of bulk amorphous Ge at 300 °K. Adapted from ref. [79].

For most amorphous semiconductors the optical gap estimated using Tauc method shows the best agreement with the other methods employing electrical conductivity measurements [78]. However, there is not a rigorous theoretical justification for this law, because of the difficulty to properly define a lattice potential and calculate the electronic band dispersion for these systems. In any case, by applying Tauc plot is possible to determine the energy gap $E_g$ and the magnitude of the light absorption transition (through the value of *B* constant) by the experimental measurement of the absorption coefficient of a bulk material.

### 2.1.2 The effects of confinement

One open question regarding the evaluation of the optical parameters by applying Tauc's law is whether the same approach holds also for nanostructured materials. In this case, as previously discussed, the main effects of the reduced dimensionality regard the increase of the forbidden energy gap and the increased oscillator strength of the optical transitions between quantic states. Such evaluation is trivial in NS because of the lost of the long range order and the consequent questionable validity of the band structure concept for these systems. Actually, Tauc model is based on the hypothesis of parabolic band edges and optical inter-band transitions between quasi localized states in which the ***k*** vector is not conserved [77]. As discussed previously, such hypothesis are qualitatively applicable in amorphous semiconductors because of the conservation of a short-range lattice order among atoms.

The same behaviour could be also valid for NS. In fact, as the result of their reduced dimension electron-hole wave-functions are localized and the conservation of ***k***-vector is released. In addition, if the size of the NS is not too small, some "memory" of the band diagram dispersion could be still retained also in these systems. To strengthen this assumption, very recent theoretical investigations based on density functional theory calculations demonstrated that the band structure concept can be still adopted also for Si nanocrystals larger than ~2 nm.

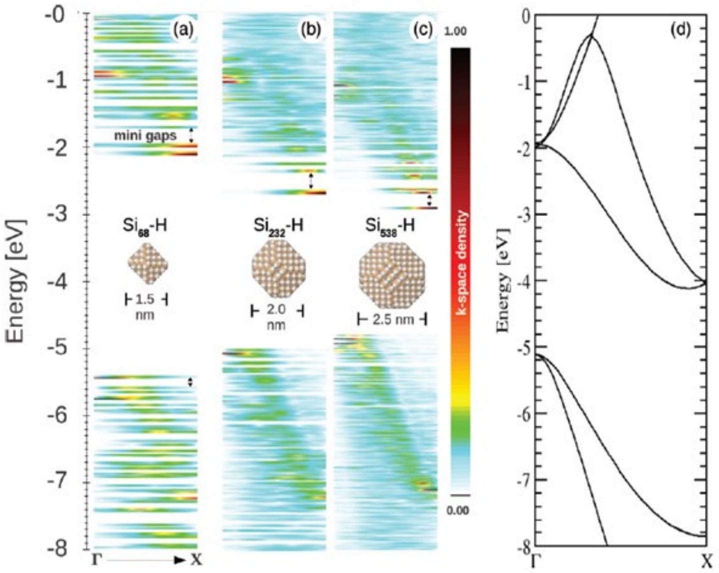

**Figure 2.4:** Projected k-space density of states for H- passivated Si NCs of different sizes (a-c). Band structure of bulk Si for comparison. Adapted from ref. [80].

Figure 2.4 shows the projected k-space density along the Γ-X direction calculated for H- passivated Si NCs [80]. While for NCs smaller that 2 nm there is a full delocalization of the ***k***-vector and the band structure cannot be recognized [fig. 2.4(a)], for larger NCs the dispersion of electronic states resembles the Si bulk band structure for both valence and conduction bands. Due to the strong similarities between bulk Ge and Si, it is reasonable to assume that the same mechanism holds also for Ge NS having relatively large size. In this case, it would be still possible to speak about an electronic band structure resembling that of bulk Ge and Tauc's hypothesis would be still respected also for this confined system.

In this regard, it would be interesting to experimentally verify if and under what conditions Tauc relationship is still applicable to real confined materials. Such experimental confirmation is extremely important because can establish a general route to evaluate the fundamental optical properties of NS from absorption spectroscopy measurements by applying Tauc model. To this aims, in the following section we will investigate the optical behavior of single amorphous Ge QW.

## 2.2 Synthesis and structural characterization of amorphous Ge QW

Investigating the optical properties of a single, one-dimensionally confined system is not an easy task, both for the synthesis and analysis point of view. However, it allows a larger control of its structural parameters with respect to more complex confined systems. Typically, this could lead to QCE with only minor or no contributions from other effects related to size uniformity, shape, etc. In this regard, single Ge QW can be thought as an example of a real dimensionally confined system that more closely approaches to the ideal case of confinement. In addition, despite the conspicuous number of studies on the optoelectronic properties of crystalline Ge QW, only a very limited literature is present for this material in the amorphous phase. As far as a-Ge QW are concerned, only some size-dependent shift of $E_g$ have been evidenced in amorphous Ge/$SiO_x$ QW superlattices deposited by vacuum evaporation [81]. However, no evaluation of the extent of quantum confinement has been reported, especially for the case of a single QW. It is clear that the possibility to exploit QCE also in a-Ge QW, if any, could make this material very promising for the realization of low-cost optoelectronic devices operable at specific tailored wavelengths, or for their potential application in light harvesting devices.

Thin films of amorphous Ge (2- to 30-nm of nominal thickness) have been deposited on (001) n-doped Si wafer or on fused silica quartz substrate by magnetron sputtering deposition. Top and bottom $SiO_2$ films (approximately 10-nm-thick each) were used as barriers for the QW structure to preserve Ge from atmosphere oxidation, as schematized in Figure 2.5.

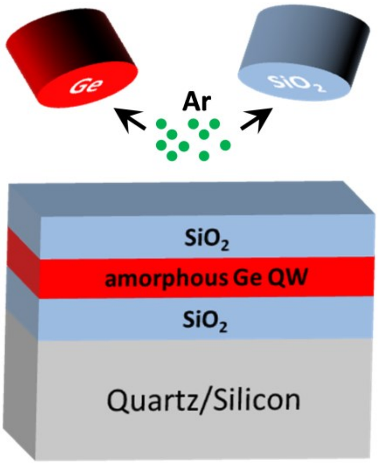

**Figure 2.5:** Schematic representation of the magnetron sputtering deposition process of amorphous Ge QW embedded by SiO$_2$ barrier layers.

Typically, magnetron sputtered films can contain quite amount of voids or low density regions inside them. Still, the amount of voids strongly depends on the working conditions used during the deposition. To avoid as much as possible the presence of voids or low density regions in our samples, we have grown our films in an optimized configuration with low deposition rates (1 nm/min), $5{\times}10^{-3}$ mbar Ar pressure during deposition and starting from a pre-deposition base pressure of $1{\times}10^{-9}$ mbar. These conditions typically ensure the growth of films without grossly voided boundaries [82]. To further verify the proper density and homogeneity of our films, we performed high resolution transmission electron microscopy (HR-TEM) and Rutherford backscattering spectrometry (RBS) analysis to measure the mean thickness and atomic Ge content of our films.

If relevant inhomogeneity occurs in the Ge film, the distribution of the electronic wave function along the plane parallel to the surface would be lost. This effect leads to a change in the nature of quantum confinement from one-dimensional (2D structures) regime to two-dimensional (1D structures) or three-dimensional (0D structures) regimes, as the feature of Such circumstances have been denied by extensive TEM and HR-TEM investigation performed both in plan and in cross-sectional view. As an example, a TEM image is reported in Figure 2.6 for the 5-nm a-Ge QW sample (grown on Si substrate), showing $SiO_2$ films (brighter layers) embedding the Ge QW (thin darker layer). The measured thickness, *d*, and roughness of the a-Ge QW are 5.36 and 3.65 nm, respectively. This means that even if some sparse thinning of the Ge QW occurs, the electronic wave functions are still confined only in the growth direction, preserving the 1D confinement regime. Similar considerations can be done for all the a-Ge QW samples.

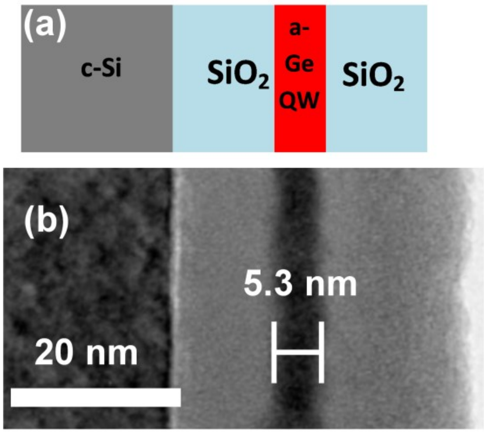

**Figure 2.6:** (a) Schematic of sample structure, together with cross-sectional bright-field Z-contrast TEM images of 5-nm-thick a-Ge QW sample (b). Figure adapted from ref [83].

RBS analysis was employed to measure the Ge dose contained in each sample and to verify the proper stoichiometry of the $SiO_2$ barrier layers. A glancing detection mode was used (1.2 MeV $He^+$ beam, 98° backscattering angle) to enhance the depth resolution. Figure 2.7 reports the RBS data in the 0.88- to 1.09-MeV energy range which is relative to $He^+$ backscattered from Ge atoms. The peak area is proportional to the Ge atomic dose contained in each QW (whose values are indicated in the figure), while the FWHM is proportional to the thickness of the Ge film.

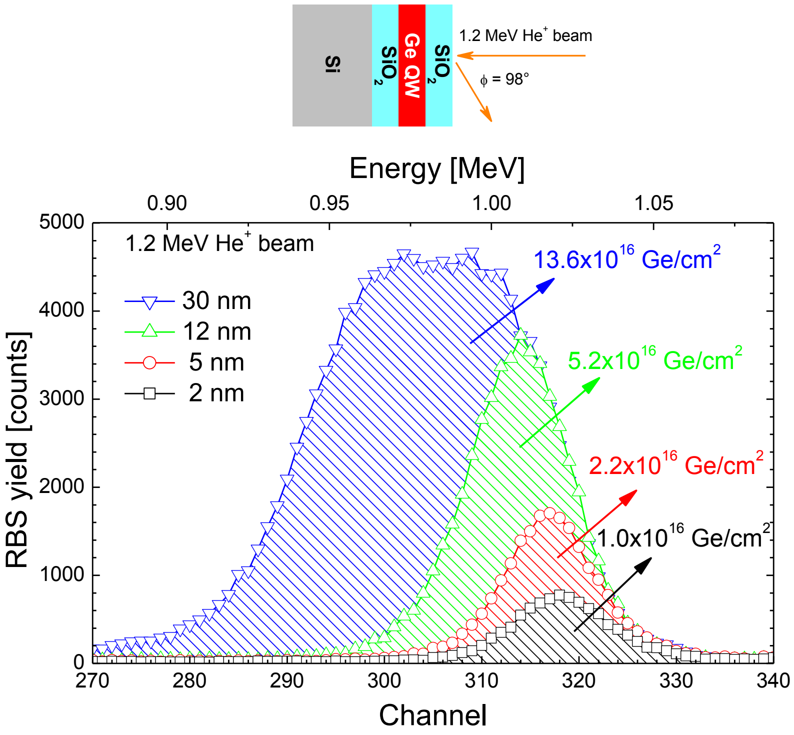

**Figure 2.7:** RBS spectra of a-Ge QWs. The filled areas are proportional to the Ge content of each QW (from $1.0\times10^{16}$ Ge/cm$^3$ to $13.6\times10^{16}$ Ge/cm$^3$), as reported in the figure. The top-image in the figure represents the schematic of analysis setup used for RBS measurements. Figure adapted from ref. [83].

By combining the atomic content evaluated by RBS with the corresponding thickness measured by TEM, we can estimate the density of Ge films. In particular, the thinnest Ge QW (~2.2 nm thick) has an atomic amount of Ge of $1.0\times10^{16}$ at/cm$^2$, corresponding to a density of about $4.5\times10^{22}$ at/cm$^3$. For a 5.35 nm Ge QW, we estimated an atomic amount of Ge of $2.2\times10^{16}$ at/cm$^2$, corresponding to a density $\rho$ of $4.1\times10^{22}$ at/cm$^2$. By considering the mean value of the density, we get $\rho=4.3\times10^{22}$ at/cm$^3$, which is in good agreement with the value for bulk Ge reported in literature ($4.42\times10^{22}$ at/cm$^3$) [25]. This last evidence clearly indicates the absence of low-density regions or voids in the as-deposited a-Ge films, which is crucial to assert that a proper spatial 1D confinement occurs in our single Ge QW case.

### 2.2.1 Light absorption in single amorphous Ge QW

Once evaluated the proper structural composition and density of Ge QW, light absorption spectroscopy was performed in the samples grown on quartz substrates. In particular, accurate transmittance ($T$) and reflectance ($R$) measurements have been performed at room temperature. In figure 2.8, T and R spectra are plotted as a function of the incident wavelength, together with the transmittance of the quartz substrate ($T^Q$ ~ 90%). The presence of Ge films induces a decrease of $T$ spectra in the UV-VIS region with respect to $T^Q$ for all the investigated samples. Such decrease is not offset by an analogous increase of the reflectance, that is $T+R<1$. This means that a consistent part of the incident light is absorbed by the single Ge QW. Moreover, $T$ spectra start to decrease at lower wavelengths as the QW thickness gets thinner, indicating a clear role of the QW thickness.

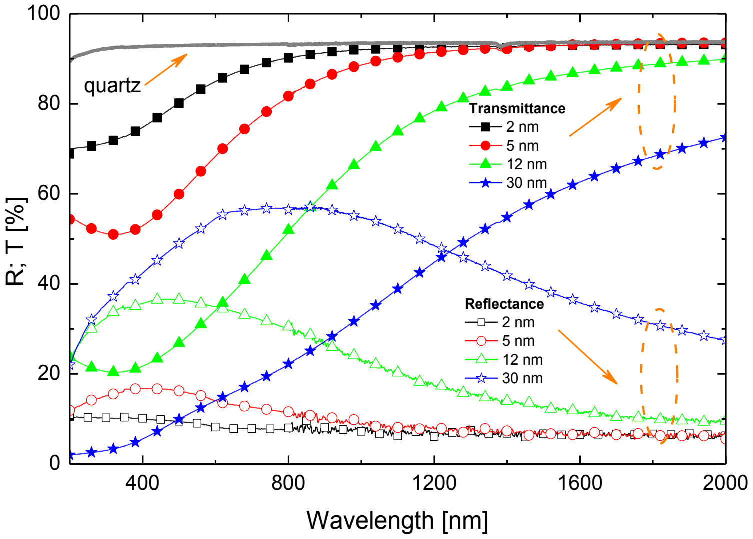

**Figure 2.8:** Transmittance and reflectance spectra for Ge QWs having different thicknesses. The transmittance spectra for the bare quartz substrates (continuous line) is reported for comparison.

To ascertain if some quantum confinement affects the optical properties of a-Ge QW, we calculated the absorption coefficient ($\alpha$) of such thin Ge films, by using the formula:

$$\alpha = \frac{1}{d} \ln \frac{T^{Q}\left(1 - R^{s}\right)}{T^{s}} \tag{2.10}$$

where $d$, $T^S$, and $R^S$ are respectively the thickness, transmittance, and reflectance of the sample [84]. In Eq. (2.10) we used reflectance spectra taken at 20°, after having verified for selected samples that the difference with respect to spectra taken at 0° is negligible. Moreover, multiple reflections are not considered, since they should be fairly irrelevant because of the quite low reflectance values. The overall error on $\alpha$, also including errors on $d$, $T$, and $R$, is about 5%, while the dynamic range of the product $\alpha d$ was $1 \times 10^{-3}$ to $2 \times 10^{-1}$.

Figure 2.9 shows the $\alpha$ spectra of the a-Ge QWs and of an a-Ge film (125-nm thickness) used as a reference for a bulk unconfined film. The absorption coefficient of the 30-nm a-Ge QW is similar to that of the 125-nm a-Ge sample, both evidencing an absorption edge at about 0.8 eV, typical of an a-Ge bulk [79][85]. On the contrary, by decreasing the thickness of the a-Ge QW from 12 to 2 nm, an evident blue-shift occurs in the onset of the absorption spectrum. Moreover, in the 12-nm a-Ge QW, the $\alpha$ spectrum is higher than in the 30-nm a-Ge QW sample, despite the similar onset. Therefore, under 30 nm, the thickness of the a-Ge QW clearly affects the photon absorption mechanism as an effect of spatial confinement on the electronic energy bands. Actually, the Bohr radius for excitons in Ge is about 24 nm [71]. Thus, the observed variation in the absorption spectra can be thought as an effect of quantum confinement on the energy band of a-Ge QWs.

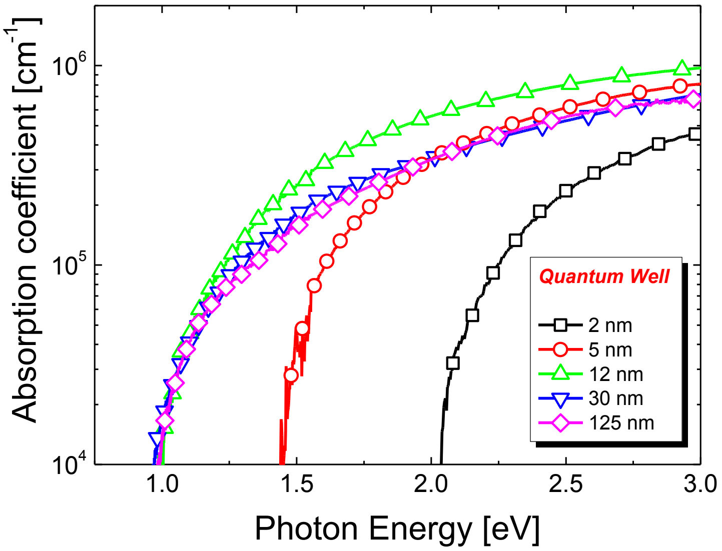

**Figure 2.9:** Absorption spectra of a-Ge QW of different thicknesses, together with the spectrum of a bulk-like 125-nm a-Ge. Figure adapted from ref. [83].

At this point, a proper description of the light absorption mechanism in the a-NS is needed. In this regard the confirmation (or not) of the validity of Tauc model in these systems is fundamental to extract their intrinsic optical properties from absorption measurements. As we described previously, Tauc formula (Eq. 2.9) is commonly used to describe the absorption coefficient α in bulk amorphous semiconductors under the assumption of parabolic band edge states and optical transitions between partially delocalized states. In the case of a-NS, Eq. 2.9 can be used if size effects are properly considered, such as bandgap widening (acting on $E_g$) or enhanced oscillator strength ($O_S$, which increases $M^2$, and then $B$) [70][77]. If the Tauc law properly describes the light absorption also for a-NS, $(\alpha h\nu)^{1/2}$ versus $h\nu$ (called Tauc plot) should give a linear trend in the energy range for which $\alpha > 1\times10^4$ cm$^{-1}$. This clearly occurs for all the investigated a-Ge QWs, as reported shown in Figure 2.10.

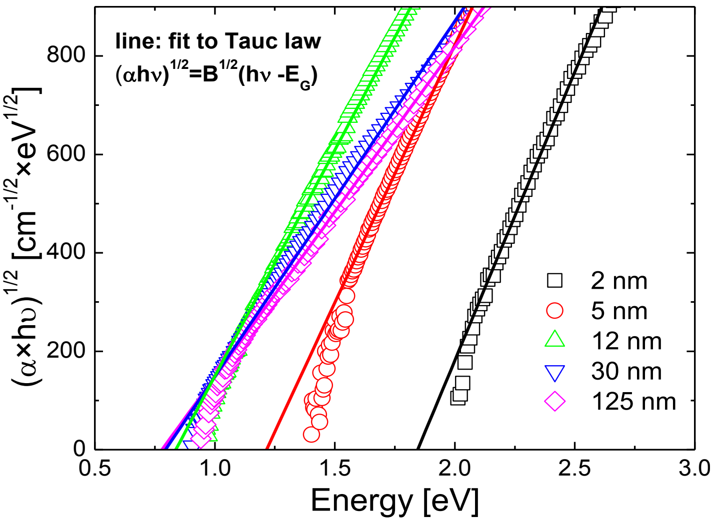

**Figure 2.10:** Tauc plots (symbols) and relative linear fits according to the reported Tauc law (Eq. 2.9, lines). Figure adapted from ref. [83].

Thus, the general hypothesis made for bulk amorphous semiconductors holds also for a-Ge NS. Such hypothesis is also in general agreement with the results obtained by Hapala et al. [80] for the electronic band scheme in Si NCs. The application of Tauc law to a-Ge QWs allows to determine $B$ and $E_g$ through linear fitting procedures (lines in Figure 2.10). As shown in figure 2.10, by reducing the QW thickness down to 2 nm, $E_g$ (fit intercept with energy axis) shifts at higher energy and $B$ (square of the fit slope) increases. These findings confirm the quantum confinement effect in a-Ge QWs. In fact, no variations of the electronic band diagram are expected above the Bohr radius, while below it, a broadening of energy levels shifts $E_g$ to larger values. In addition, the stronger spatial confinement of carriers in very thin a-Ge films leads to excitonic absorption enhancement, which is observed as the increase of $B$. This evidence clearly points out that light absorption can be profitably enhanced by the quantum confinement in a-Ge QWs, confirming the previous indication of another study [81]. In order to quantify if the bandgap widening and the excitonic absorption enhancement are uniquely attributable to QCE, a further verification have to be done.

## 2.3 Quantum confinement in single amorphous Ge quantum wells

Figure 2.11 describes the effect of quantum confinement on the optical bandgap of a-Ge QWs. In particular, it is shown the large size-dependent blue-shift (up to 1 eV) occurs as the QW thickness is reduced down to 2 nm.

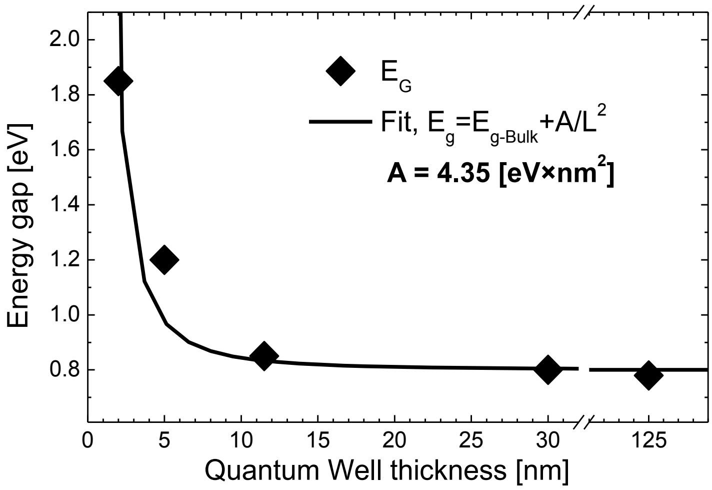

**Figure 2.11:** Experimental values (diamonds) of energy gap in a-Ge QW versus thickness, fitted through effective mass theory formula of QC (Eq. (1.4), solid line). Adapted from ref. [83].

Previous data reported by Bittar et al. on amorphous Ge/SiO$_x$ superlattices evidenced a much lower blueshift of $E_g$ (only about 0.1 eV for the same thickness variation) [81]. Such discrepancy is most likely due to the use of non-stoichiometric SiO$_x$ embedding barriers by Bittar et al instead of SiO$_2$. In fact, as we will discuss in detail in chapter 3, the barrier height of the hosting barrier plays a key role in determining the optical properties and the confinement effect of NS. The use of stoichiometric SiO$_2$ barriers ensures a higher confinement for carriers than SiO$_x$ and gives rise to a larger blue-shift of the optical bandgap for our Ge QWs.

To ascertain if such a large size dependent blue-shift is well described by quantum confinement of carriers, $E_g$ data have been fitted (solid line) within the effective mass theory, assuming an infinite barrier, by eq. (1.4). In our case, *A* is the only fitting parameter, while $E_G^{\text{bulk}}$ was fixed as the bandgap of bulk a-Ge (0.8 eV, [85]), which is also in good agreement with our value for 30-nm QWs. The good fit agreement with experimental data confirms that the shift in the energy gap is ascribed to QCE and that SiO$_2$

layers act as infinite potential barrier, ensuring a strong confinement of electrons within Ge QWs. Moreover, the experimental confinement parameter in a-Ge QWs resulted to be 4.35 eV·nm$^2$, which is about double of the theoretical value of 1.97 eV·nm$^2$ reported by Barbagiovanni et al. for a strong quantum confinement in crystalline Ge QW [29]. Actually, *A* is given by $A = \pi^2\hbar^2/2m^*$, where $m^*$ is the reduced effective mass of excitons, expected to be approximately 0.1 × $m_e$ in Ge ($m_e$ is the free electron mass). The reason of the difference between our experimental valued for a-Ge QW and the calculated one for c-Ge QW can be attributed, at first approximation, to the reduced effective mass of carriers in amorphous NS. This hypothesis agrees also with the experimental observations made by Robner et al. [86] on the effective masses of Ge/SiGe multi-QW (MQW). Therefore, as the result of the larger value of *A*, an increased confinement of carriers and a stronger shift of the optical bandgap is expected in amorphous NS than in crystalline ones.

Beyond the energy blue-shift, another interesting effect of the spatial confinement is the enhanced interaction of light with confined carriers. As explained before, such effect is related to the larger over-lapping of electron-hole wavefunctions in a confined structure that gives rise to an enhanced probability of the optical transition. Such effect is typically observed by photoluminenscence (PL) spectroscopy at low temperature in highly structural ordered systems [87] -[89]. Figure 2.12 reports on the increase in the light absorption efficiency measured for our amorphous Ge QW at room temperature.

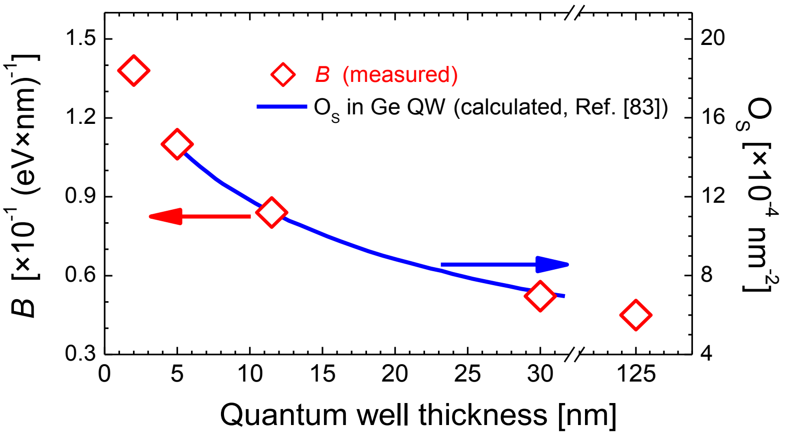

**Figure 2.12:** Experimental values of B (diamonds, left axis) compared with the calculated trend [75]] for the oscillator strength ($O_S$) in Ge QWs (line, right axis). Adapted from ref. [83].

On the left axis of Figure 2.12, the variation of *B* with QW thickness is plotted, as extracted from fits in Figure 2.9. Such a quantity significantly increases up to three times going from a bulk-like a-Ge film to the thinnest QW, evidencing a noteworthy increase of the light absorption efficiency.

Besides the important potentiality of the enhanced absorption efficiency for the fabrication of efficient light harvester, it is even more interesting to focus on the fundamental laws behind such enhanced absorption. In fact, since the *B* parameter in Equation 2.9 includes the matrix element of optical transition *M* (which is related to the oscillator strength, $O_S$), the increase in *B* can be thought as the evidence of the enhanced oscillator strength in the confined system. The thinner the QW thickness, the smaller is the exciton Bohr radius, giving rise to a larger oscillator strength ($O_S$) [75]. Such an effect was predicted and has been observed also for c-Ge QWs [75][76]. Now, for the first time, it is experimentally assessed also in a-Ge QWs. On the right axis of Figure 2.12 is reported the variation of $O_S$ with thickness in the c-Ge QW, calculated in the 5- to 35-nm thickness range by Kuo and Li using a 2D exciton model and infinite barrier [75]. As clearly shown in the figure there is a good agreement between the measured values of *B* and the calculated $O_S$. This last finding is the experimental confirmation that the enhanced absorption efficiency observed at room temperature in a-Ge QWs is actually due to the excitonic effect.

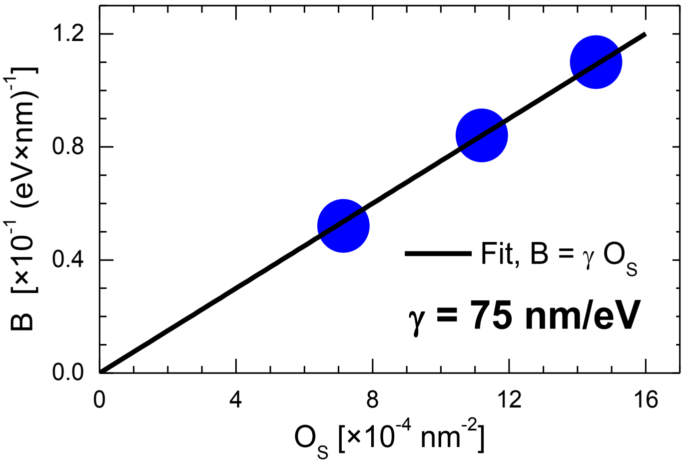

**Figure 2.13:** Linear correlation between the absorption efficiency, *B*, and oscillator strength $O_S$ for a-Ge QW. Adapted from ref. [83].

Finally, in Figure 2.13 is evidenced the linear correlation between *B* (measured at 5, 12, and 30 nm) and the expected $O_S$ calculated for those thicknesses. The linear fitting allows to estimate the factor of proportionality ($\gamma = B/O_S$), which accounts for the absorption efficiency normalized to the oscillator strength. The good linear correlation between *B* and $O_S$ is the demonstration of the effectiveness of Tauc model in describing the light absorption process also in confined structures. Thus, a proper modeling, based on Tauc approach, applied to light absorption measurements at room temperature allows to quantify the extent of size effects and to disentangle the oscillator strength increase and the bandgap widening. Such approach has been demonstrated here to be valid for a-Ge

QWs. More generally, it could represent a powerful tool to investigate and describe the fundamental quantities ruling the light absorption process also of other types of a-NS.

## 2.4 Conclusions

In this chapter, we provided a general overview of the theory governing the light absorption process, both in bulk and in confined semiconductor nanostructures. Starting for the explanation of the Tauc model, commonly used to describe the optical behavior of bulk amorphous semiconductors, we gave arguments that the same model is respected also for amorphous NS. To experimentally prove this, we reported on the large quantum confinement effects shown by single amorphous Ge ultrathin (2- to 30-nm thicknesses) films embedded in $SiO_2$ barrier layers. These confined structures, grown by magnetron sputtering at room temperature, revealed a large blue-shift (about 1 eV) in the optical bandgap and a significant increase (up to three times) in the light absorption efficiency due to an enhanced optical oscillator strength. Such effects, typically observed at cryogenic temperature or in crystalline materials, have been evidenced for the first time in the amorphous phase and at room temperature for Ge by using absorption spectroscopy measurements. Moreover, the experimental values of the optical bandgap and oscillator strength, extracted by Tauc model, are fully in agreement with the expected values calculated within the effective mass theory in confined structures. Such agreement demonstrates that: 1) the optical behavior of amorphous Ge QW is fully governed by quantum confinement effects and; 2) Tauc model can be applied also in NS materials and represents a powerful approach to describe the fundamental optical properties of these systems

# Chapter 3

# Light Absorption in Germanium Quantum Dots

*After having ascertained that the optical properties of single one-dimensionally confined Ge behave as an ideal-like structure for what concerns the quantum confinement of its carriers and having proven the validity of Tauc method also for confined systems, in this chapter we will investigate the synthesis and optical properties of more complex structures, as ensembles of Ge quantum dots. Many other parameters can concur in defining the optical behavior of these systems, which may not be described by only quantum confinement effects. For this reason, we will investigate the light absorption process of ensembles of Ge QDs and the effects due to QDs size, QDs spacing and distribution, quality and type of the hosting matrix and synthesis technique. In particular, this study will regard the synthesis and optical properties of Ge QDs embedded in* $SiO_2$ *or* $Si_3N_4$ *matrices and grown after thermal annealing of Ge-rich films synthesized by co-sputtering deposition, plasma enhanced chemical vapour deposition (PECVD) and ion implantation.*

## 3.1 From 2D to 0D structures: when not only size matters!

As soon as one moves from an almost ideal 2D confined system, as a single QW, to a 0D confined system (i.e. QD), a stronger quantum confinement of the excitons is expected, as theoretically and experimentally observed for many nanostructures. Indeed, the light absorption process in more complex structures, as QDs are, cannot be modeled only by their size, since other relevant effects may strongly contribute to the photo-conversion process.

A key-example of such a complexity is given by the numerous studies on the optical properties of Si QDs. In these structures the variation of the optical bandgap was experimentally shown to rely not only on the size tuning, but also on the presence of defects, on the relative presence of the amorphous-crystalline (*a*-*c*) phase, on the matrix-induced strain on QDs [29], [71], [80], [84]. A great role of the embedding matrix, beyond that of QC regime, and of the stoichiometry of QD interfaces was also evidenced.

This puzzling scenario does not change very much when switching from Si to Ge QDs. In addition, the optical properties of Ge nanostructures, especially for what concerns the absorption behavior, have been much less investigated than Si ones. Up to now, Ge QDs embedded in $SiO_2$ have mainly been studied for optoelectronic applications and, similarly to Si QDs, contrasting results appear in the literature for what concerns their optical properties. For example, Fuji et al. observed a clear size-dependent near infrared photoluminescence from Ge nanocrystals embedded in $SiO_2$ matrix due to QCE [90]. For the same system, Zacharias et al. reported on a broad and size-independent blue-PL emission not attributable to the radiative recombination of excitons confined in the nanocrystals, but rather to the contribution of defects at the nanocrystal/matrix interface or in the matrix [91]. A similar behavior holds also for the light absorption. Boestedt et al. reported on the strong QCE in the conduction band of Ge QDs in $SiO_2$ observed by X-ray absorption spectroscopy [92]. Teng et al. studied Ge QDs embedded in $Al_2O_3$ or in AlN matrix. They showed a blue-shift of the $E_1$ and $E_2$ optical direct transitions with decreasing QD size, but no differences have been found on the optical behavior between the two matrices [93]. More recently, Shih et al. reported evident interfacial effects of Ge nanocrystals embedded in ITO or ZnO, with larger absorption onset energies in ITO, attributed to a Ge oxide shell formed at QD surface [94]. Actually, Ge–O bonds and the related strain can modify the electronic energy levels, thus affecting light absorption and emission processes [91], [95][96]. Moreover, the QDs formation can strongly be controlled by the matrix, as Ge nanoclusters nucleation and ripening depend on diffusivity and interface energies between Ge and its surrounding [97][98]. Finally, it was evidenced that also QDs spacing and distribution may have a strong role on the optical absorption of these systems, even hiding the effects due of quantum confinement [99][100].

Thus, the optical behavior of QDs appears to be quite complex, and seems not to be fully described only by the QD size variation through QCE. In this regard, in order to give a more clear understanding of the light absorption in Ge QDs, it would be essential to disentangle the role of the size from all the above mentioned parameters and to identify the extent of their contribution, if any, in the light absorption process. To this aim, in next paragraphs we will systematically investigate the light absorption process in Ge QDs, trying to distinguish (in turn) the contribution of QD size from: (a) the synthesis technique, (b) the QD spacing and distribution, (c) the effects of the hosting matrix.

Among all the reported techniques used for the synthesis of Ge QDs, for the sake of simplicity in the following paragraphs we will focus on Ge QDs synthesized by conventional co-sputtering deposition, plasma enhanced chemical vapour deposition (PECVD) and ion implantation.

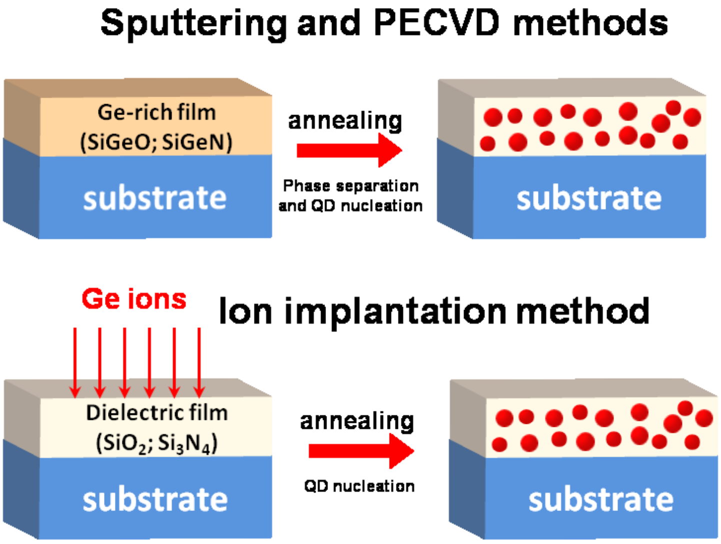

**Figure 3.1:** Schematic representation of Ge QD synthesis from annealing of Ge-rich films deposited by sputtering or PECVD method or by ion implantation of Ge.

As drawn in figure 3.1, in the case of co-sputtering and PECVD synthesis a Ge-rich dielectric film (e.g. a SiGeO or SiGeN alloy) is deposited on fused silica or Si substrates. Thermal annealing (during or after the film deposition) determines the phase separation of the film toward a nearly stoichiometric matrix ($SiO_2$ or $Si_3N_4$) and the concomitant nucleation and growth of Ge QDs [101] - [103]. In the case of ion implantation, Ge atoms are implanted into a stoichiometric oxide or nitride matrix. The Ge diffusion and the consequent nucleation and growth of QDs is induced by post implantation thermal annealing [97][104]. This preparation method is usually characterized by a higher concentration of matrix defect produced during the ion implantation process, that are partially recovered during the thermal annealing. However, ion implantation method allows the growth of Ge QDs in a stoichiometric and chemically stable matrix, while thermal annealing of SiGeO and SiGeN alloys could meet only to a partial phase separation and the presence of sub-stoichiometric compounds [105].

## 3.2 The role of the size

Size is one of the main parameters describing the optical behavior of confined structures. As the QDs size shrinks below the exciton Bohr radius (~24 nm for Ge [71]) a larger bandgap and increased oscillator strength is expected by quantum confinement effects. To deepen this point, in the following two sub-paragraphs we will investigate the role of the size on the light absorption process of Ge QDs embedded in $SiO_2$ matrix. Each sub-paragraph deals about the two synthesis techniques used: magnetron co-sputtering deposition and plasma enhanced chemical vapour deposition.

### 3.2.1 Structural and optical properties of Ge QDs synthesized by sputtering

Ge-rich $SiO_2$ thin films (hereafter SiGeO) have been obtained by rf-magnetron co-sputtering of $SiO_2$ and Ge targets ($5\times10^{-3}$ mbar Ar atmosphere, nominal deposition temperature 400°C), onto fused silica or (001) Si substrates. Different Ge concentration have been obtained by varying the power at the Ge target (from 30 to 70 W), while the power at the $SiO_2$ target was kept constant (500 W). The thickness of the SiGeO films were measured by transmission electron microscopy (TEM), while the elemental composition was determined by Rutherford backscattering spectrometry (RBS, 2.0 MeV He+ beam in random configuration, 165° backscattering angle). Figure 3.2 shows a typical RBS spectrum of our SiGeO films deposited on silicon substrate. Arrows indicate the signals due to Si, Ge and O in the SiGeO film (starting respectively at around 1600, 1150 and 750 keV of $He^+$ backscattered energy for the used configuration). All the investigated samples exhibit an homogeneous depth distribution of Ge atoms (as shown in figure 3.2) and have been fitted through SIMNRA software simulation in order to estimate the atomic content of Si, Ge and O in the films [106].

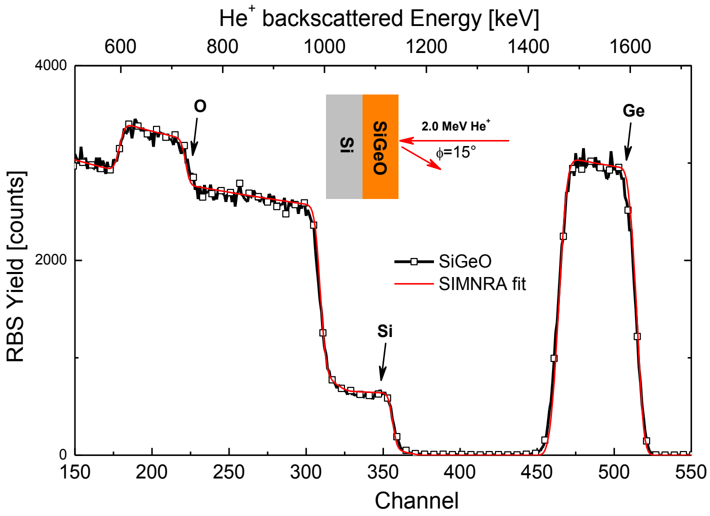

**Figure 3.2:** RBS spectrum and SIMNRA fitting of a representative SiGeO film deposited by magnetron sputtering on Si substrate. The experimental RBS setup is drawn in the figure.

Table 3.1 summarizes the values of thickness (from TEM) and Ge content (from RBS) evaluated for as deposited SiGeO films. The Ge content in SiGeO films increases with the rf-power at the Ge target, from 8% to about 18%, while the film thickness is around 250 nm for all samples.

| **Power at the Ge target [W]** | **Thickness [nm]** | **at. % Si** | **at. % Ge** | **at. % O** | **Ge content, D [at/cm$^2$]** |
|---|---|---|---|---|---|
| 30 | 210 | 27 | 8 | 65 | $1.15\times10^{17}$ |
| 40 | 300 | 24.5 | 11.5 | 64 | $1.77\times10^{17}$ |
| 50 | 250 | 24 | 16 | 60 | $3.0\times10^{17}$ |
| 60 | 290 | 22.5 | 18.5 | 59 | $3.4\times10^{17}$ |

**Table 1:** Film thickness (extracted by TEM) and stoichiometric content of SiGeO films deposited by rf-magnetron sputtering.

Thermal annealing in the range from 600°C to 800°C (1 h, $N_2$ atmosphere) promoted the phase separation of SiGeO film into $SiO_2$, $GeO_2$, and Ge clusters (due to precipitation of the excess of Ge in the alloy) [102]. SiGeO films deposited by sputtering can be described as a mixture of Ge, $GeO_2$, and $SiO_2$ units, according to a random matrix model, similarly to what occurs for silicon-rich oxide [107]. During annealing, Ge QDs undergo an Ostwald ripening mechanism, similar to the Si QD case [103], leading to a size increasing of precipitates with a concomitant amorphous to crystalline (*a*-*c*) transition occurring in the 600°C to 800°C temperature range [108]. At the same time, part of the Ge atoms out-diffuse from the sample surface as volatile Ge-O compounds with the increasing of the annealing temperature, as already evidenced in literature [108], [109]. In our case, such an out-diffusion is negligible up to 600°C (~5%) while it becomes significant for annealing above 800°C (20 to 40% of Ge out-diffused).

Cross-section TEM in high resolution (HR-TEM) or scanning mode (STEM) have been used to verify the formation of Ge clusters, to measure their size distribution, and to evidence the crystalline phase. A high density of Ge precipitates within the $SiO_2$ matrix is revealed by the STEM images (at the same magnification) in Figure 3.3, just after the deposition (a) and after thermal annealing at 750°C (b) for the SiGeO film with a Ge concentration of 16%. The bright patches represent Ge nanoclusters whose density and mean size noticeably change after annealing (the mean diameter increasing from 2.5 to 7.5 nm). Although amorphous (a-) Ge QDs are already present in the as-deposited films, the deposition temperature was not high enough to induce the formation of crystalline QDs in our case.

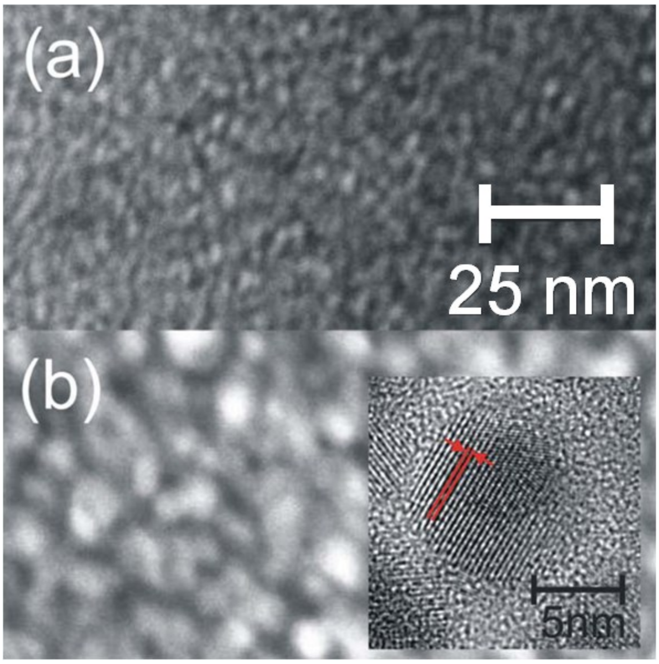

**Figure 3.3:** Cross sectional dark-field STEM images (same magnification) of the SiGeO film with 16% of Ge. As deposited (a) or after annealing at 750°C (b). The inset reports a HR-TEM of the annealed sample, showing the presence of a clear crystalline structure. From [102].

The inset in Figure 3.3 (b) reports an HR-TEM image of the annealed sample, evidencing a clear crystalline phase for Ge QD with the fringes due to crystalline planes (indicated by red lines and separated by 0.33 nm, as the (111) planes of c-Ge bulk). In Figure 3.4, the thermal evolution of mean QD diameter (2r) measured by TEM (diamond) and by glancing incidence X-ray diffraction (GI-XRD, crossed squares, the line is a guide for eyes) is reported. Even if GI-XRD gives information only for c-QDs, the reasonable agreement between the two techniques observed at 750°C supports the idea that the size distribution of c-QDs does not significantly deviates from that of a-QDs. Therefore, by joining the two techniques, is possible to follow the overall variation of the mean diameter with the annealing temperature, which shows a clear QD enlargement in the 400°C – 800°C range, in agreement with an Ostwald ripening growth mechanism [103].

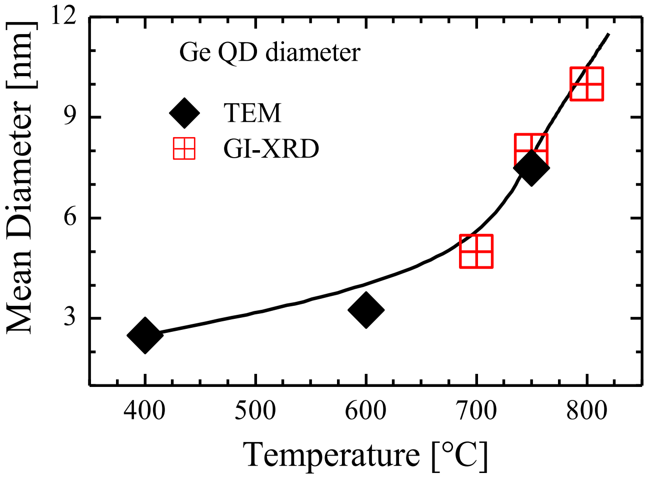

**Figure 3.4:** Thermal evolution of the mean diameter of Ge QDs measured by TEM (diamond) or GI-XRD (squares). Line is a guide for eyes. Adapted from ref. [102].

A similar evolution of the QD size can be obtained also by varying the concentration of Ge within the SiGeO films. As shown in figure 3.5, thermal annealing at 600°C (1h, $N_2$ atmosphere) induced the nucleation of small a-Ge QDs, whose size linearly increases from about 2 to 4 nm by increasing the Ge concentration from 8% (~$0.5\times10^{22}$ at/cm$^3$) to 18.5% (~$1.2\times10^{22}$ at/cm$^3$). In particular, we can give a rough estimation of the mean QD concentration by considering the atomic Ge content (*D*) measured by RBS and the QD mean size (*2r*) extracted by TEM analysis, under the assumptions that after annealing all the Ge in excess in the alloy is involved in the nucleation of spherical QDs and the atomic density ($\rho_{Ge}$) of QDs is equal to the bulk value. In this case, the number of Ge atoms in a spherical QD having size 2r is $N_{Ge} = 4/3\pi r^3 \cdot \rho_{Ge}$, while the concentration of Ge QDs within a layer of thickness *d* is simply: $C_{QDs} = \frac{D}{d \cdot N_{Ge}}$. Assuming a random distribution of QDs within the layer, the mean surface-to-surface QD distance (<*a*>) can be estimated as $< a >= 1/\sqrt[3]{C_{QDs}} - 2r$.

For all the investigated SiGeO samples annealed at 600 °C, we verified, a mean QDs concentration of the order of 0.7 - $1.2\times10^{19}$ QD/cm$^3$, corresponding to a mean surface-to-surface distance between adjacent QDs of around 2 nm.

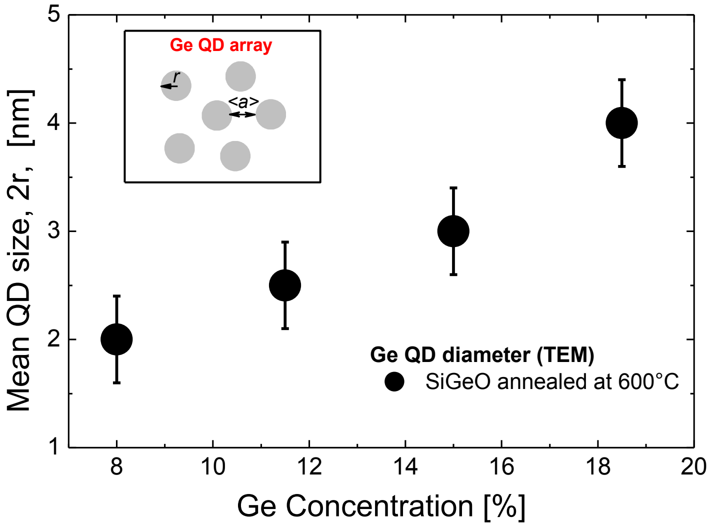

**Figure 3.5:** Evolution of the mean diameter of Ge QDs with the Ge concentration in SiGeO films annuale at 600°C in $N_2$.

Once the formation and growth of Ge QDs has been evaluated, the optical absorption properties are compared to determine the role of the QD size, if any, on the photon absorption mechanism. It is worth noting that the comparison among samples with different amount of Ge can be misleading as far as only the absorption coefficient α is concerned, since a different α can be trivially related to a different amount of absorbing centers. This problem can be overcome using the absorption cross section $\sigma$, defined as the absorption coefficient $\alpha$ normalized to the density, $D$, of atoms involved in the photon absorption process ($\sigma = \alpha \cdot d / D$) [99], [100]. The absorption cross section can then be used within the Tauc formalism as:

$$\sigma = \frac{B^*}{\hbar\omega}\left(\hbar\omega - E_g\right)^2 \tag{3.1}$$

where $B^*$ is a modified Tauc coefficient, having the same physical meaning of $B$, only scaled to the Ge atomic content of the specific sample. It should be emphasized that the use of $\sigma$ allows a rigorous comparison between samples with different density of absorbing centers.

Figure 3.6 shows the absorption cross section of different sizes of Ge QDs in $SiO_2$ films produced by sputtering after post-thermal annealing at 600°C. All the reported spectra have a featureless shape typical of an amorphous material. In particular, no resonance peaks at around 2.5 and 5 eV, related to direct optical transitions ($E_1$ and $E_2$) in c-Ge are visible [102], [110]. These results are in agreement with TEM analysis that revealed only amorphous QDs for this annealing temperature. As clearly shown in the figure, the size of QDs has a strong role on the photon absorption of our samples. In fact, the increasing of Ge concentration in SiGeO films ensures also the growth of larger QDs, inducing an evident increase of the absorption coefficient with a concomitant red-shift of the absorption energy onset. Such a size-dependent red-shift of the absorption onset could be an effect of quantum confinement occurring in these systems.

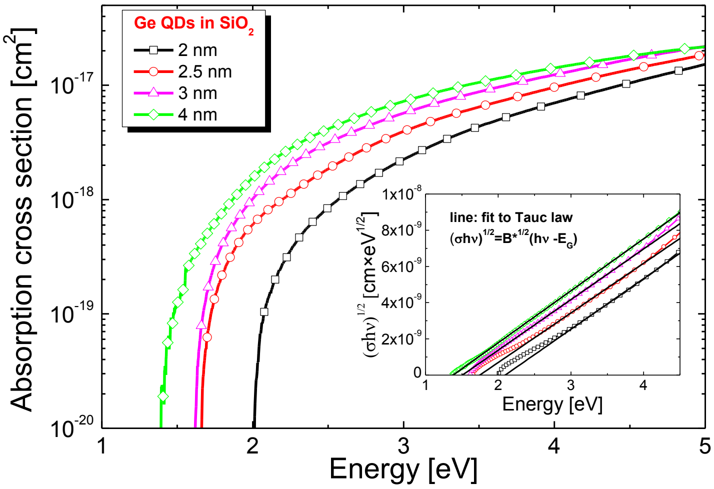

**Figure 3.6:** Absorption cross section, $\sigma$, of Ge QDs in $SiO_2$ for different QDs sizes. The inset shows Tauc plot and corresponding linear fits.

To better clarify the role of size on the light absorption in Ge QDs, we calculated their optical bandgap by applying the Tauc model, as described in the previous chapter. The consistence of this approach for QDs relies on the assumptions of non conservation of the ***k*** vector and on the parabolic band edges dispersion. The validity of such hypothesis, verified for a-Ge QW, holds also for Ge QDs, as indicated by the good linearity of Tauc plots in the inset of figure 3.6. Symbols in Fig. 3.7 summarize the values of the optical bandgap in our samples as a function of the QD size. Besides the role of size dispersion (related to the random QD nucleation in SiGeO single layers), Ge QDs in $SiO_2$ exhibit a clear size dependent shift of the optical bandgap. The largest Ge QDs (~4 nm) exhibit an optical bandgap of about 1.4 eV (well above the bandgap of not-confined a-Ge, ~0.8 eV, reported as a dashed line in figure 3.5) that increases to a value of about 2.1 eV when QD size shrinks to only 2 nm.

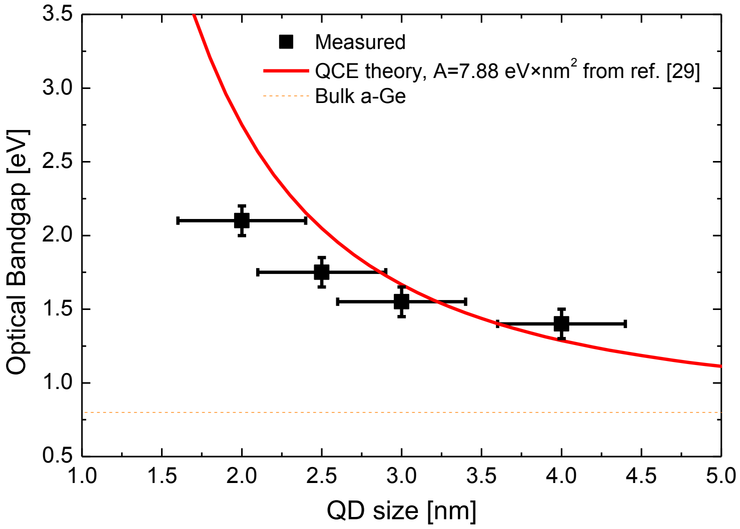

**Figure 3.7:** Optical bandgap as a function of size for Ge QDs in $SiO_2$. The value of amorphous bulk Ge (dashed line) as well as the theoretical trend of $E_g$ for Ge QDs according to ref. [29] are reported for comparison.

In order to understand if such a blue-shift is related only to quantum confinement effects, we plotted the expected valued of the optical bandgap for Ge QDs according to eq. (1.4) ($E_g(QD) = E_g(bulk) + A/L^2$) and used the value of $A$=7.8 eV×nm$^2$ calculated by Barbagiovanni et al. for strong confinement regime in Ge QDs [29].

Though the experimental values of the optical bandgap for the large QDs are in approximate agreement with the theoretical curve within the error bars, evident discrepancies occurs when the size decreases below 3 nm. The lower experimental values of $E_g$ indicate that other concomitant effects are playing a role in the absorption process, leading to a deviation from a pure quantum confinement regime. Such a deviation could be related to the large amount of disordered boundary shells at the interface with QDs that produce a dramatic change of the band structure of these systems. This is particularly true for the smaller QDs that exhibit a larger surface/volume ratio and are particularly sensitive to structural arrangement and the chemical ambient of the surrounding atoms with respect to larger QDs. For this reason, in order to better quantify the contribution of such a type of effects, in the following paragraph we will investigate on the synthesis and light absorption process of Ge QDs in $SiO_2$ prepared by PECVD technique.

### 3.2.2 Ge quantum dots by PECVD

Thin SiGeO films have been deposited by PECVD on fused silica or Si substrates kept at 250°C. Different Ge concentration (from 8% to 16%) have been obtained by varying the flux of $GeH_4$ while keeping constant the fluxes of $SiH_4$ and $N_2O$ precursors. The elemental composition of SiGeO films (as deposited or after thermal annealing at 800°C) was determined by RBS analysis and SIMNRA simulation of the experimental data, as previously explained. Small amounts of nitrogen (~5%) have been found in as deposited SiGeO samples, due to the contamination from $N_2O$ gas. Thermal annealing of SiGeO alloys induces nucleation and growth of small Ge precipitates embedded in $SiO_2$. We investigated, by TEM analysis, the average size of QDs after 800 °C annealing as a function of the Ge concentration. TEM image in the inset of Figure 3.8 (referred to the sample with the highest Ge concentration, ~16%) reveals the presence of Ge QDs as bright spots (due to high Z-contrast of QDs with respect to the $SiO_2$ matrix). Ge QDs in SiGeO films exhibit a mean size growing from about 3.5±1 nm to 8.5±2 nm with increasing the Ge concentration from $0.7\times10^{22}$ at/cm$^3$ (~8% Ge) to $1.3\times10^{22}$ at/cm$^3$ (~16% Ge). Despite the similar values of Ge concentration, QDs synthesized by PECVD method are larger compared to the ones synthesized by sputtering deposition, probably because of the higher annealing temperature used. However, such a larger annealing has been required in PECVD films to have a proper phase separation of the SiGeO alloy, in a similarly way to what observed also for Si-rich alloys [105].

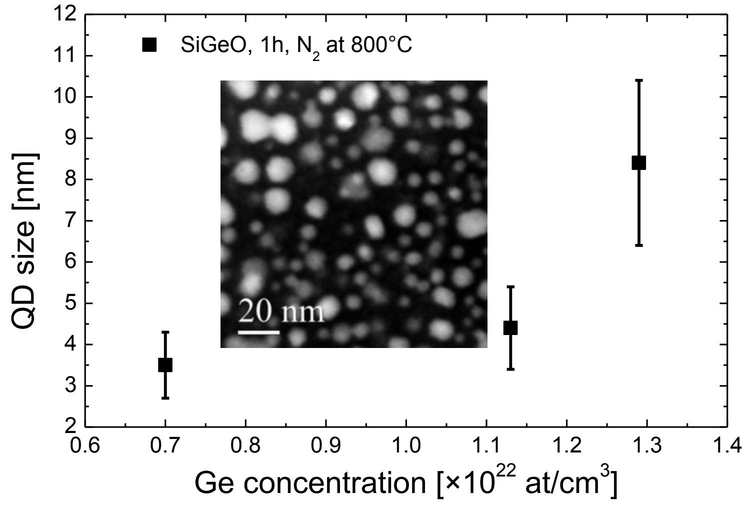

**Figure 3.8:** Mean QD size as a function of the Ge atomic concentration in $SiO_2$ films annealed at 800 °C. The inset shows a representative TEM image of Ge QDs in the film with the highest Ge concentration (16%).

For QDs synthesized by PECVD, also a different QD packaging is observed with respect to those produced by sputtering. In fact, by considering the QD mean size extracted by TEM, and assuming that after annealing all the Ge in excess in the alloy is involved in the QD nucleation, we can give a rough estimation of the QD concentration and surface-to-surface <*a*> values. For SiGeO samples synthesized by PECVD, QDs concentration ranges from ~$2.5\times10^{18}$ QD/cm$^3$ (<*a*> ~ 4 nm), for the sample with 10% of Ge, to a value of $3\times10^{17}$ QD/cm$^3$ (<*a*> ~ 7 nm), for the sample having 17.5% of Ge. These values of QD density and <a> distance must be taken as lower values, since in CVD preparation methods an incomplete precipitation of the Ge in excess cannot completely be ruled out [105]. However, by comparing the values of QDs concentration and <a> for PECVD films with those estimated for sputtered samples, a surely more tightly packed distribution of QDs emerges for the latter.

Once the formation and growth of Ge QDs in PECVD made matrices has been evaluated, the optical absorption properties were investigated to determine if the different deposition technique and a less dense packaging of QDs have an influence on the photon absorption mechanisms. Figure 3.9 reports the absorption coefficient spectra of as deposited and 800°C annealed SiGeO films for different Ge concentrations and sizes. As clearly shown in the figure, thermal annealing has a strong role on the photon absorption in SiGeO films, inducing an evident increase of the absorption cross section with a concomitant red-shift of the energy onset. A similar trend also occurs when the Ge concentration is increased. In fact, a higher Ge content within the films ensures the growth of larger QDs, giving rise to a larger absorption. This behavior, similar to that observed for QDs produced by sputtering, is in agreement with an effect of quantum confinement.

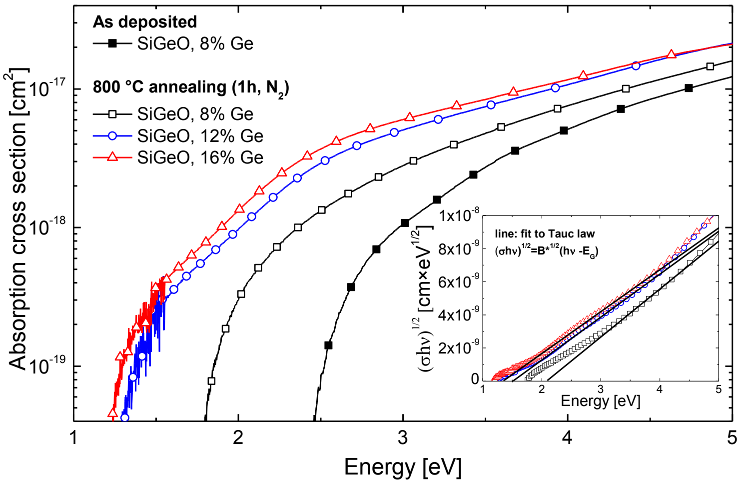

**Figure 3.9:** Absorption cross section spectra of as deposited (closed symbols) and 800°C annealed (open symbols) SiGeO films for different values of Ge concentration. The inset shows Tauc plot and corresponding linear fits.

Squared symbols in Figure 3.10 summarize the optical bandgap values for Ge QDs synthesized by PECVD, extracted with the Tauc plot method, as a function of the QD size. Ge QDs in $SiO_2$ display a blue-shift of about 1 eV by shrinking the size down to 3-4 nm. In order to understand if this blue-shift is attributable to quantum confinement effect only, $E_g$ values have been fitted within the effective mass theory according to the relationship for the infinite potential barrier case: $E_g(QD) = E_g(bulk) + A/L^2$, were $E_g^{bulk}$ was fixed at the bandgap value of a-bulk Ge (0.8 eV), while $A = \pi^2\hbar^2/2m^*$ was the only fitting parameter.

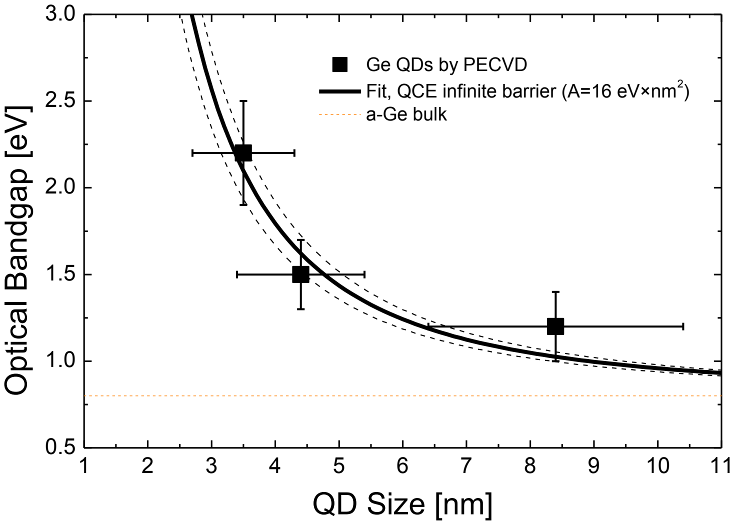

**Figure 3.10:** Experimental values of the optical bandgap versus the size of Ge QDs grown after thermal annealing at 800 °C of SiGeO films deposited by PECVD (squares). The black solid line was obtained through fitting from the effective mass theory for three-dimensionally confined a-Ge QDs in $SiO_2$ by PECVD (infinite barrier case), obtaining a value of confinement parameter $A = 16 \pm 2\, eV \times nm^2$. Dashed black lines represent the uncertain of the confinement parameter. Small dashed line represents the optical bandgap of unconfined a-Ge.

The good fitting agreement shown in figure 3.10 for QDs produced by PECVD confirms that the observed size dependent shift of $E_g$ for Ge QDs in $SiO_2$ is ascribed to QCE and $SiO_2$ matrix acts as an infinite barrier for confined carriers. In particular, we found a value of the confinement coefficient of 16±2 eV×nm$^2$, resulting in a very strong confinement for carriers in a-Ge QDs. Such a value is about 3 times larger than the *A* value obtained for the case of single a-Ge QW embedded in $SiO_2$ (4.35 eV×nm$^2$) investigated in chapter 2. Actually, such an increment of the confining parameter is fully expected by theory. In fact, *A* is proportional to $1/m^* = 1/m_e^* + 1/m_h^*$ (where $m_e^*$ and $m_h^*$ are the electron and hole effective masses, respectively) and the effective masses are assumed to be isotropic for the three confinement directions in amorphous materials. Therefore, the confinement coefficient for a-QDs is expected to be 3 times larger than for a-QW. In a-Si nanostructures, the *A* parameter was experimentally observed by Park et al. to increase by a factor of 3 going from 2D (QWs) to 0D (QDs) confines structures [111]. This evidence further supports the predominant role of quantum confinement and the goodness of Tauc method for the experimental evaluation of the optical behavior of Ge QDs in $SiO_2$.

### 3.2.3 Quantum confinement: a solo player?

Recently, Barbagiovanni et al. reported the values of *A* calculated using EMA approach for c-Si and c-Ge nanostructures [29]. While a good agreement with experimental data for Si is found, some discrepancies arise for Ge NCs which experimentally exhibit a stronger confinement effect with respect to what theory predicts. This is shown in figure 3.11 (a), where the theoretical $E_g$ curve using the value of *A* given by Barbagiovanni et al. ( $A = 7.8\, eV \times nm^2$ ) does not match with experimental values for Ge QDs produced either by PECVD or sputtering [29]. Moreover, we can observe that the optical bandgap of QDs in $SiO_2$ strongly differs between the two synthesis techniques. Surprisingly, QDs grown by sputtering evidence a bandgap values well lower than the ones synthesized by PECVD technique and clearly not following the QC relationship, not for the *A* value given by us and not even for the one calculated by Barbagiovanni et al. [29].

To further clarify this point, the absorption efficiencies of QDs synthesized by sputtering or PECVD are compared in figure 3.11 (b). A different trend between the two types of QDs is observed. The absorption efficiency increases with the reduction of the QD size for PECVD samples. This behavior, similar to what observed for the a-Ge QWs, is ascribed to the larger optical oscillator strength as the dimensions of the system is reduced. On the contrary, the same effect does not occur for QDs synthesized by sputtering technique. In this case any increase of the oscillator strength is observed by shrinking the QDs size, as one should expect from theory.

From a comparison of the trends reported in figure 3.11 (a) and (b), it is interesting to observe that QDs synthesized by PECVD are fairly well described by QCE for what concerns both the optical bandgap and absorption efficiency. On the contrary, QDs synthesized by sputtering deviate from a pure quantum confinement regime in both cases, tough some effects of quantum confinement are still observable as far as the size-dependent shift of the optical bandgap concerns. This behavior is quite surprising, since we would expect a more "ideal" case for QDs produced by sputtering technique. In fact, Ge-rich alloys deposited with this technique typically exhibit a larger phase separation with a more stoichiometric stability with respect to PECVD and, moreover, the absence of nitrogen contaminations [84][105]. This suggests that beyond the role played by QDs interface defects and the amount of Ge-O or Ge-N bonds, other effects control the light absorption mechanism of QDs.

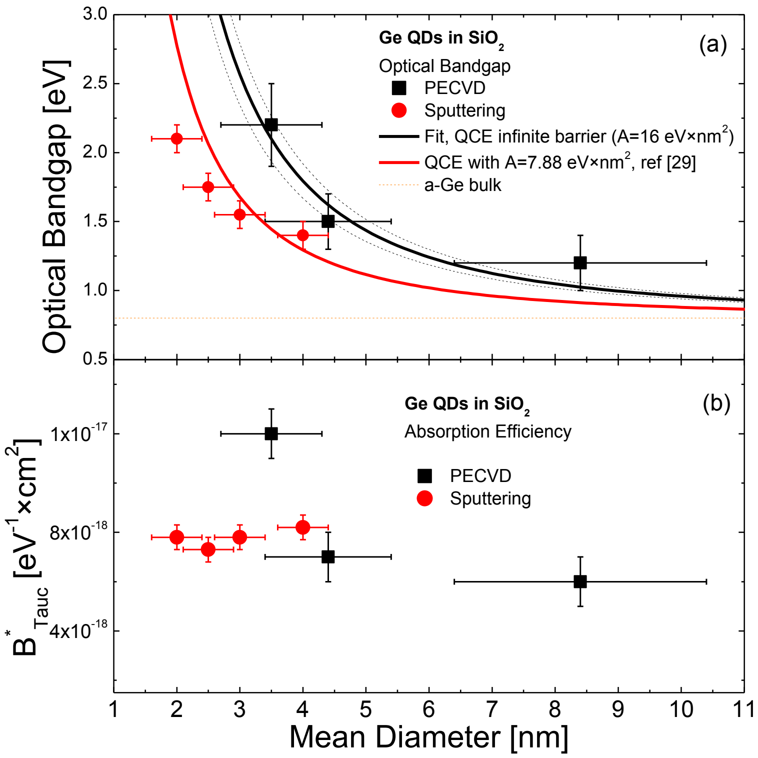

**Figure 3.11:** (a) Experimental values of the optical bandgap versus the size of Ge QDs grown after thermal annealing at 800 °C of SiGeO films deposited by PECVD (squares) or sputtering (circles). The black solid line was obtained through fitting from the effective mass theory for three-dimensionally confined a-Ge QDs in SiO$_2$ by PECVD (infinite barrier case), obtaining a value of confinement parameter $A = 16 \pm 2\, eV \times nm^2$. Red line represents the theoretical bandgap calculated by Barbagiovanni et al. for c-Ge QDs under strong confinement regime [29]. Small dashed line represents the optical bandgap of unconfined a-Ge. (b) Absorption efficiency ($B^*_{Tauc}$) of Ge QDs in SiO$_2$ synthesized by PECVD or sputtering technique as a function of QD size.

Actually, a reason for the different optical behavior shown by QDs in SiO$_2$ synthesized by sputtering or by PECVD could be related to the different

QD packaging in the two systems. In fact, several theoretical and experimental studies indicate that the QDs spacing and arrangement can play an important role in the optical properties of these systems. In a recent paper, Guerra et al, calculated the electronic structure of Si nanocrystals (NCs) and the role of the strain induced by a surrounding $SiO_2$ matrix or induced by lowering the distance in between the NCs [112]. According to their calculations, the strain produced at the QD/matrix interface produces a red shift of the absorption spectra. In particular, for nanocrystals smaller than 2 nm the proportion of atoms at the $Si/SiO_2$ interface becomes relevant, producing surface-related states that affect the quantum confinement appearing as inner band gap states and then drastically changing the optical response of the system [117]. In particular, they demonstrated that for a NC-NC separation lower than 0.5 nm strain-induced forces mutually acting on the NCs emerge, playing an important role over any kind of NC-NC interaction mechanisms. Such calculations are also in substantial agreement with the results reported by Hapala et al., which observed a systematic blue-shift (~200 meV) of the bandgap for free-standing oxide-passivated Si nanocrystals compared to the matrix-embedded ones having the same size [113]. They explained their experimental results as the effect of compressive strain exerted on the nanocrystals by the embedding matrix. Finally, Uhrenfeldt et al. recently observed that the absorption of large and closely packed Ge NCs in $SiO_2$ ordered in multi-layers exceeds that for similar concentration of NCs randomly distributed in the film [99]. They found indications that the order distribution and packaging of Ge NCs play an important role on the optical response of these systems and can prevail on the effects due to quantum confinement.

A similar behavior, in which mutual coupling effects between closely packed QDs take place, can account for the different optical response between QDs produced by PECVD or sputtering. In fact, in our case the Ge QDs produced by these two techniques differ for the density and packaging of QDs. As previously described, annealing at 600°C of sputtered SiGeO films results in the nucleation of a very tightly packed array of small QDs having a spacing not larger than 2 nm. By varying the Ge concentration in the SiGeO film larger QDs nucleate, but the spacing remains roughly constant. On the contrary, thermal annealing at 800°C of SiGeO films produced by PECVD results in the growth of nearly isolated QDs, having a QD-QD spacing of the order of 4- to 7 nm. Thus, the reduced QD-QD spacing in samples produced by sputtering could be responsible for the observed deviation from a pure QCE regime, in particular for what concerns the size-dependent bandgap tuning and the constant oscillator strength. When the QD spacing is larger enough, as in the PECVD case, QCE dominate over the effects of interacting QDs.

## 3.3 The role of the distance

In order to clarify if and to what extent QD-QD interactions can modify the light absorption process, we will present, in the following paragraph, an experimental effort conceived to separate the dependence of the light absorption on size and QD-QD distance by using a multilayer approach. A clear evidence of light absorption enhancement by decreasing the QD-QD distance is presented and discussed.

### 3.3.1 Experimental design

In this experiment, multilayered samples (as drawn in Figure 3.12) have been fabricated by repeating 15 times the film/barrier ($SiO_2$:Ge/$SiO_2$) structure, by magnetron co-sputtering deposition from $SiO_2$ and Ge targets ($2\times10^{-3}$ mbar *Ar* deposition pressure, substrate temperature of 400 °C), fused silica quartz substrates. After a $SiO_2$ buffer layer, thin films (4 nm) of $SiO_2$:Ge were alternated to pure $SiO_2$ barriers, whose thickness was varied to produce samples with tightly packed or fairly isolated Ge QDs along the growth direction. The multilayer structure and thickness, as well as the presence of Ge QDs were evaluated by cross sectional Transmission Electron Microscopy (TEM) analysis, through a JEOL 2010F microscope at 200 kV operated in conventional bright field mode TEM. The atomic Ge content in the films was measured by Rutherford Backscattering Spectrometry (RBS, 2.0 MeV $He^+$ beam, 165° backscattering angle). The absorption coefficient spectra have been obtained by combining the transmittance and reflectance spectra (200 up to 2000 nm wavelength range) with a Varian Cary 500 double scanning UV-VIS-NIR spectrophotometer, as previously described.

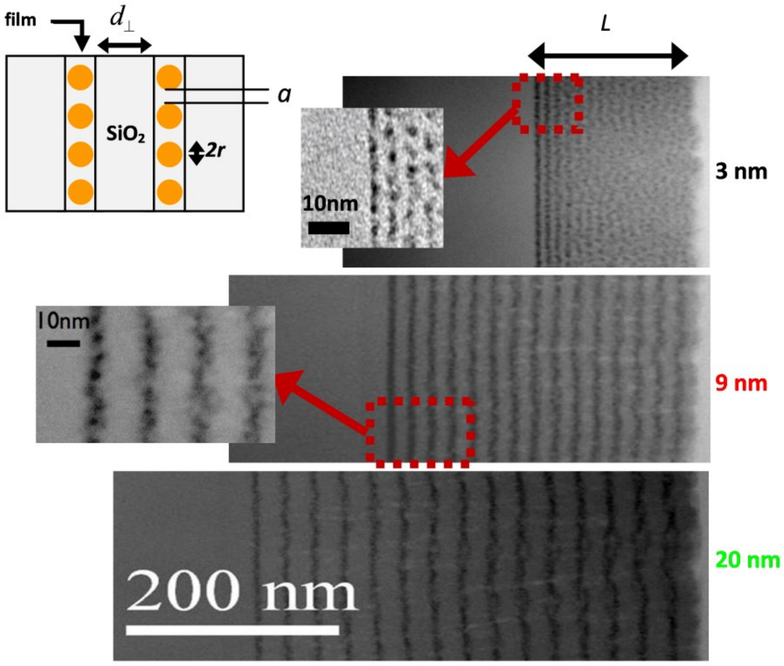

**Figure 3.12:** Schematic and cross sectional Bright field (BF)-TEM images of Ge QDs multilayered samples with different thicknesses of $SiO_2$ barriers. BF-TEM image marked by the red arrows shows the multilayer of Ge QDs with the thinnest and medium $SiO_2$ barrier. From ref [100].

The structural characterization of the Ge QDs multilayers are summarized in Figure 3.12. Bright field TEM images show the structure of the films with pure $SiO_2$ barriers (brighter layers) embedding very thin films containing Ge QDs dispersed in $SiO_2$ (darker layers). The thickness of the $SiO_2$ barrier ($d_\perp$) was 3 nm for the tightest QDs configuration (total sample thickness, *L*, of 106 nm), 9 nm for the intermediate packaging (*L* of 245 nm), and 20.4 nm for the most spaced one (*L* of 439 nm). The multilayered configuration also allows a better control of the size and vertical order distribution of Ge QDs. In fact, the bright field BF-TEM image (left side of Fig. 1) shows in detail the tightest QDs configuration sample with the clear presence, in each film, of one layer of small (3 nm in diameter) and densely packed amorphous Ge QDs. From the RBS spectra (not shown here) we found that the Ge content (*D*) is fairly the same in the three samples, being around $6.5\times10^{16}$ Ge/cm$^2$ and giving out an areal density of ~$4.3\times10^{15}$ Ge/cm$^2$ within each QDs layer. Basing on TEM evidences, we can assume spherical QDs with an average diameter (*2r*) of 3 nm, thus a mean QDs areal density of ~$7\times10^{12}$ QD/cm$^2$ in each layer, corresponding to a surface-to-surface distance (*a*) of about 1 nm between adjacent Ge QDs in the same layer. As the *a* value is fixed and well lower than $d_\perp$, the multilayer approach used here allows to play only with the distance between Ge QDs films along the growth direction. In other words, in multilayer samples the QD-QD distance can be varied only in the vertical direction, while it is fixed in the plane of the QDs film, this last value depending only on the Ge concentration in each layer.

### 3.3.2 Modulating the absorption efficiency

In order to properly compare the light absorption by Ge QDs arranged in the three multilayered samples and to verify if the QDs arrangement plays a role in the process, we used the atomic absorption cross section [14] ($\sigma = \alpha \cdot L / D$, where $\alpha$ is the absorption coefficient spectrum, *L* is the sample thickness measured by cross section TEM, and *D* the Ge atomic content obtained by RBS measurements). In fact, as *L* is different in the three samples, the analysis based on the comparison among *α* spectra would be misleading. The different amount of Ge in each sample requires the use of *σ*. Thus, if the QD configuration and distance do not play any role in the light absorption, σ should be the same for all samples. Instead, this is not strictly the case, as shown in Figure 3.13 (a), where we report σ for multilayered samples with Ge QDs films spaced by barriers of 3, 9 and 20 nm (squares, circles and triangles, respectively). The measured *σ* spectrum for unconfined amorphous Ge is reported for comparison. Errors on the *σ* values (coming from indetermination on *α*, *L* and *D*) are comparable with the symbol size.

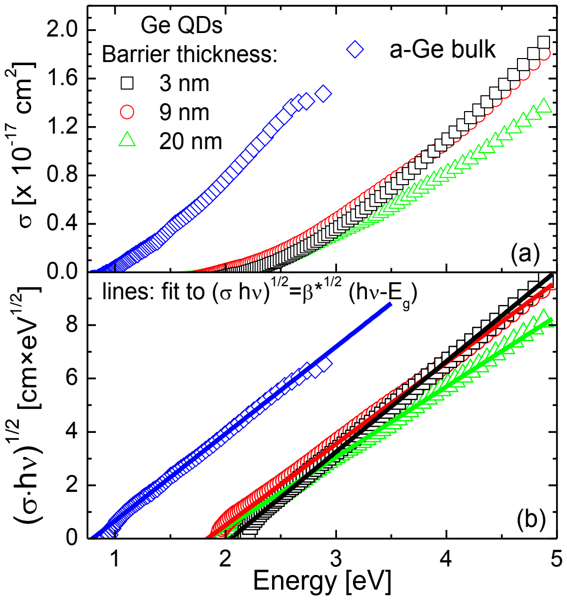

**Figure 3.13:** Atomic absorption cross section (*σ*) spectra for Ge QDs multi-layers with different $SiO_2$ barrier, together with the σ spectra of amorphous bulk Ge. (b) Tauc plot (symbols) and corresponding linear fits (lines) for Ge QDs arranged in multi-layers and amorphous bulk Ge film. Adapted from ref. [100].

In all the cases, the absorption cross section of QDs is clearly lower than for bulk Ge, in agreement with ref. [85]. Of course, this is related to the different onset energy, much lower for bulk Ge, due to QCE. All the σ spectra of Ge QDs show a similar onset at about 2 eV, while the multilayer with the largest barrier clearly has the worst performance. By using this procedure we compare the experimental absorption efficiency of Ge QDs arranged in different configuration, in order to put in evidence the effects related to the QD-QD spacing, if any. It is also worth of noting that the rate of increase in the $\sigma$ spectra is higher for the smaller barrier multilayer sample. This is an experimental evidence that closely packed Ge QDs produce an enhancement of the light absorption.

With the aim of clarify this aspect, we used the (modified) Tauc model (eq. 3.1), applied to the absorption cross sections, to extract the values of $E_g$ and $B*$ for our materialsIt must be stressed that the use of σ allows a rigorous comparison between samples with different density of absorbing centres, while the $B*$ coefficient lets to suitably compare samples with different optical bandgap. Once again, the validity of this approach also for Ge QDs vertically ordered in multi-layers is ensured by the good linearity of the Tauc plots, as reported in Figure 3.13 (b). This allow to directly extract the values of $E_g$ and $B*$ by a linear fit.

Figure 3.14 summarizes the optical bandgap, $E_g$, of the multilayer samples as a function of the barrier thickness. All the QDs arranged in the multilayer samples(square data), independently of the barrier thickness, exhibit the same optical energy gap (1.9±0.1 eV), well above that of unconfined amorphous Ge (~0.8 eV, measured with the same technique and reported as blue rectangle in Figure 3.13). In addition, since all QDs have a similar size (2r ~ 3 nm) we do not expect any variation of $E_g$ because of QCE, as indeed clearly occurs in our case.

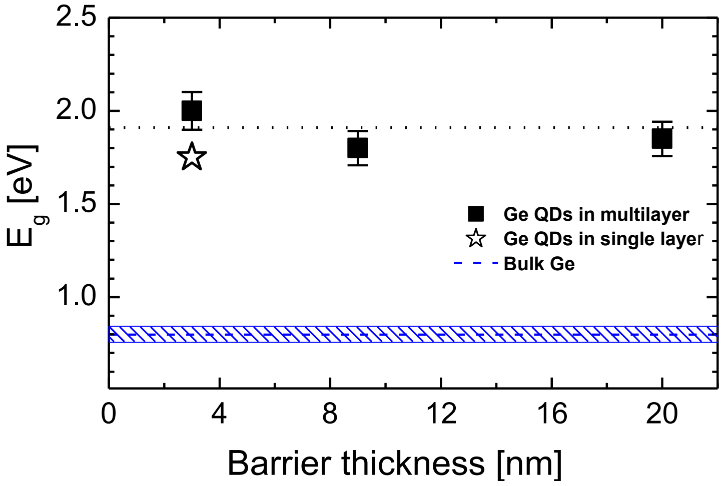

**Figure 3.14:** Experimental values of energy gap ($E_g$, squares) of Ge QDs arranged in multilayers with different $SiO_2$ barrier thicknesses. For comparison the $E_g$ values are reported for amorphous bulk Ge (rectangle) and Ge QDs in a single layer (star) configuration. Adapted from ref. [100].

The modified Tauc coefficient $B^*$ *vs* the barrier thickness is reported in Figure 3.15, showing a clear decrease with the spacing of Ge QDs. This evidence is directly linked to the observed enhancement of the light absorption cross section in closely packed Ge QDs, as $B^*$ represents a sort of absorption efficiency, independent of the optical bandgap. In particular, in the closest packed configuration, such absorption efficiency is almost doubled with respect to the case of the most spaced Ge QDs. To get a basis for comparison, we experimentally extracted the modified Tauc coefficient $B^*$ for unconfined amorphous Ge, reported as a blue rectangle in Figure 3.15 (which thickness is proportional to the experimental error). Such a value is in agreement with that for the closest packed QDs, while other samples show a lower absorption efficiency in comparison to bulk material.

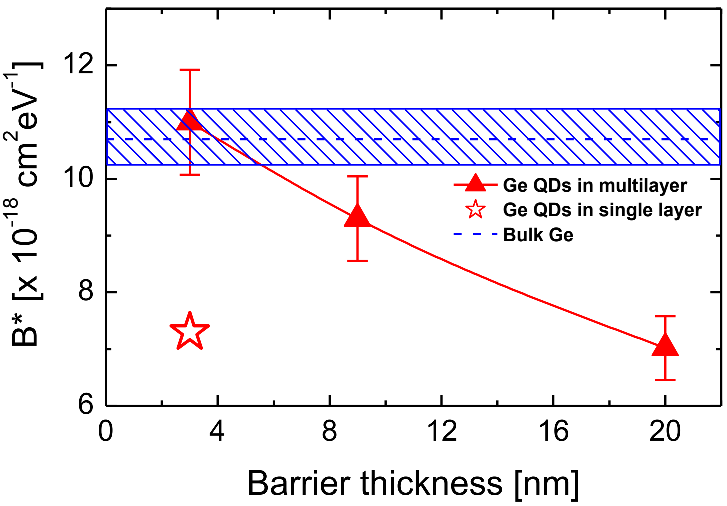

**Figure 3.15:** Experimental values of absorption efficiency (B*, squares) of Ge QDs arranged in multilayers with different $SiO_2$ barrier thicknesses. For comparison the *B** values are reported for amorphous bulk Ge (rectangle) and Ge QDs in a single layer (star) configuration. Adapted from ref. [100].

Even if this deposition approach allows to modify the QD-QD distance only in the vertical direction, some general consideration can be drawn. Thus, as far as the light absorption mechanism is concerned, the quantum confinement in Ge QDs clearly increases the optical bandgap with respect to the bulk, but it does not give a clear advantage on the light absorption efficiency. Instead, by using well spaced Ge QDs an evident loss occurs in the efficiency of the absorption process. Such an effect has been observed in our samples up to 20 nm of QD-QD vertical spacing. To account for the effect of a three dimensional (3D) QD-QD spacing on the absorption efficiency, a sample with a single layer (~250 nm thick) of $SiO_2$:Ge was fabricated and characterized by the same procedure. Ge QDs of similar diameter have been found, with a mean surface-to-surface distance (now in 3D) of 3 nm. This single-layer sample can be compared with the multilayer sample with a barrier thickness of 3 nm, to account for the modulation of

$d_{\perp}$, the in-plane QD-QD distance. The single layer sample shows an optical bandgap of 1.7 eV (star in Fig. 3.14), as expected for the fixed QD diameter, still an absorption efficiency (star in Fig. 3.15), well lower than the multilayer sample with the smaller barrier thickness, and comparable with the largest barrier thickness. In other words, when Ge QDs are spaced by 3 nm in 3D, they absorb as much as in a multilayer configuration with 20 nm of 1D spacing (vertical growth direction) and 1 nm of 2D spacing (in plane within each layer). All these data evidence that the QD-QD spacing plays a key role in the photon absorption process. Therefore, some long range interaction between QDs has to be assumed to account for the observed effect. Actually, the presence of electronic coupling between semiconductor nanoparticles has been theoretically described [114],[115], for which energy transfer occurs between semiconductor nanocrystals up to 10-20 nm apart, mainly by means of dipole-dipole interactions. This effect is typically observed in light emission spectroscopy [116]. If some electron coupling occurs between closely packed Ge QDs, it should affect the electron transition probability and then the light absorption mechanism. On the other hand, as the QD-QD distance within the film is quite short ($d_{\perp}$ ~1 nm), a kind of collective behavior cannot be excluded at all, as if the interaction responsible for the light absorption enhancement occurs between the ensembles of Ge QDs contained in each film.

These findings demonstrate how the optical response of an ensemble of QDs can be affected by proximity effects between adjacent QDs that significantly modify the strength of the optical absorption, even dominating the effects due to the confinement. Anyway, this effect can be further exploited for enhancing the absorption by nanostructure materials for light harvesting applications.

## 3.4 The role of the matrix

Besides the NS size, one of the main parameter contributing to define the optical properties of NS is the confining potential barriers offered by the matrix where NS are embedded. According to theory, by reducing the height $V_0$ of the potential barriers a lower confinement of the electron-hole pair occurs. In fact, eq. (1.4) is valid in the case of an infinite confining barrier potential. Eq. (1.4) is still acceptable for NS embedded in $SiO_2$, because of the much larger confining barrier height with respect to the typical energy level values of confined electron-hole pairs [27]. However, for a lower barrier height $V_0$, the value of $E_g$ given in eq. (1.4) is reduced by the factor $\left[1+\frac{\hbar}{r\sqrt{2m^*V_0}}\right]^2$. Hence, lower potential barriers reduce the strength of quantum confinement. In addition, the optical behavior of QD can also be largely affected by other matrix effects, e.g. defects, un-passivated bonds, QD/matrix interface states [91][97][102][117]. In this regard, also the type and stoichiometric quality of the matrix can play a strong role on the nucleation and growth of NS, leading in turn to a different optical response of the system.

For this reasons, a crucial step towards applications and devices is to understand the influence of the hosting matrix on the light absorption mechanism and QCE in NS. In the following sub-paragraphs, the synthesis and optical properties of Ge QDs embedded into $Si_3N_4$ or $SiO_2$ fabricated by ion implantation or PECVD techniques are presented and compared, giving insights on the role of the host for what concerns both the synthesis and optical properties of Ge QDs.

### 3.4.1 Ge quantum dots by ion implantation

The synthesis of Ge QDs by ion implantation has been realized by implanting $Ge^+$ ions in $Si_3N_4$ or $SiO_2$ matrices, followed by thermal annealing. Implant energy (100 keV) and fluence ($7.3\times10^{16}$ Ge ions/$cm^2$) were chosen to induce the QDs precipitation within 90 nm from the surface. Even if the energy loss for incoming ions is slightly larger in $Si_3N_4$ than in $SiO_2$, the projected ranges came out to be ~ 45 nm in both [118], as shown in the RBS spectra of Ge implanted profile reported in figure 3.16. Once implanted, the matrices were subjected to furnace annealing processes up to 900°C (1 hour, $N_2$ ambient). Large differences arise in the formation of Ge QDs in $Si_3N_4$ or in $SiO_2$, as evidenced by the STEM images in Figure 3.16 referring to the implanted films annealed at 850 °C. Ge QDs appear as bright spots, due to the higher Z-contrast of Ge with respect to both matrices. The QDs layer appears to be placed in the 20-90 nm depth range, in agreement with the expected projected range. The QD diameter ($2r$) is much larger in $SiO_2$ ($2r$ ~ 3–24 nm) than in $Si_3N_4$ ($2r \leq$ 2-3 nm). Moreover, as evidenced by electron diffraction analysis (shown in the insets of Figure 3.16), Ge QDs in $SiO_2$ are crystalline, contrary to the $Si_3N_4$ case, where no diffraction spots are observed. The same also holds after annealing at 900°C (STEM images not shown here). Despite the high annealing temperature (Ge melting point is 938 °C), Ge QDs into $Si_3N_4$ matrix are surprisingly amorphous and small in size. Studying Ge QDs in $Si_3N_4$, obtained by magnetron sputtering technique, Lee *et al.* observed that large and crystalline QDs only form for very high Ge concentration and for temperatures as high as 900°C [119]. On the other side, it was shown that Ge clusters in $SiO_2$ during annealing undergo Ostwald ripening and crystallization for temperatures higher than 700 °C [102][108].

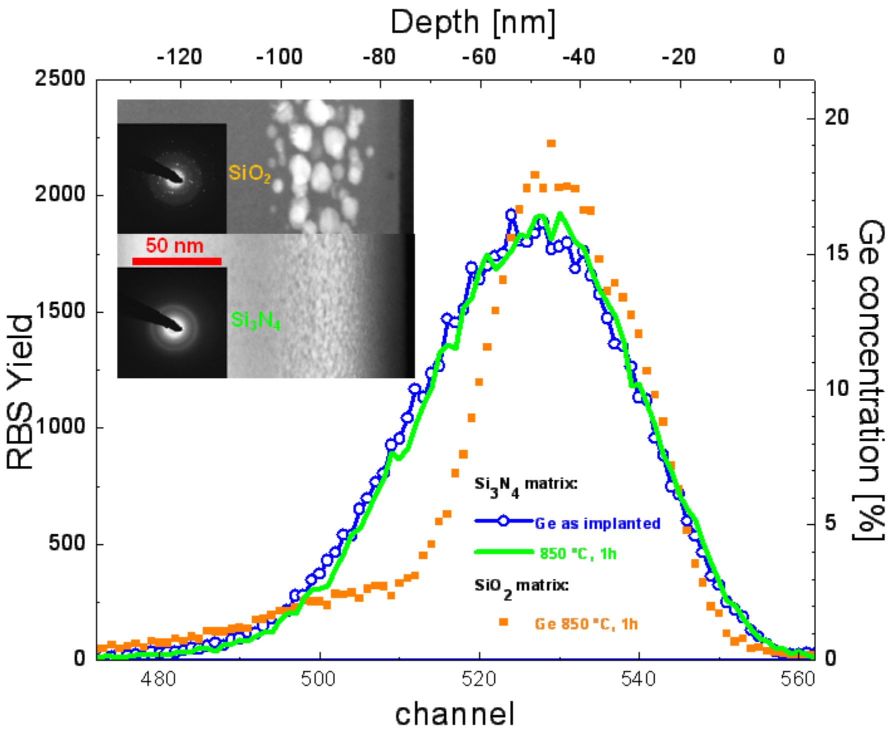

**Figure 3.16:** Rutherford backscattering spectrometry performed on Ge implanted (continuous line) and annealed (circles) $Si_3N_4$ or in annealed (squares) $SiO_2$. Top and right axes have been calculated after a proper calibration for depth and Ge fluence. The inset shows cross sectional high angle annular dark-field STEM images of the Ge nanoclusters embedded in $Si_3N_4$ or in $SiO_2$ matrices, obtained after Ge ions implantation (100 keV, $7.3\times10^{16}$ cm$^{-2}$) and annealing at 850°C, 1h. Larger Ge nanoclusters are observed in the $SiO_2$ matrix. Electron diffraction images for the two samples are shown.

These evidences together with our data clearly prove that embedding matrix significantly affects the formation of Ge QDs. In the $Si_3N_4$ case we propose that the ripening of Ge nuclei can be limited by a low Ge diffusivity. Actually, the Ge diffusivity in $Si_3N_4$ can be much smaller than in $SiO_2$, as it occurs for Si diffusivity (~$3\times10^{-13}$ cm$^2$/s at 800°C in $SiO_2$ [109], ~$1\times10^{-24}$ cm$^2$/s at 840°C in $Si_3N_4$ [120]). To verify this we employed RBS technique in Ge implanted $Si_3N_4$, comparing the He backscattered energy spectra in the as-implanted (line + circles) and 850°C annealed (continuous line) samples, as shown in figure 3.15. After annealing neither the implanted Ge content nor its profile is changed in $Si_3N_4$. In $SiO_2$ matrix a small fluence loss (~6%) was measured (not shown here). Basing on the thermal budget (850°C, 1h) and depth resolution (5 nm), Ge diffusivity in $Si_3N_4$ at 850 °C cannot be larger than $7\times10^{-17}$ $cm^2/s$. This low diffusivity and the STEM images point out that while at 850°C Ge migrates in $SiO_2$, leading to QD ripening and Ge out-diffusion, at the same temperature Ge diffusion in $Si_3N_4$ is very low, reducing the QD ripening in $Si_3N_4$.

The lack of crystalline phase in Ge QDs in $Si_3N_4$ can be related to their small size. According to the classical nucleation theory, a critical radius ( $r^* = \frac{-2\gamma}{\Delta G_{phase}}$ ) exists, above which the amorphous to crystalline transition lowers the free energy, since for large nuclei the extra interfacial energy ($\gamma$) is compensated by the gain in the internal free energy ($\Delta G_{phase}$) due to crystallization [121]. Recently, the Ge/$Si_3N_4$ interface was shown to have a larger $\gamma$ in comparison to the Ge/$SiO_2$ one [28]. This supports a larger critical radius for Ge QDs in $Si_3N_4$ (since $\Delta G_{phase}$ is not affected by the matrix, at a first approximation) justifying the lack of crystalline Ge QDs in the $Si_3N_4$ samples. Thus, the larger interfacial energy and the reduced diffusivity of Ge in $Si_3N_4$ limit the QDs ripening and crystallization. This means that the kinetics of NC formation and crystallization is much slower in $Si_3N_4$ than in $SiO_2$.

Once evaluated the Ge QDs formation in the two matrices, the optical properties were compared to evidence the role of the matrix, if any, on the photon absorption mechanism. As the QD formation is affected by the matrix, the comparison of light absorption was done for samples annealed at 700°C, which are expected to give comparable Ge QDs (amorphous and 2-4 nm sized) in both kind of matrices. As clearly shown in Figure 3.17, the values of $\sigma$ are 3-4 times larger for QDs in $Si_3N_4$ than in $SiO_2$.

This finding evidences a strong role of the matrix in the photon absorption, pointing out that $Si_3N_4$ matrix allows Ge QDs to absorb light much more efficiently than $SiO_2$. Such an effect can be profitably used for any light sensing application of Ge QDs.

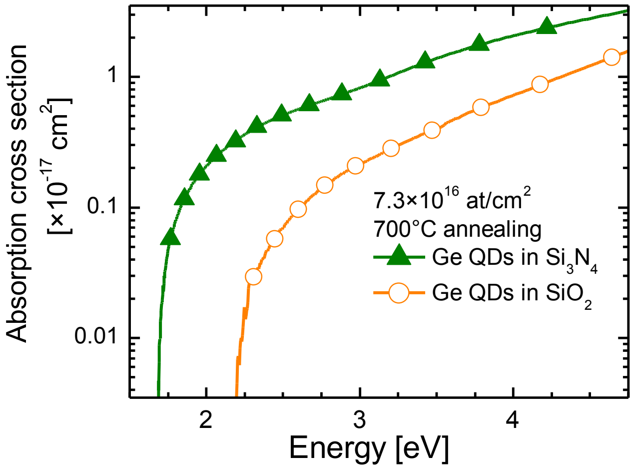

**Figure 3.17:** Atomic absorption cross section spectra for Ge nanoclusters embedded in $Si_3N_4$ or $SiO_2$ (700°C annealing after 100 keV Ge implant at 7.3 ×10$^{16}$ Ge/cm$^2$ dose). Adapted from ref. [97].

Tauc plots are reported with symbols in Figure 3.18 for samples implanted in $Si_3N_4$ (triangles) or $SiO_2$ (circles) matrices. Plots show a kink [indicated in by an arrow for the $Si_3N_4$ sample] above which the trend is linear, according to the Tauc model. Below the kink, transitions can occur involving electronic states in the band tails or in the midgap, for which the Tauc law is no longer valid. Implantation damage can create midgap or tail states in the band structure which account for the deviation from linear absorption trend observed in the Tauc plots below the kink [97]. Because of this, a univocal determination of $E_g$ cannot be performed, but still Tauc plots can be fitted above the kink (lines in Fig. 3.16), giving an onset energy for light absorption ($E_{ON}$, $\propto$ energy for which absorption coefficient is larger than $10^4$ $cm^{-1}$ [97]). Ge QDs in $Si_3N_4$ (triangles) show a smaller $E_{ON}$ (~1.9 eV) than in $SiO_2$ (~2.5 eV). In both matrices NCs exhibit $E_{ON}$ larger than that of unconfined amorphous Ge (~0.8 eV), due to QCE.

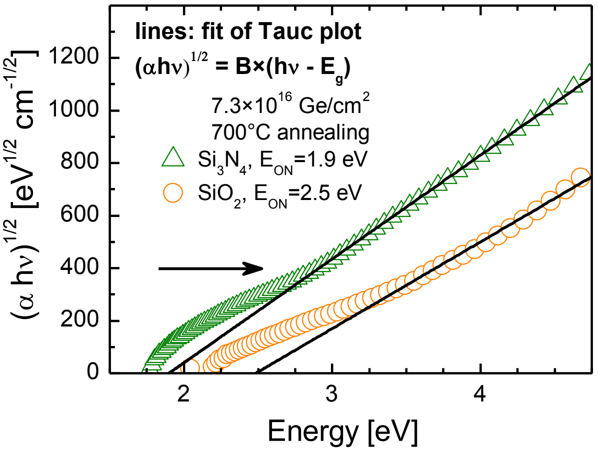

**Figure 3.18:** Tauc plot for Ge QDs in $Si_3N_4$ (triangles) or in $SiO_2$ (circles) and corresponding linear fit (defects induced absorption, below the arrow, causes deviation from the fit). Figure adapted from ref. [97].

Thus, a clear role of the hosting matrix emerges for what concerns the optical bandgap of Ge QDs. In this regard, it is important to know if the same results also hold when the QDs size is varied by changing the Ge concentration. For this reason, in the next paragraph we will compare the structural and optical properties of Ge QDs embedded in $Si_3N_4$ and $SiO_2$ synthesised by PECVD and ion implantation techniques. This further investigation is needed to discern the role of Ge content and QD size in the synthesis and optical absorption of these systems.

### 3.4.2 Ge QDs by PECVD: similarities and differences with the implanted case

With the same conditions described for the SiGeO films reported in section 3.2.2, thin SiGeN films have been deposited by PECVD on fused silica quartz or Si substrates kept at 250°C and then annealed at 800°C (1h, $N_2$ atmosphere) to induce the QD nucleation. The concentration of Ge within the SiGeN alloy was varied between 17% (corresponding to ~$1.1\times10^{22}$ at/cm$^3$) to 27% (corresponding to ~$1.9\times10^{18}$ at/cm$^3$) by varying the flux of $GeH_4$ while keeping constant the fluxes of $SiH_4$ and $NH_3$ precursors. Oxygen contaminations (<10%) are present in SiGeN films after annealing, probably due to absorption through the atmosphere.

As observed in the insets of figure 3.19, a very different QD size distribution and packaging is present in the two matrices. As mentioned before, thermal annealing of SiGeO films produces a sparse array of Ge QDs with a size increasing from around 3.5 – to 8 nm with increasing the Ge concentration. On the contrary, despite of the almost twice concentration of Ge in SiGeN films, in this case the annealing produces a packed array of QDs with a mean size slightly increasing with the Ge concentration in the 1 – to 2 nm range. In this case, a QD concentration of the order of 0.5 – 1 $\times10^{20}$ QD/cm$^3$ is found, corresponding to a mean surface-to-surface distance below 1 nm, roughly independent on the Ge content. Actually, the larger QD density and the limited growth of QD size in SiGeN films is similar to what observed for $Si_3N_4$ films implanted with Ge. This confirms the mechanism of reduced Ge diffusivity and larger interfacial energy for QDs nucleation also in SiGeN films grown by PECVD and allow for a more consistent comparison between the two techniques.

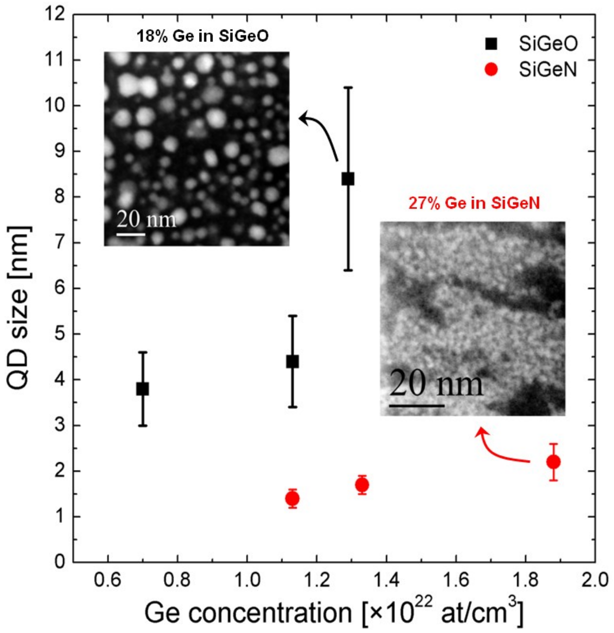

**Figure 3.19:** Evolution of QDs size as a function of Ge concentration in SiGeO and SiGeN films deposited by PECVD and annealed at 800°C.

Once the formation and growth of Ge QDs in SiGeO and SiGeN films have been investigated, the optical absorption properties were compared to disentangle the role of size and matrix on the photon absorption mechanism. In figure 3.20 the absorption cross sections of Ge QDs with only slightly different size embedded in the two matrices are compared. Tough the initial concentration of Ge atoms in the two alloys is different (27% in SiGeN against 8% in SiGeO), the definition of $\sigma$ allows to suitable compare samples with different amount of absorbing centers.

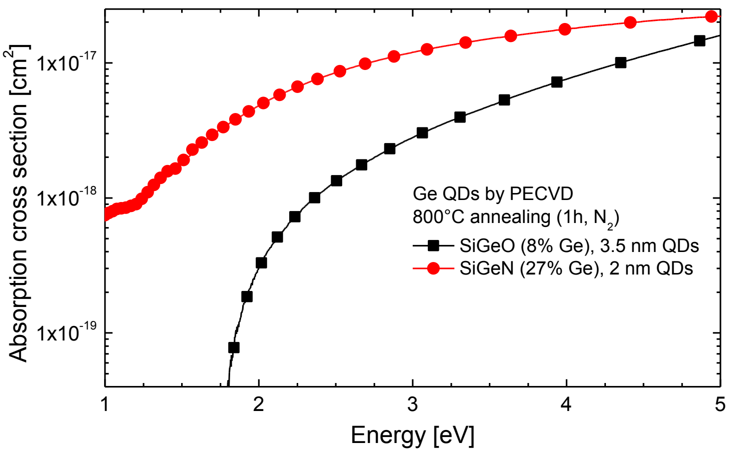

**Figure 3.20:** Absorption cross section spectra of Ge QDs synthesized by 800 °C annealing of SiGeO and SiGeN alloy deposited by PECVD.

As clearly shown in the figure 3.20, QDs nucleated from SiGeN film evidence a larger absorption cross section than SiGeO film (almost 1 order of magnitude at 2.5 eV), with an absorption onset largely red-shifted towards lower energy despite the smaller QDs size. This behavior, similar to that observed in QD synthesized by Ge implantation in $SiO_2$ and $SI_3N_4$, further evidences the strong role of the embedding matrix in the light absorption process.

### 3.4.3 $SiO_2$ vs $Si_3N_4$ matrix

Symbols in figure 3.21 summarize the values of the optical bandgap of Ge QDs for the two matrices as a function of the QD size for both PECVD and implantation techniques. In both nitrides and oxides based matrices, the energy gap $E_g$ exhibits a clear size-dependent shift. As previously discussed, Ge QDs in $SiO_2$ by PECVD (solid squares) display a blue-shift of about 1 eV by shrinking the QD size down to 3-4 nm, fully in agreement with QCE theory. Such an agreement is found also for QDs synthesized by Ge implantation in $SiO_2$, as shown by the symbol (solid triangle) in figure 3.20. A clear blue-shift of $E_g$ occurs also for Ge QDs in $Si_3N_4$ by PECVD (open squares). In this case $E_g$ increases from about 0.9 eV (close to the $E_g$ value of unconfined Ge, ~0.8 eV [85]) for ~2-3 nm QDs, to a value of about 1.5 eV for slightly smaller QDs of 1-2 nm of diameter.

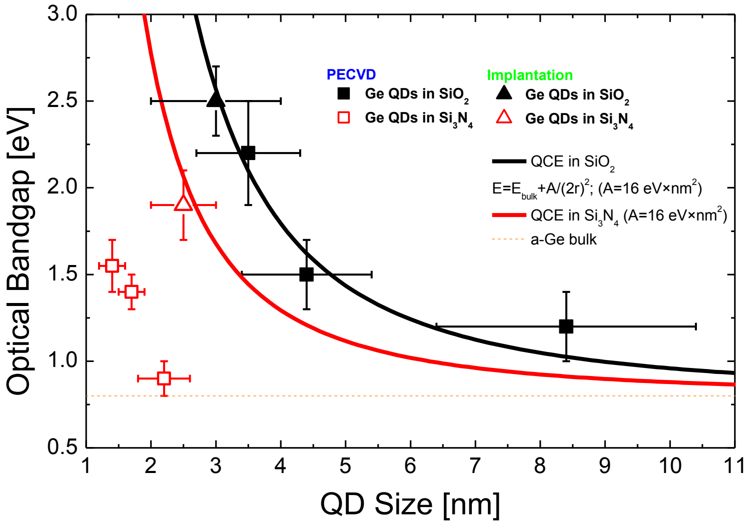

**Figure 3.21:** Optical bandgap of Ge QDs in $SiO_2$ and $Si_3N_4$ matrix as a function of QD size and the synthesis technique used. The solid back line was obtained through fitting from the effective mass theory relationship (infinite barrier case) of experimental data for Ge QDs in $SiO_2$ synthesized by PECVD. Solid red line represents the theoretical bandgap for QDs embedded in $Si_3N_4$ (finite barrier case). Small dashed line represents the optical bandgap of unconfined a-Ge.

However, even if the optical behaviour of Ge QDs hosted in $SiO_2$ is well described by quantum confinement theory, large discrepancies occurs when they are embedded in $Si_3N_4$, depending on the synthesis technique used. This is particularly evident for the optical bandgap exhibited by ~2-3 nm QDs synthesized by ion implantation in $Si_3N_4$ ($E_g$~2 eV, open triangle), which is much larger than that of QDs with similar size synthesized by PECVD ($E_g$~0.9 eV open square). To explain such a large difference and better discern the role of the size from the matrix, we should consider the barrier heights seen by electrons and holes for Ge QDs embedded in the two different matrices. As drawn in figure 3.22, the offsets between conduction and valence band edges can be computed relating their position to the vacuum level and using, at a first order approximation, the electron affinities (χ) and bandgap of bulk materials (as reported in the table of figure 3.22 [122][123]).

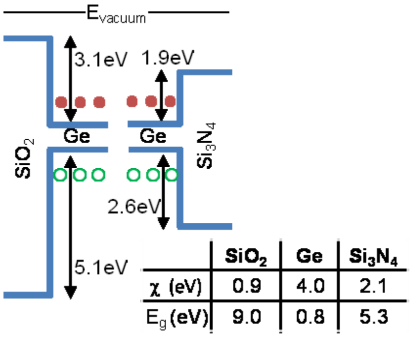

| | $SiO_2$ | Ge | $Si_3N_4$ |
|---|---|---|---|
| χ (eV) | 0.9 | 4.0 | 2.1 |
| $E_g$ (eV) | 9.0 | 0.8 | 5.3 |

**Figure 3.22:** Schematic of band alignment for Ge QDs in $SiO_2$ or in $Si_3N_4$, with relative electron affinity (χ) and bandgap ($E_g$). Adapted from ref. [97].

By taking into account Eq. (1.4) and assuming an infinite barrier for carriers in the case of $SiO_2$ matrix, we get $E_g \sim 2.6\,eV$ for 3 nm sized Ge QDs in $SiO_2$ (using the value of the confinement parameter $A$=16 eV×nm$^2$ determined in section 3.2.2), in agreement also with our experimental results for ion implanted sample. On the other hand, $Si_3N_4$ matrix offers a lower barrier to carriers (sum of offsets $V_0$~ 4.5 eV), so that a finite barrier calculation is needed because the bandgap widening is reduced by the factor $\left[1+\frac{\hbar}{r\sqrt{2m^*V_0}}\right]^2$ [27]. As shown by the red curve in figure 3.21, this factor lowers the expected $E_g$ of 2-3 nm Ge QDs in $Si_3N_4$ to around 2 eV, in good agreement with the experimental result obtained for QDs produced by ion implantation.

On the contrary, the strong discrepancies occurring for QDs in $Si_3N_4$ synthesized by PECVD demonstrates that other competitive effects take place in the absorption process in this last case. Most likely, the presence of mid-gap states due to the incomplete phase separation of SiGeN films and also the not negligible oxygen contaminations after thermal annealing at 800 °C can account for such a large deviation from quantum confinement regime. Thus, besides the role of size and height of confining barrier in controlling the optical behavior of Ge QDs, a strong role is determined also by the quality of the hosting matrix and by the amount of defects states, which can even dominate over the effects of quantum confinement.

## 3.5 Conclusions

In this chapter we presented a detailed experimental investigation on the synthesis, structural analysis and optical absorption properties of Ge QDs embedded in insulating matrix. In particular, we studied the role of the structural parameters (such as QD size and density, structural phase, QD-QD spacing, hosting matrix, amount of defects, synthesis technique) on the optical behavior of these systems. Ge QDs in $SiO_2$ have been synthesized through thermal annealing of SiGeO films deposited by sputtering or PECVD techniques or by annealing of stoichiometric $SiO_2$ films implanted with Ge. Ge QDs in $Si_3N_4$ have been synthesized through thermal annealing of SiGeN films deposited by PECVD or stoichiometric $Si_3N_4$ films implanted with Ge. In general, Ge QDs in $Si_3N_4$ tend to remain amorphous, and are much smaller and closer to each other than in $SiO_2$ matrix, because of the larger interfacial energy and reduced diffusivity of Ge in $Si_3N_4$.

Effects due to quantum confinement of carriers in Ge QDs have been observed in all the investigated experiments. However, the optical behavior of QDs appears to be quite complex, and not always can be fully described only by size effects. Some distinctions have to be made regarding the different contributions arising by their structural properties. Figure 3.23 summarizes the optical bandgap of Ge QDs in $SiO_2$ and $Si_3N_4$ matrix as a function of QD size and the synthesis technique used.

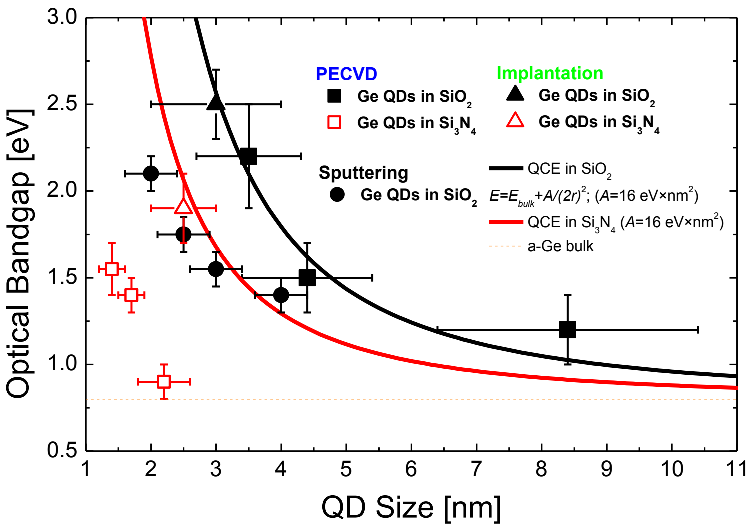

**Figure 3.23:** Summary of the optical bandgap of Ge QDs in $SiO_2$ and $Si_3N_4$ matrix as a function of QD size and the synthesis technique used. QDs in $SiO_2$ have been synthesized through annealing of SiGeO films deposited by sputtering (solid black circles), PECVD (solid black squares), or $SiO_2$ films implanted with Ge (black solid triangle). QDs in $Si_3N_4$ matrix have been synthesized through annealing of SiGeN films deposited by PECVD (open red squares) or $Si_3N_4$ films implanted with Ge (open red triangle). Solid black line represents the theoretical trend of the optical bandgap for Ge QDs in $SiO_2$, obtained through fitting from the effective mass theory relationship (infinite barrier case) of experimental data. Solid red line represents the theoretical bandgap for QDs embedded in $Si_3N_4$ (finite barrier case). The optical bandgap of unconfined a-Ge is reported as small dashed line for comparison.

From the data reported in Figure 3.23 and the results discussed along this chapter, the following conclusion can be drawn:

- Nearly isolated Ge QDs in $SiO_2$ produced by PECVD or ion implantation (respectively solid black squares and triangle in figure 3.21) behave as an ideal-like three-dimensionally confined system in which the bandgap and the optical oscillator strength exhibits a clear tuning with the QD size, in agreement with the QCE predictions. In particular, by fitting our experimental values of $E_g$ within the effective mass theory, we estimated a value of the confinement parameter $A$=16±2 eV×nm$^2$. Such a value is about 3 times larger than the $A$ value obtained for the single a-Ge QW ($A$=4.35 eV×nm$^2$) case, in agreement with the theoretical predictions when passing from a 2D to a 0D confined structures. Such evidences support the predominant role of quantum confinement in describing the optical behavior of a nearly isolated array of Ge QDs embedded in an infinite barrier matrix.

- The type and stoichiometric quality of the hosting matrix deeply affects the optical properties of Ge QDs. When hosted in a stoichiometric $Si_3N_4$ matrix (open red triangle in figure 3.23), Ge QDs evidence an optical bandgap lowered by the reduced barrier height of $Si_3N_4$, but still in good agreement with the value expected from QCE. On the other hand, a poor quality of the hosting matrix (due to an incomplete phase separation of the Ge-rich dielectric film or to a large amount of defects), cause deviations from quantum confinement regime. Such behavior explains the systematically lower values of the optical bandgap observed for small QDs synthesized after thermal annealing of SiGeN films by PECVD (open red squared in figure 3.23) or SiGeO films by sputtering (close black circles in figure 3.23) with respect to the values expected from only QCE.

- QD packaging and inter-dot distance have also a strong role on the strength of the optical absorption of these systems. 3D-randomly distributed arrays of QDs having a fixed QD-QD spacing (~2 nm) show a roughly constant oscillator strength, which does not change with varying the QD size as one should expect from QCE. To further deepen this point, we studied the photon absorption in multi-layers of vertically ordered Ge QDs (with a fixed size of ~3 nm) spaced by $SiO_2$ barriers with thickness in the 3-20 nm range. In this case, the different QD-QD vertical spacing significantly changes the effectiveness of the light absorption, since a closer packaging allows a clear enhancement in the photon absorption. These findings demonstrate how the optical response of an ensemble of QDs can be affected by proximity effects between adjacent QDs (such as dipole interactions, energy transfer, strain induced effects) that significantly modify the strength of the optical absorption, even dominating the effects due to the confinement.

These results clearly demonstrate that the optical properties of Ge QDs are strongly influenced by several effects, not uniquely related to the confined dimension of these systems and that can dominate over the simply quantum confinement. However, by a precise control of the structural parameters of QDs is still possible to effectively tune the optical response of these system and exploit their properties for light harvesting applications.

# Chapter 4

# Light detection with Ge nanostructures

*In this chapter we will investigate the conduction properties and the efficiency of photo-carrier extraction of light harvesting devices based on Ge nanostructures. In particular, we will report on the spectral response of metal-insulating-semiconductor (MIS) devices employing single amorphous Ge QW or packed arrays of small (2 to 4 nm) Ge QDs in* $SiO_2$ *as light sensitizer and conductive layer. Devices with Ge QWs exhibit a clear enhancement of the photocurrent with the QW thickness, indicating a key role of Ge in the electron-hole photo-generation process.*

*When Ge QDs are used as active materials in MIS photodetectors, much larger performances are achieved, due to a mechanism of photoconductive gain activated by QDs. We will investigate the role of Ge QDs size and QD-layer thickness on the response of these photodetectors and explain the photoconductive gain observed as a result of a preferential trapping mechanism of photo-generated holes in Ge QDs. These results clearly demonstrate the large applicability of Ge QDs for the fabrication of high-efficiency and fast Si-compatible photodetectors and the potential application for future low-cost solar cells.*

## 4.1 From material to device

In the previous chapters we dealt about the optical absorption of Ge NS and on the role played by their size, order distribution and matrix effects in modifying the absorption capability of these confined systems with respect to the bulk material. The absorption coefficient of a material is one of the most important key factors in determining the performance of any kind of device operating under illumination (as solar cells or photodetectors). Of course, as larger the absorption coefficient of a material is, as thinner absorbing layer is needed. Figure 4.1 compares the absorption coefficient of bulk Si and Ge with the absorption coefficient measured for 3 nm Ge QDs in $SiO_2$ synthesized by PECVD (chapter 3.2.2). To generate an adequate number of photo-carriers in a light-harvesting device a $\mu m$-thick layer of bulk Si is typically needed in the visible spectral range. The thickness of the absorbing layer can be reduced to a few tens - hundreds of nm using bulk Ge, extending also the operation region of the device in the NIR. However, this approach determines higher production costs, due to the scarsity of this element. Indeed, the absorption coefficient of Ge QDs behaves in the between bulk Si and Ge. As shown in figure 4.1, Ge QDs have a lower absorption coefficient than bulk Ge, due to their larger bandgap and the much less amount of absorbing material employed. However, they evidence an absorption still larger than bulk Si, especially in the VIS-NIR spectral region. In addition, the absorption coefficient of QD thin films posses the great advantage to be highly tunable, in energy and absorption efficiency, with the QD size, QD-QD distance and type hosting matrix. These properties gives the great chance to tailor the thickness of the absorbing layer and selectively tune the operative spectral range of light harvesting devices employing Ge NS.

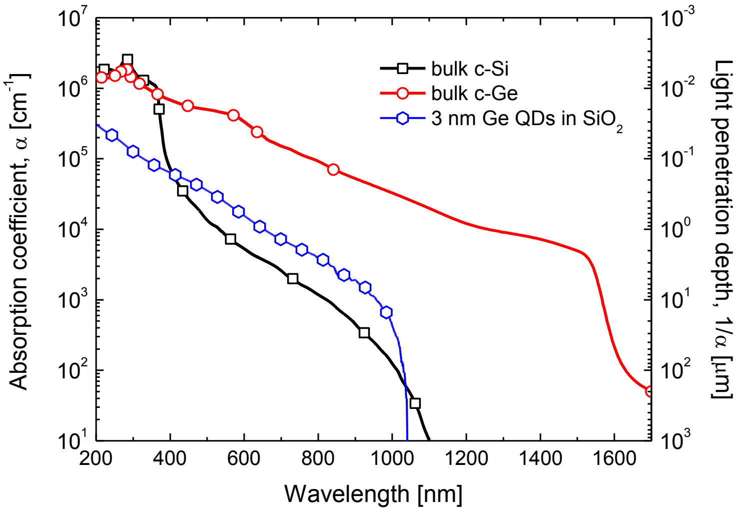

**Figure 4.1:** Comparison between the absorption coefficients (left vertical scale) and light penetration depth (right vertical scale) of bulk crystalline Silicon, Germanium [5] and 3 nm Ge QDs embedded in $SiO_2$.

The other key factor in the performance of any light harvesting device is the capability to extract the photo-carriers generated through light absorption. Depending on the band structure of the device, such photo-carriers can be separated by the action of a built-in electric or by the direct application of an external electric field. The first case is typically exploited in solar cells (*p*-*n* junction or Schottky diode) or in analogous photodiodes operating in photovoltaic mode, while in the second case the device works as a photodetector. Of course, the mechanism of conduction and photocarrier extraction in devices employing Ge NS has a primary importance toward their usage as active material in light harvesting devices.

For this reason, a fundamental step in this direction is to firstly study the carrier transport mechanism in Ge NS thin films under light conditions and investigate the effectiveness of photo-carrier extraction under applied external bias. Therefore, in the following paragraphs, we will give a detailed investigation on the mechanism of photo-carrier conduction and extraction mechanism in prototypal light detectors employing Ge NS as absorber/conduction active medium.

## 4.2 The simplest approach: Light detection by single Ge QW

On chapter 2 we described the optical properties of single a-Ge QW. We demonstrated that these structures behave as a quasi-ideal system in term of the confinement effect of carriers. Such structures revealed a large size-dependent tuning of their optical bandgap and a significant increase in the light absorption efficiency due to an enhanced optical oscillator strength. The chance to exploit such effects is fundamental toward the development of high-performances and energy-tunable light harvesters.

In order to test if photo-generated carriers in a-Ge QWs can be separated and collected through the action of an external electric field, we fabricated a photodetector device, as illustrated in the drawing of Figure 4.2. A metal-insulator-semiconductor (MIS) configuration was pursued after sputter deposition at room temperature of a transparent gate electrode (Al-doped ZnO, 3×3 $mm^2$ area) onto the $SiO_2$/Ge/$SiO_2$ structure grown upon (100) *n*-Si substrate (40 – 120 Ω·cm). Finally, silver paint was used to assure the electrical back contact. Transversal current density versus voltage (*J*-*V*) measurements in dark and under white light illumination were performed in the 400- to 1100-nm range ( photon flux in the range of $10^{13}$ to $10^{14}$ photons/($cm^2$·s)) using a Keithley 4200 semiconductor characterization system.

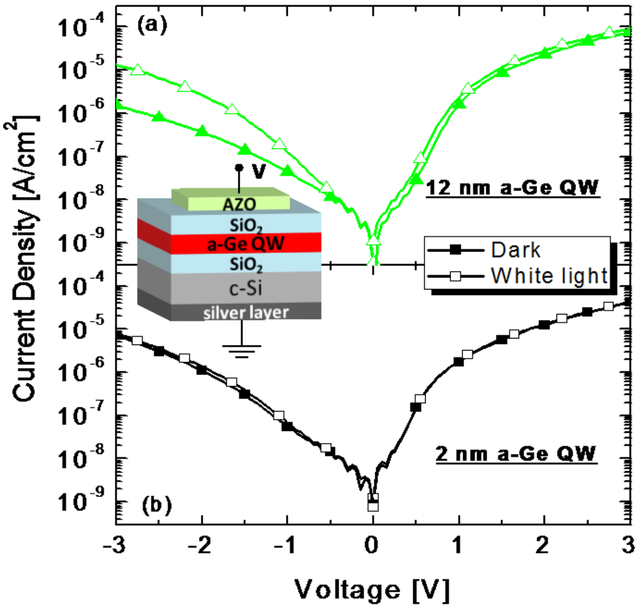

**Figure 4.2:** Current density versus voltage (*J*-*V*) measurements under dark (filled symbols) or white light (empty symbols) conditions, in devices containing (a) 12- or (b) 2-nm a-Ge QWs. The used metal-insulator-semiconductor configuration is drawn in the figure. Figure from ref. [83].

Figure 4.2 reports the *J*-*V* curves for selected samples with 12 -nm (Figure 4.2a) or 2- nm (Figure 4.2b) a-Ge QW. Under dark conditions, both the MIS devices (biased as shown in the drawing) have similar behavior in forward and reverse biases. Most of the applied voltage is dropped across the dielectric ($SiO_2$) stacks, while the QW thickness slightly lowers the dark current density ($J_{dark}$) in the thicker sample (offering a more resistive path). Upon white light illumination, the *J*-*V* values remains largely unaffected in the forward bias, while an increase of the current density ($J_{light}$) occurs for the thicker samples in the reverse bias regime. In particular, for a negative bias of −3 V, the net photocurrent ($J_{light} - J_{dark}$) increases from 1 to 12 $\mu A/cm^2$ going from 2 to 12 nm of QW thickness. The net photocurrent is due to the electron-hole pairs photo-generated in the QW and in the substrate (n-Si). As the device is reverse biased, electrons are pushed to the substrate and holes to the transparent electrode. It should be noted that, by increasing the Ge QW thickness, the contribution of the substrate to the net photocurrent shrinks. In fact, the photo-generation of electron-hole pairs in the substrate decreases because of the light absorbed in the QW, and the carrier collection lowers because of the higher resistance. By comparing the images in Figure 4.2 (a), and (b,) we can appreciate the role of the a-Ge film, as the MIS devices differ only for the QW thickness. The higher net photocurrent measured in the thicker QW gives a clear evidence of a positive photoconductivity effect within a-Ge QWs.

In order to quantitatively investigate the spectral response of the devices, we illuminated them with different wavelengths and measured the external quantum efficiency ( $\mathrm{EQE} = \frac{hc}{\lambda}\left(J_{\mathrm{light}} - J_{\mathrm{dark}}\right)/P,$ where $P$ is the power of incident photons per unit area), which gives the number of collected carriers per incident photon at a given wavelength. In Figure 4.3 (a,) the EQE spectra are reported for both the devices biased at −3 V. The device with 2-nm a-Ge, shows a fairly low and flat photo-response in all the investigated spectral range. Such a response was expected after the very low net photocurrent reported in Figure 4.2(b). Actually, this behavior is mainly attributed to the contribution of the carrier generation and extraction within the depleted region layer in the Si substrate, without a significant role of the Ge QW. In fact, as shown in figure 2.10 of chapter 2, light absorption by the 2- nm a-Ge QW occurs only for photons with energy larger than 1.8 eV (λ ≤ 700 nm). Moreover, even for λ ≤ 700 nm, the fraction of photons absorbed by 2 nm Ge QW is only a few percent of the total incident one. Thus, a really small contribution of the 2-nm a-Ge QW is expected on the overall response of the photodetector, allowing for the consideration of the 2- nm a-Ge QW device response as a reference for the substrate behavior. On the contrary, the device with 12- nm a-Ge QWs shows a much larger EQE, clearly indicating the paramount role of carriers photo-generation within a-Ge films. Even if the maximum EQE is only 14%, one should consider that the photoresponse in this device is mainly attributable to the photo-carrier generation within the 12- nm Ge layer and their following extraction, since the Si substrate has only a minor contribution in this case. In particular, from the measurements of the absorption coefficient reported in chapter 2, it is possible to estimate that the fraction of absorbed light in the 12- nm-thick a-Ge QW is much lower than unity in the entire spectral range investigated.

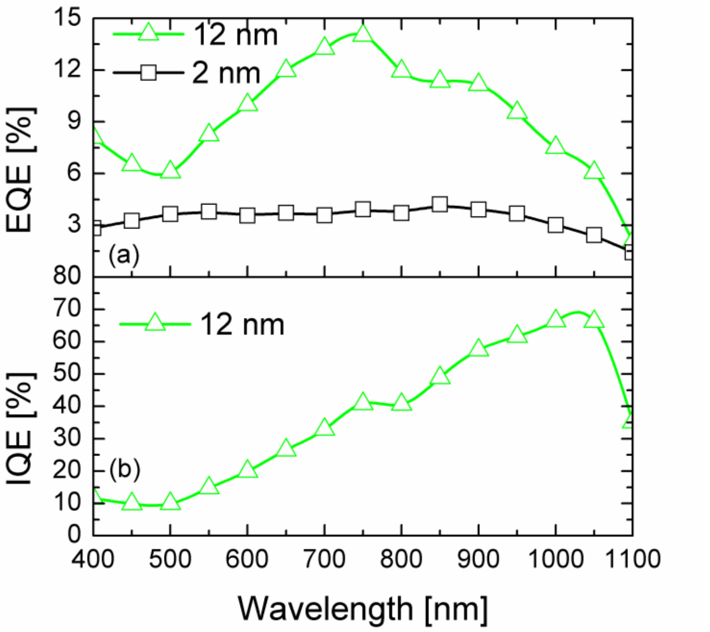

**Figure 4.3:** (a) EQE spectra taken at −3V bias for the 2- or 12-nm a-Ge QW devices. (b) IQE spectrum for the 12-nm a-Ge QW photodetector biased at −3 V. From ref. [83].

Therefore, by measuring the fraction of light absorbed within the QW, we can extract the internal quantum efficiency (IQE). Such a quantity gives the number of collected carriers per absorbed photon at a given wavelength by the Ge layer: $\mathrm{IQE} = \frac{hc}{\lambda}\left(J_{\mathrm{light}} - J_{\mathrm{dark}}\right) \Big/ \left[P\left(1-e^{-\alpha \cdot d}\right)\right]$. As reported in Figure 4.3(b), the IQE shows values as high as 70% in the near-infrared region, close to the $E_g$ value (~approximately 0.9 eV) that we measured for this system by absorption spectroscopy. This correlation further supports the main role of the a-Ge QW as active absorbing layer in the photodetector device. The IQE spectrum decreases for higher photon energy as the collection of the hotter carriers is less probable, due to recombination issues.

The high IQE value indicates that a large part of the photocarriers generated by light absorption in Ge QW are effectively extracted through an applied bias. Hence, the high IQE measured on this device reveals that a-Ge QWs can be profitably used as efficient photo-sensitizer in light detection devices. In addition, the excitonic effect and the bandgap tuning due to the quantum confinement effect can be further exploited to develop energy tunable and efficient photodetectors operable at room temperature, which are compatible with Si technology and with low- cost approach.

## 4.3 High efficiency photodetectors based on Ge QDs

As shown in the previous paragraph, good performances can be achieved by using Ge QW as active medium in photodetectors devices. In theory, the usage of Ge QDs could potentially improve the performances of light harvesting devices, because of the easier bandgap tuning and a stronger optical oscillator strength with respect to QW due to quantum confinement. However, we have demonstrated that the optical properties of these systems cannot be explained solely with QCE. In fact, the amount of defects, the type and quality of the matrix or even the QD packaging strongly concur in determining the optical response of these systems. In a similar way, these parameters can strongly influence the electrical response and conduction mechanism in QD based photodetectors.

Actually, despite much research have been performed into the investigation of the structural and optical properties of Ge QDs, only a few studies have addressed photodetector (PD) devices based on these materials. Only recently, detection amplification in the UV-VIS range through the usage of Si and Ge QDs have stimulated increased interest as viable materials for high responsivity photodetectors (PDs) in the visible and near infrared wavelength ranges. For example, Si QD PDs have been shown to achieve peak responsivities in the range of 0.4–2.8 A/W [51][52], and optoelectronic conversion efficiencies as high as 200% due to photoconductive internal gain mechanism. Compared to Si QDs, $SiO_2$-encapsulated Ge QDs are characterized by lower synthesis temperatures, as well as higher absorption coefficient. However, so far the maximum performances reported for Ge QD PDs has been 0.13 A/W at 820 nm [49] and 1.8 A/W at 600 nm, with the latter devices produced via a high-temperature anneal at 900 °C [53] and slow response time in the *ms* range [54].

One open question concerning the use of Ge nanostructures in the fabrication of high-efficiency and fast PDs is whether the structural and absorption properties of such nanostructures can influence the photo-conversion efficiency of the device. To deepen this point we fabricated MIS PD with high density of a-Ge QDs embedded in the insulating $SiO_2$ layer.

In particular, Ge-rich $SiO_2$ films (~250 nm thickness, 16% Ge) were fabricated by rf-magnetron co-sputtering deposition of a $SiO_2$ and a Ge target onto a (100) $n^-$ Si substrate (40 – 120 Ω·cm), as described in section 3.2.1 of chapter 3. The temperature during the deposition process (400°C) allow the nucleation of small, densely and homogeneously distributed a-Ge QDs in the as-grown film, with a mean QD size of 2-3 nm and a QD-QD spacing of the order of 1-2 nm. The top contact of the MIS structure was fabricated by sputter-depositing a fully transparent 55 nm thick indium-zinc-oxide (IZO) film of $2x10^{-4}$ Ω-cm resistivity, whereas silver paste was used to ensure the bottom contact with the n-Si substrate.

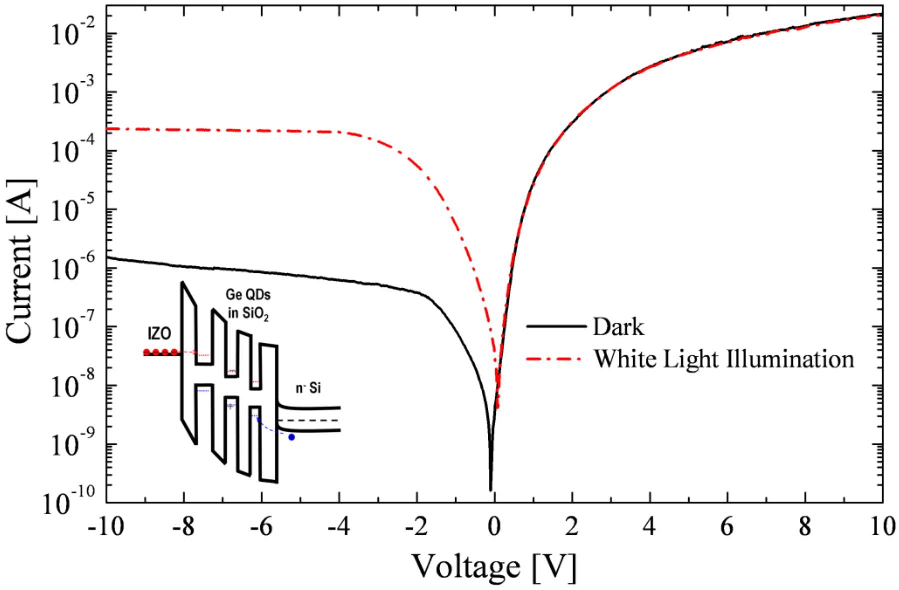

**Figure 4.4:** Current-voltage *I*(*V)* characteristics in dark and under white light illumination of MIS PD with Ge QDs embedded in a silicon dioxide layer. Figure adapted from ref. [55].

Figure 4.4 shows a comparison of the current-voltage *I(V)* curves in the dark and under white light illumination, with the n-Si substrate grounded and the top contact swept from –10 to 10 V in 10 mV steps. In the dark, the I(V) is strongly rectifying, with ~$10^4$ rectification ratio at ±4 V. Similar *I(V)* characteristics were reported previously in MIS structures containing Si and Ge QDs and attributed to hopping conduction through the QDs in the barrier. Within this framework, the large current in forward bias is carried by electrons tunneling from the accumulation layer in the n-Si substrate (where their density increases rapidly with *V* and reduces the effective tunneling barrier). Instead, the low current in reverse bias is due to electrons tunneling from the IZO through a QD-$SiO_2$ network. Tunneling of minority holes from the $n^-$ Si substrate is negligible because of the heavier effective hole mass and the larger valence band offset at the Ge/$SiO_2$ interface that lowers the tunneling probability exponentially [124] [125].

In addition, we can distinguish two different regimes of the photocurrent with respect to the applied bias. For $-2 < V < 0$ the photocurrent exhibits a strong bias dependence, while for larger values of the applied bias the photocurrent saturates. This behavior can be explained by a non-uniform electric field distribution across the QD layer and it is typical in superlattice-based devices [126][127]. For low values of the applied bias, we can consider the electric field $E$ mostly uniformly distributed across the Ge QDs layer and the current increases with bias because of the increasing of electron tunneling probability between QDs. For higher (negative) values of $V$ a nonlinear distribution of the $E$-field takes place due to the preferential charging of QDs close the Si interface by hole-trapping, as drawn in the inset of figure 4.4. This effect leads to the formation of a high $E$-field domain across the neutral QDs and a low uniform electric field region across the rest of QDs layer because the total applied bias remains constant. Therefore, any further increase of the applied bias will mainly result in an increase of the $E$-field only in the high $E$-field domain region, leading to the saturation of the overall current with respect to the applied bias.

Upon white light illumination, the forward bias *I(V)* remains largely unaffected, but there is a strong increase of the reverse current by a factor of >100, similar to the results reported by Shieh et al. in a Si QD-containing MIS structure [51].

In order to understand the mechanism of the photocurrent, we performed *I(V)* measurements by illuminating the device at various incident λ in the 400–1100 nm range under continuous wave (cw) illumination. The results are shown in Fig. 4.5(a), where we find a clear spectral dependence of the photocurrent, with a peak at around 900 nm that is one order of magnitude larger than the current in dark conditions. More importantly, control devices with the same thickness of the Ge-rich $SiO_2$ layer, but without Ge QDs do not exhibit any photo-response when illuminated, as demonstrated in figure 4.5(b). This finding indicates the key role of the QDs in the photo-conduction mechanism of this type of photodetector.

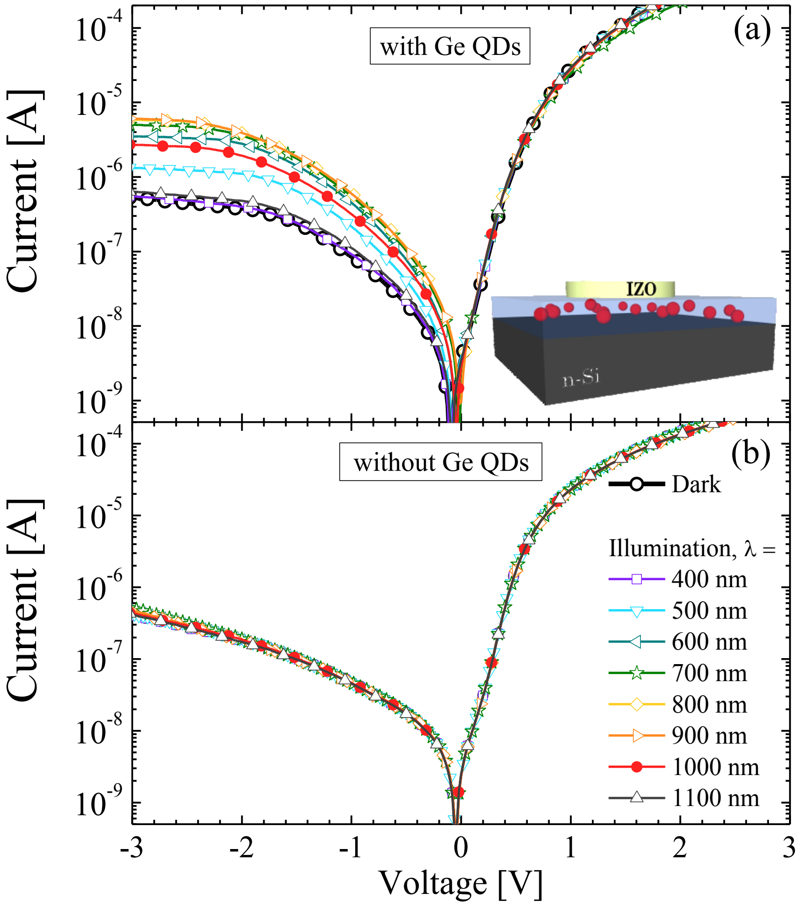

**Figure 4.5:** MIS PD *I*(*V*) characteristics as a function of excitation wavelength λ in the 400–1100 nm range for a device with (a) and without (b) a-Ge QDs. A schematic illustration of the device is reported. Figure adapted from ref. [55].

For a more quantitative analysis of the spectral response and conduction mechanism properties of our PDs, we turn our attention to the spectral responsivity, $R_{sp}$, defined as the photocurrent produced by the device at a given power and wavelength of the incident light:

$$R_{sp}(\lambda)=\frac{(I_{light}-I_{dark})}{P_{ph}(\lambda)} \tag{4.1}$$

where the quantity in the numerator is the net photocurrent under illumination for a given voltage, while $P_{ph}(\lambda)$ is the spectral distribution of the incident photon power, determined using a calibrated Si detector.

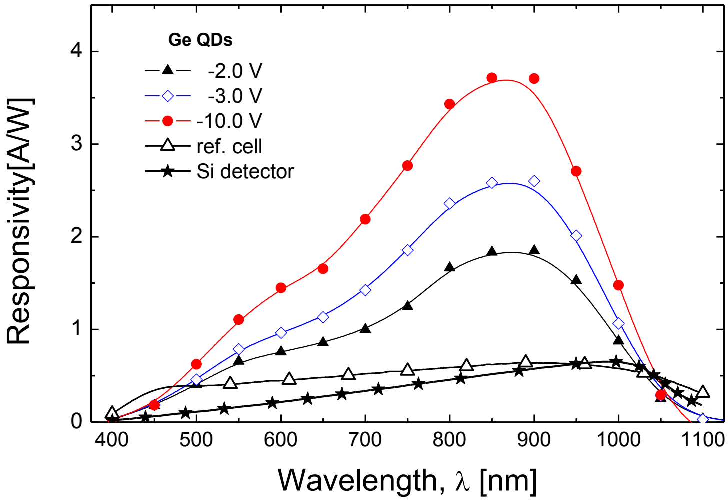

**Figure 4.6:** Spectral responsivity of our MIS PD versus reverse bias. Stars and open triangles indicate, respectively, the responsivity of a commercial Si PD and of an NREL calibrated silicon reference cell. Adapted from ref. [55].

Figure 4.6 shows the responsivity of a device containing a-Ge QDs (~3 nm in size) as a function of λ for several values of the applied bias, obtained by measuring the photogenerated current reported in Fig. 4.5(a). Remarkably, responsivity peaks a value of around 4 A/W at –10 V bias and ~1.75 A/W at a lower –2 V bias in the 800 – 900 nm range. It is worth noting that these responsivity values are higher than the values reported for analogous MIS PDs employing Si or Ge QDs, in particular for low values of the applied bias. In addition, this type of photodetector exhibits also better performances with respect to commercial Si PDs made by p-n diode, as shown in Fig. 4.6 for comparison.

### 4.3.1 Photoconductive Gain Mechanism

To better clarify the role of Ge QDs in the conduction mechanism of this device, it is essential to relate the light absorption within the device to the current behavior during illumination. To this end, we calculated the spectral IQE, defined as the number of carriers collected at the output of the device per each absorbed photon at a given voltage.

$$IQE = \frac{hc}{\lambda} \cdot \frac{\left(I_{light} - I_{dark}\right)}{\left(1 - R\right) \cdot P_{ph}} \tag{4.2}$$

where *R* is the reflectance of our Ge QDs MIS PDs, measured using a calibrated Si standard reference (not shown here).

The results are summarized in figure 4.7, which shows IQE values larger than 100% in a wide spectral range from 500 to 1000 nm. Such large values indicate that a gain mechanism, activated by light absorption and the consequently photo-carrier generation, occurs through the action of Ge QDs. In particular, for an applied bias of -10 V a large photoconductive gain as high as 700% is achieved, that means that as many as 7 carriers are extracted at the output of the device per incident photon absorbed. Moreover our Ge QDs PDs shows a remarkable gain even for a low bias of -2 V, with IQE values as high as 300%.

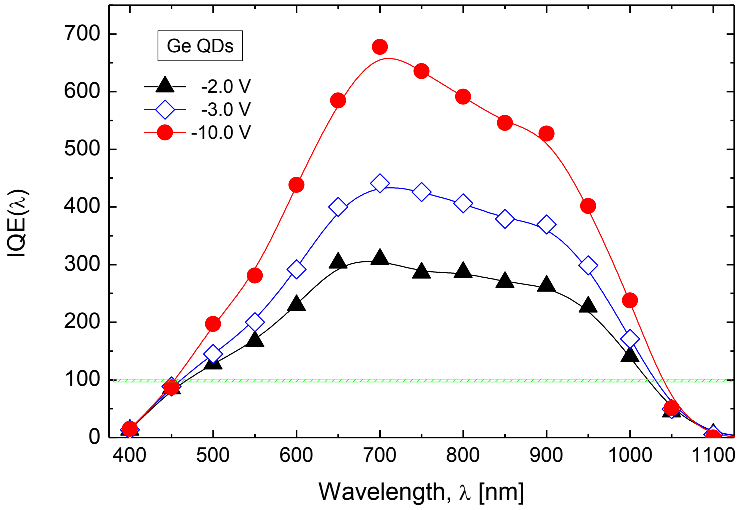

**Figure 4.7:** Spectral IQE of MIS PDs containing Ge QDs in the insulating layer as a function of the applied bias. Adapted from ref. [55].

Typically, avalanche phenomena such as impact ionization require high electron kinetic energies ($E > 3.5\, E_g$) [12]. Thus, we can exclude such a type of phenomenon as the dominant mechanism that explain the gain of our PDs. Instead, we attribute such a large photo-response to a mechanism of hole-trapping activated by the presence of Ge QDs [13, 14]. According to this model, schematically shown in figure 4.8, electron-hole pairs are photo-generated by light absorbed within the Ge QDs layer or the Si substrate. Then, the photo-generated holes get preferentially trapped by the Ge QDs, because of their lower ability to tunnel between QDs into the $SiO_2$ with respect to electrons. The resulting positive charge localized in the Ge QDs layer facilitates the extra injection of electrons from the IZO contact, giving rise to high currents under illumination. According to this mechanism, the high photoconductive gain achieved by Ge QDs MOS PDs is given by the amount of extra electrons injected from the IZO contact gate to the Si substrate in the mean life-time in which the photo-generated hole is trapped within the Ge QDs layer. A similar gain mechanism was previously suggested to explain the photoconductive behavior of MIS structures containing Si QDs in $SiO_2$ [51], as well as GaN/AlGaN metal-semiconductor-metal PDs, where holes are trapped by line defects in GaN [128]. In this regard, defect states around the QD interface could play a similar role in the hole trapping process and for the activation of conduction tunneling paths for extra-electron.

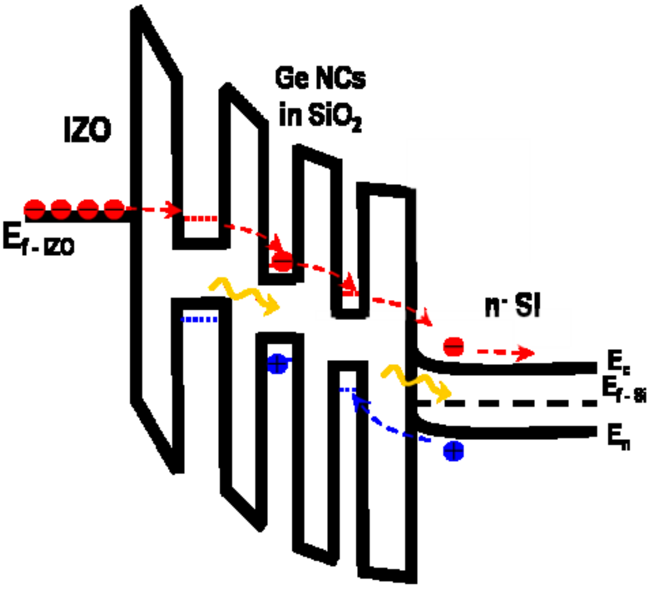

**Figure 4.8:** Schematic representation of the energy band diagram of a MIS PD with Ge QDs and mechanism of conduction under illumination and reverse bias. Adapted from ref. [129].

Actually, the photoresponse of our PDs strongly depends on the electromagnetic wave penetration within the multilayered MIS structure, that is the fraction of light absorbed by the Ge QDs layer or by the Si substrate. In particular, it is important to remind that the optical bandgap of 2-3 nm Ge QDs in $SiO_2$ synthesized by sputtering is around 1.5 - 1.6 eV (λ~800 nm), as shown in section 3.2.1 of chapter 3. Therefore, also the contribution of the Si substrate in the photo-generation of holes is crucial to guarantee the gain mechanism in our PDs, especially for wavelengths where

Ge QDs do not play a significant role in the optical absorption of the incident photons**.** In order to definitively relate the optical properties of our device, we first fit the experimental reflectance spectra for devices with and without IZO layer, by using a multiple reflection model. The fitting procedure (not shown here, see ref. [55]) allowed us to confirm the IZO and QD layer layer thicknesses (55 and 230 nm, respectively) as well as determine the refractive index for the transparent IZO (using a Cauchy model) and volume fraction of a-Ge QDs in the film (~36%, using the Maxwell-Garnett approximation, in good agreement with independent estimates using RBS and TEM analysis).

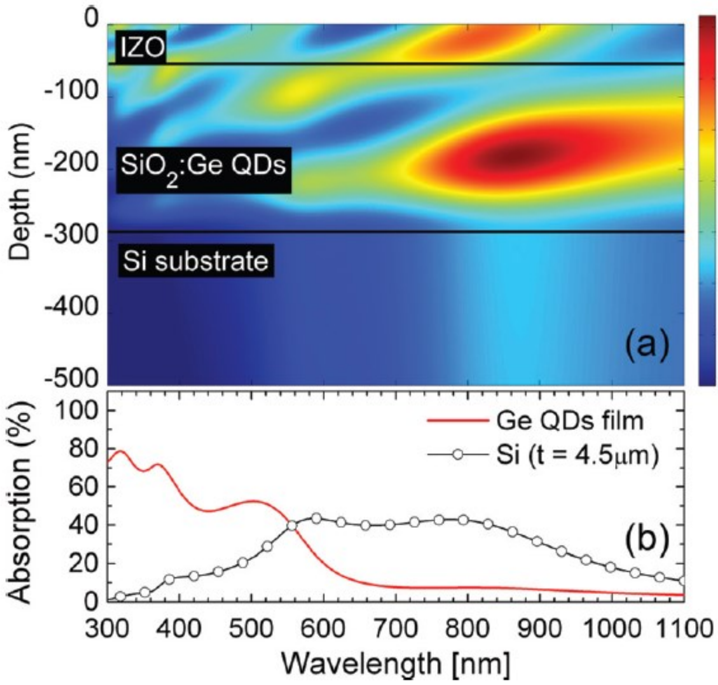

**Figure 4.9:** (a) FDTD calculations of the *E*-field intensity distribution vs. wavelength (300–1100 nm) and depth, normalized by the field intensity of the incident wave. (b) Fraction of incident light intensity absorbed by the Ge QDs (red line) and by the first 4.5 $\mu$m of silicon substrate (corresponding to the minority hole diffusion length). From ref [55].

We then performed Finite-Difference-Time-Domain (FDTD) calculations using a commercial software (Lumerical) to reproduce the reflectance measurements and calculate the electric field intensity distribution inside the PD structure, as shown in Figure 4.9(a), as a function of λ and depth. The electric field intensity (normalized to the incident field intensity) peaks inside the insulating layer containing the Ge QDs, although there is also leakage of incident radiation into the Si substrate in the NIR region. From the simulations and definition of the Poynting vector, we can estimate the fraction of absorbed light intensity occurring within the Ge QDs and the silicon substrate, respectively, as shown in Figure 4.9(b). The results show that while shorter wavelengths (visible region) are absorbed mostly in the Ge QDs layer, longer wavelengths (NIR region) are preferentially absorbed in the bulk Si. Hence, the spectral response of this type of PD is not only related to the direct absorption from Ge QDs strongly, but also a non-negligible contribution of photo-carriers coming from the Si substrate has to be considered. In particular, for $\lambda < 700$ nm the photo-generation of holes is due to the absorption of light both by the Ge QDs and Si substrate (with the QD absorption dominant at smaller wavelengths). Therefore, in the visible spectral region, Ge QDs play two roles: they act as hole-photo-generation (1) and hole-trapping (2) centers. For $\lambda > 700$ nm Ge QDs are mostly transparent to the incident light, which is absorbed only by the Si substrate, as shown in Figure 4.9(b). In this last case, the main role of Ge QDs is to trap photo-generated holes injected from the Si substrate (created within a minority carrier diffusion length from the Si interface) and act as a hopping conduction channel for the electrons injected from the IZO gate contact.

## 4.4 Tuning the optical response: the role of size and defects

The high values of responsivity and the high spectral gain ensured by the presence of Ge QDs demonstrate the great potentiality of the usage of such structures toward the fabrication of high-efficiency PDs. Moreover, our results indicate that the light absorption in both the insulating Ge QDs layer and in the silicon substrate is crucial for achieving a broad and high spectral response. In this regard, it would be important to discern the role of QDs size on the optical response of this type of PDs. This is essential in order to further optimize the performance of these photodetectors and study the potential applicability of Ge QDs also in photovoltaic devices.

For this reason, we fabricated MIS PDs with active layers consisting of Ge QDs having different mean size. In particular, Ge QDs have been synthesized by sputtering deposition (at 400°C) of SiGeO films and after 600°C post-deposition annealing (1h , $N_2$ atmosphere). After fabrication of the active layers, MIS PDs ($3 \times 3$ $mm^2$ active area) were fabricated by sputter deposition of a transparent conductive indium–zinc-oxide (IZO) thin-film top contact and using a silver layer on the back of the n-Si wafer, as described previously.

Table 4.1 summarizes the values of QD layer thickness and mean QDs size, evaluated by TEM analysis, as well as QD concentration (calculated by crossing TEM estimations on QD size and layer thickness with RBS analysis on Ge content). As discussed in sec. 3.2.1 of chapter 3, the shrinking of QD size leads to a blue-shift of the optical bandgap from 1.4 eV for ~4 nm QDs to 2.1 eV for ~2 nm QDs. Such a blue-shift is only partially attributable to the effect of quantum confinement. In fact, we have demonstrated that proximity effects and/or surface-related defects lead to a deviation from QCE regime, as stronger as smaller and closer these QDs are. Moreover, all the investigated MIS PDs have a roughly comparable thickness of the QD layer ($W_{QD}$= 250±40 nm) and a QD-QD distance of around 1-2 nm. Therefore, the variation of the spectral response of our PDs with the QDs size, if any, can be directly linked only to the different effectiveness of the QD layer in the absorption process.

**Table 4.1:** Summary of MIS PDs containing Ge QDs in insulating layer Ge-rich $SiO_2$ layers. QD-layer thickness and QD size have been evaluated by TEM analysis, while QD density by crossing RBS analysis on Ge content and TEM analysis on QD size. QD bandgap have been evaluated by absorption spectroscopy on samples deposited on fused silica substrate, as reported on Chapter 3.

| **Device** | **QD-layer thickness, $W_{QD}$, [nm]** | **QD size [± 1 nm]** | **QD concentration [QD/cm$^3$]** | **QD Bandgap [eV]** |
|---|---|---|---|---|
| PD2 | 210 | 2 | $1.2\times10^{19}$ | 2.1 |
| PD3 | 250 | 3 | $2\times10^{19}$ | 1.6 |
| PD4 | 290 | 4 | $7\times10^{18}$ | 1.4 |

Figure 4.10 shows the spectral IQE for an applied bias of -10V calculated from *I(V)* characteristics of MIS PDs with different size of Ge QDs embedded in the active QD-layer. As clearly shown in the figure, a large photoconductive gain (IQE > 100%, green bar in figure 4.10) is exhibited for all the reported PDs in a broad 500 – 1000 nm spectral range. However, also a large variation of the photoconductive gain occurs when the size of QDs is changed. PDs with the active layer consisting of 3 nm and 4 nm Ge QDs shows an IQE peaked at around 700 nm and markedly increasing from around 300% to almost 700% with the decreasing of the QDs mean size. Such trend is confirmed also for the PD with 2 nm Ge QDs, which shows much larger values of the photoconductive gain in all the investigated range, with an IQE peak blue-shifted at around 500 nm and reaching impressive values as high as 1500%.

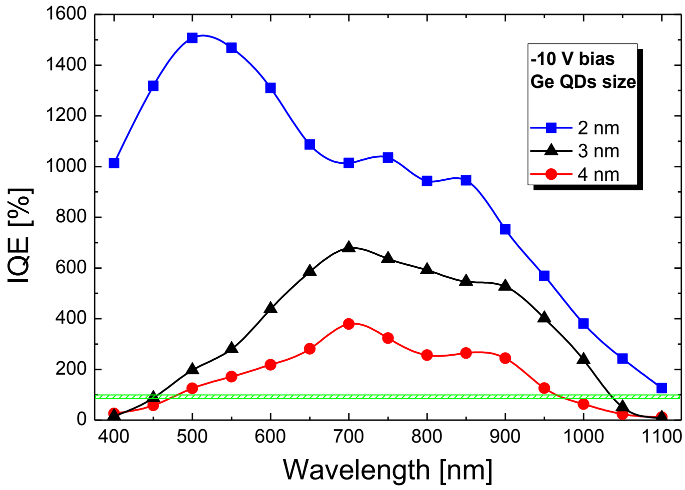

**Figure 4.10:** Spectral IQE at -10V of applied bias for MIS PDs containing Ge QDs of different size in the active QD-layer.

In first approximation, the reason of such a large variation of the IQE can be linked to the different optical bandgap of Ge QDs and their capability to efficiently absorb the incident light. In particular, we can consider the QD-layer as a sort of size-tunable filter for the incident photons that are absorbed by the underlying Si substrate.

To deepen this point we calculated the fraction of light absorbed by the Si substrate lying below the QDs layer for the different QDs sizes. By excluding for simplicity the effects of interference at the ITO/QD-layer and QD-layer/Si interface, we can estimate such a quantity by taking into account the fraction of the incident light firstly absorbed by the QD layer and considering the remaining part that is absorbed within a thickness *l* of 4.5 $\mu$m (minority hole diffusion length in Si) by the underlying Si substrate, in agreement with the relationship:

$$\frac{I_{Si}}{I_0} = \left(1 - e^{\alpha_{QD} \cdot W_{QD}}\right) \cdot e^{-\alpha_{Si} \cdot l} \tag{4.3}$$

where $\alpha_{Si}$ is the absorption coefficient of bulk Si [25], $I_0$ is the incident light intensity while $\alpha_{QD}$ is the absorption coefficient for QD at different sizes (calculated in sec. 3.2.1 of chapter 3) and $W_{QD}$ the thickness of the QD layer.

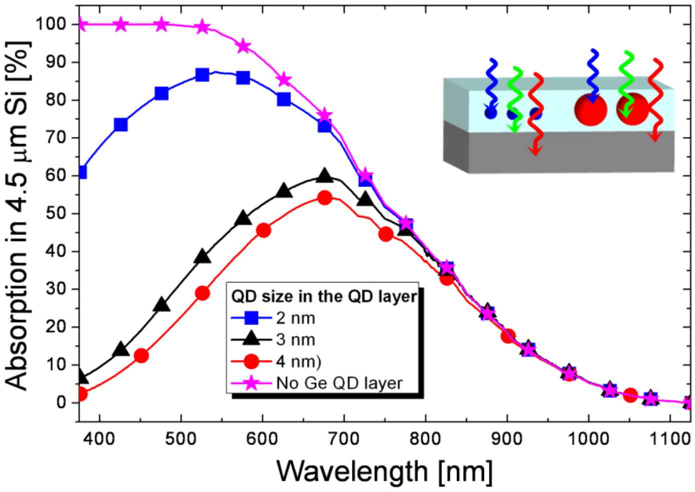

**Figure 4.11:** Spectral distribution of the fraction of light absorbed by 4.5 $\mu$m-thick Si substrate as a function of the size of Ge QDs in the QD-layer.

As shown in figure 4.11, by decreasing the QD size more light is absorbed by the Si substrate. This is basically due to the higher optical bandgap of QDs and the consequently lower absorption capability of the QD-layer. This effect, in turn, leads to a preferential photo-holes generation by the Si substrate and the consequently injection and trapping in the QD-layer. It is worth to note, from a closer comparison of the curves reported in figure 4.10 and 4.11, that the fraction of the light absorbed in the Si substrate is peaked at approximately the same wavelength range where the corresponding QDs MIS PDs show a peak in the photoconductive gain. As more transparent the QD-layer is (figure 4.11), as higher the photoconductive gain is (figure 4.10). Such behavior suggests the idea that electron-hole pairs photo-generated by light absorption within the QD-layer have only a minor contribution in activating the photoconductive gain process, since they probably recombine suddenly within the QD. Anyway, the presence of QDs is fundamental to guarantee the gain mechanism by hole-trapping. In fact, reference devices with no Ge QDs nucleated in the SiGeO layer do not show any response with light illumination, as observed in figure 4.5 (b). This means that the performances of this type of device are strictly related to: (1) the amount of photo-holes generated within the Si substrate and (2) to the effectiveness of hole-trapping by QDs. Therefore, the QD-layer acts as a QD-size tunable optical filter for the response of the device and also as a selective conductive layer for injected carriers.

In this regard, the increasing of the photoconductive gain with the shrinking of QD size can be only partially attributable to the larger amount of photo-holes created within the Si substrate and subsequently injected and trapped in the QD layer. This is particularly evident for wavelengths where QDs are optically transparent. As shown in figure 4.11, at λ = 800 nm almost the same fraction of photons are absorbed by the Si substrate, independently from the size of QDs embedded in the QD-layer. Thus, we should expect a similar IQE for all the different sizes of Ge QDs, since the same amount of photo-holes is generated in the Si substrate. However, as shown in figure 4.10, this is not the case. On the contrary, at 800 nm IQE increases of almost a factor 4 when shrinking the QDs size from 4 nm to 2 nm. Still, the fluence of Ge QDs (given by the product of the QD density and the QD layer thickness) should have a role in the gain mechanism, because of the larger quantity of trapping sites available for injected holes. However, such a quantity is truly similar for the devices with 2 nm and 4 nm QDs, therefore it does not really contribute in the gain enhancement observed.

Actually, such increase of the photoconductive gain can be related to a more efficient trapping capability of photo-holes by small QDs. Such hypothesis finds connection also with the optical behavior evidenced by small Ge QDs. In the previous chapter we demonstrated that the optical properties of Ge QDs by sputtering strongly deviate from a pure quantum confinement regime (see figure 3.23), probably due to modification of energy levels in CB and VB induced by a larger contribution of defects or strain-related effects in small QDs. The same type of defects could have an active role also in the hole-trapping process. In this regard, a larger amount of defects states in very small QDs is beneficial for the electrical activation of the photoconductive gain mechanism in Ge QDs MIS PDs. In fact, as longer is the life-time of hole-retention by QD-defects as more extra-electrons can flow, giving rise to larger gain.

## 4.5 Response time

The performance of photodetectors is measured not only in terms of quantum efficiency (or gain) of carrier collection, but also by the response time τ. Such a quantity is related both to the photo-carrier generation and to the transit time taken to transport them to their respective contacts through the action of an *E*-field (external of or built-in, depending on the type of photodetector). In general, the response time of a photodetector is linked to its gain by the relationship $Gain = t_{life} / \tau$ [5][130]. In this case, $t_{life}$ is the life-time of excess carriers, while $\tau$ can be assumed, in first approximation, equal to the transit time of carriers by drift diffusion ( $\tau = W^2 V / \mu$, where *W* is the width of the active layer, $\mu$ is the mobility of the slower carrier and *V* is the applied potential across the device) [5]. If the life-time exceeds the transit time of the flowing carrier through the device, many charges worth of current may be integrated for each photon absorbed, giving rise to a gain. For our Ge QDs PDs, the life-time of photo-carriers (holes in particular) is prolonged with the aid of QDs traps that enables the flowing of many extra-electrons from the IZO contact. Therefore, investigations on the response time are important not only for direct application in light detection devices, but also because they give us indications on the time scale of hole-trapping and on the transit-time of carriers that are involved in the conduction and gain mechanism of this type of PDs.

To this aim, the transient photoresponse of MIS PDs containing ~3 nm Ge QDs have been investigated by illuminating the device (held at constant reverse bias of -2V) with a modulated diode laser (either by a mechanical chopper or through direct digital modulation of the laser) at λ=670 nm. The laser beam was focused on a ~3mm diameter spot. The photo-current was then measured from an oscilloscope by recording the voltage drop across a resistor in series with the PD. Figure 4.12 shows the time response measurements under a modulated incident light beam at λ =670 nm with an optical modulation frequency of 960 Hz. The measurements were performed for various illumination powers, using a 10 kΩ series resistor.

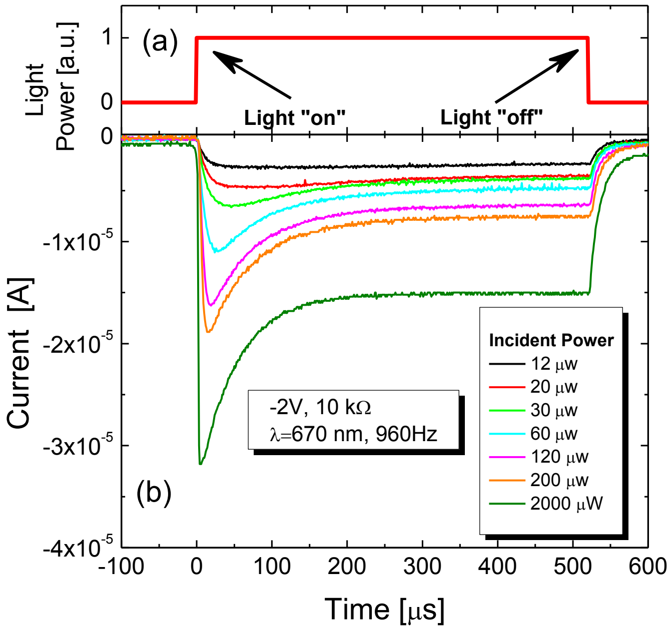

**Figure 4.12:** Transient photoresponse curves for Ge-QD PD with $W_{QD}$=230nm under illumination using a 670 nm laser beam modulated by a mechanical chopper at 960 Hz: (a) representative illumination square waveform; transient photocurrent response under -2V of applied bias (b). The photocurrent signal was obtained by measuring the voltage drop across a load resistor (R=10 kΩ) recorded using an oscilloscope.

A rapid initial rise of the photocurrent magnitude is observed as the light is switched on. Specifically, the photocurrent shows a fast turn-on time ($t_{on}$) overshoot, followed by a slower transient to a steady-state value. The initial photocurrent overshoot level depends on the incident power and can be attributed to a fast photo-absorption, followed by carrier injection and hopping transport of electrons and holes through the QD layer. The slower transient behavior that follows the overshoot suggests that charging in the QDs is followed by an electric field redistribution inside the QD-containing film, similar to the mechanism responsible of the saturation of *I(V)* characteristics in figure 4.4. Indeed, as a result of localized charging of QDs near the interface by hole-trapping, the average field across the remaining QD layer will decrease to ensure that the total applied voltage across the entire film remains constant. As a consequence of the reduced average electric field, a reduced drift current will follow, thus explaining the lower steady state current values after the initial overshoot. A similar photocurrent overshoot was previously reported in a different system, consisting of GaAs/AlGaAs superlattice-based infrared PDs operating at low temperature, and was attributed to charging of the first few quantum wells with subsequent reduction of the electric field in the rest of the superlattice [126][127].

When light is switched off, current approaches to its dark value with a characteristic time, $t_{off}$, intrinsically related to the de-charging of Ge QDs within the QD layer. Rise ($t_{on}$) and decay ($t_{off}$) times of a PD are therefore critical parameters. From our photo-transient current measurements, we can define the switching on (off) time as the time taken by the photocurrent to reach a value of ( $1 - 1/\mathrm{e} \approx 63\%$ ) of its maximum (minimum) after illumination. In figure 4.13 are reported the time-resolved photocurrent curves (normalized to the peak value) at various incident powers of the PD with ~3 nm Ge QDs. We observe a clear power dependence of $t_{on}$ which decreases with increasing incident power, in agreement with a larger number of QDs being electrically activated by trapping of photo-generated holes. In particular, the $t_{on}$ of the PD with ~3 nm Ge QDs goes from ~2 *µs* to around 0.65 *µs* as the incident power is increased from 15 $\mu W$ to 1 $mW$. However, the response time of this type of photodetectors remain considerably slower than the response time of a commercial Si *p-n* fast-photodiode (typically of the order of 50 – 150 ns, continuous line in figure 4.13).

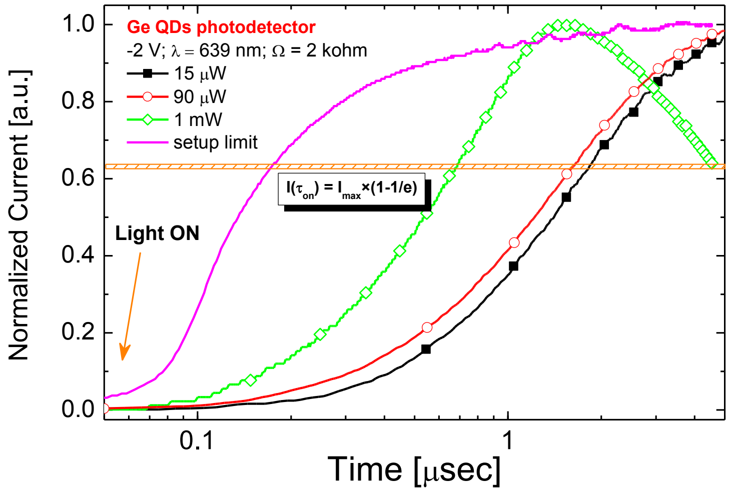

**Figure 4.13:** Normalized photocurrent response time curves of MOS PDs with a QD-layer of ~3 nm-diameter Ge QDs for different excitation powers. The continuous magenta line represents the baseline system response (~0.1 $\mu s$ response time) obtained by measuring the modulated laser beam using a commercial Si photodiode with nanosecond response time.

Based on the presented results, assuming one of the main delays comes from the transit time due to the percolative-hopping conduction of electrons through the QD layer (which to first approximation is proportional to $W_{QD}^2$), faster response times can be achieved by reducing the QD layer thickness. Therefore, we fabricated MIS PDs with different QD-layer thicknesses, similarly as previously described.

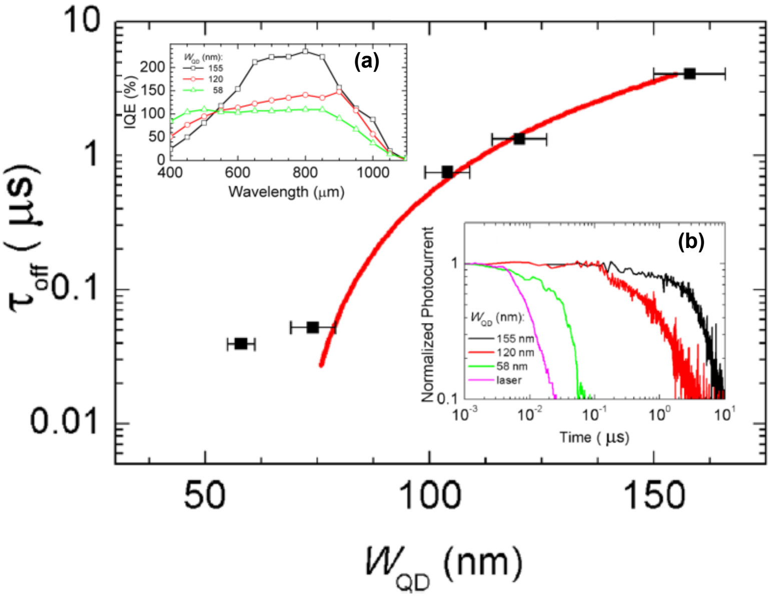

**Figure 4.14:** Experimental values of $\tau_{off}$ of Ge QDs PDs as a function of the thickness $W_{QD}$ of the QD-layer (solid squares) and fit of the experimental data showing a quadratic dependence (red line). Insets shows (a) spectral IQE measured at -2V and (b) time-resolved normalized photocurrent response measured at -2V bias and 2 mW incident power (using a load resistor with R=50 Ω) for different thicknesses of the QD-layer. Adapted from ref. [56].

The measured spectral IQE curves (at -2V) from some representative devices with thinner active layer are reported in the inset (a) of figure 4.14. We observe that reducing $W_{QD}$ only slightly reduces the internal quantum efficiencies of these devices. Interestingly, for the thinnest device ($W_{QD}$ ~ 60 nm), the IQE is roughly constant to around 100% over a wide wavelength range, from 400–850 nm. On the other hand, the response time ($t_{off}$) of these devices, decreases quickly with $W_{QD}$, as clearly shown in figure 4.14 (b). For example, reducing $W_{QD}$ down to 60 nm reduces $t_{off}$ to ~40 ns, as shown in Figure 4.14, at the cost of a slightly lower performance.

In order to verify that the conduction mechanism is controlled by the drift of electrons by percolative-hopping through the QD-layer, we performed a quadratic fitting of the measured response times with respect to $W_{QD}$, as shown by the red curve in figure 4.14. As is seen from the figure, the fit is reasonably consistent with the measured data except at the lowest $W_{QD}$, where the deviation can be attributed to parasitic capacitance. Indeed, the measured capacitance for the thinnest device is about 260 pF. Given that we are using a load resistor with R=50 Ω, a lower bound to the circuit RC constant is of the order of ~10 ns, i.e., the same order of magnitude of the fastest measured response time. This suggests that an even faster response time can be achieved by reducing the parasitic series resistance and capacitance, the device area, and decreasing $W_{QD}$ even further. There may also be room for improvement in the response time by optimizing the Ge QD size and distribution in the active layer.

Finally, we would like to point out that the bandwidth, $f_{3dB}$, of a photodetector is closely related to the response speed by the relationship: $\tau = 0.35 / f_{3dB}$ [5]. By reducing the active QDs layer thicknesses, we are able to achieve a faster response time as just shown above, and thus we would expect larger bandwidths as well. Therefore, we performed responsivity measurements over a wide modulation frequency range of illumination for these devices, as reported in Figure 4.15. To reduce the RC time delay, we used an R=50 Ω series resistor in the measurement circuit.

As shown in figure 4.15, the responsivity of the all the devices generally decreases as $f$ increases, because of the lower amount of QDs that can be electrically-charged as light impulses become shortened and fastened. However, the different response time exhibited by PDs having QD-layers with different thickness clearly affects also the frequency dependence of the responsivity. In fact, while the responsivity of the $W_{QD}$=155 nm PD begins to fall off already after ~$10^4$ Hz, for thinner $W_{QD}$ devices the roll-off can be pushed to higher frequencies as the result of the faster rise and decay times. Finally, for our thinnest device with $W_{QD}$=58 nm, the responsivity is roughly constant up to operating frequencies of ~$10^7$ Hz.

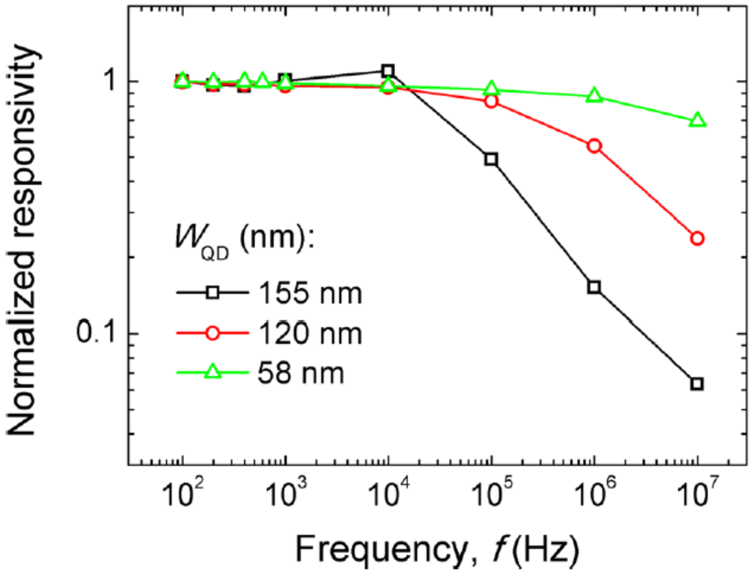

**Figure 4.15:** Normalized responsivity vs. frequency $f$ for devices with $W_{QD}$=155 nm, 120 nm and 58 nm. For this set of measurements, R=50 Ω, $P_{opt}$=1 mW, and V=-2V. From ref. [56].

These results demonstrate that the usage of Ge QDs as active medium in MIS photodetectors allow to achieve high internal quantum efficiency and response times as fast as 40 ns, at low operating voltages of only 2 V. Moreover there is room from improvements by the control of QDs size, amount of charge-traps, thickness of the active layer and PD geometry. These advantages together with the ease of fabrication and low temperature processing, make germanium quantum dots a promising candidate for CMOS-compatible, integrated photodetector applications including fast, low power consumption cameras and integrated biochemical sensors.

## 4.5 Conclusions

In this chapter we investigated the carrier conduction mechanism of prototypal light harvesting devices based on Ge nanostructures. We demonstrated that Ge NS can be effectively used as active absorber and conductive medium in the fabrication of efficient photodetectors. In particular, we studied the current transport characteristics in metal-insulating-semiconductor (MIS) devices employing Ge QW or Ge QDs in the insulating layer, under light illumination and applied bias.

MIS devices using single amorphous Ge QW exhibit a clear net photocurrent which increases with the QW thickness, indicating the key-role in the absorption and photo-carrier extraction played by Ge. Moreover, the quantum efficiency of photo-carrier extraction reaches values as high as 70% at -2V of applied bias, indicating that almost every electron-hole pair generated by light absorption within Ge QW can be effectively collected. Such high performances, together with the chance of bandgap tuning by quantum confinement, demonstrate that amorphous Ge QWs can be profitably used as efficient energy-tunable photo-sensitizer in light detection devices.

When Ge QDs are used as the active layer in MIS photodetectors, much higher performances are achieved. Large photocurrent, with light-ON/OFF ratio as high as $10^2$, are achieved when illuminating the device in the 500 – 1000 nm range. The corresponding internal quantum efficiencies, as high as 1500% for -10V of applied bias and 300% for a low bias of only -2V, reveal the presence of an internal gain mechanism in this type of photodetectors. Such gain is activated by a trapping mechanism of photo-generated holes due to the presence of Ge QDs, which facilitate the further injection of extra-carriers when the device is biased. Moreover, the spectral response strongly depends on the size of QDs and on the amount of hole-traps centers, exhibiting larger photoconductive gains as smaller is the QDs size. In this regard, the QD-layer acts both as a size tunable optical filter for the response of the device and as a selective conductive layer for injected carriers. Finally, we gave evidences on the connection between the photoconductive gain and the lifetime of trapped holes through response time measurements. We found that the response time of PD is fastened with the increasing of the amount of trapped holes (proportional to the incident power) and can be further decreased down to ~40 ns as the active QD-layer is thinned to ~60 nm, with minimal loss in responsivity.

Such results clearly demonstrate that a proper control and exploitation of the structural and optical properties of Ge nanostructures offers great opportunities toward the development of efficient light harvesting devices, giving also large room for improvements for future low cost solar cells.

# References

[1] 2012 Key world energy statistics - International Energy Agency, available at www.iea.org/statistics/.

[2] D. S. Ginley, D. Cahen, *“Fundamentals of Materials for Energy and Environmental Sustainability”*, Cambridge University press (2012).

[3] Z. L. Wang and W. Wu, Angew. Chem. Int. Ed. **51**, 2–24 (2012).

[4] R. Perez, K. Zweibel, T. E..Hoff, Energy Policy, **39,** 7290 (2011).

[5] Simon M. Sze (1981) *“Physics of semiconductor devices”*, 2nd Ed., (John Wiley & Sons, New York, NY)

[6] PV status report 2012, available at http://iet.jrc.ec.europa.eu/sites/default/files/files/documents/events/pvreport-2012-part1.pdf

[7] V. Milnar, Nanotechnology **24**, 042001 (2013).

[8] W. Shockley and H. J. Queisser, J. Appl. Phys. **32**, 510 (1961).

[9] Figure available at National Renewable Energy Laboratory website: http://www.nrel.gov/ncpv/

[10] M. A. Green, K. Emery, D. L. King, Y. Hishikawa, and W. Warta, Prog. Photovolt: Res. Appl.k **14**, 455–461 (2006).

[11] A. J. Nozik, Chemical Physics Letters **457**, 3–11 (2008).

[12] M. C. Beard, K. P. Knutsen, P. Yu, J. M. Luther, Q. Song, W. K. Metzger, R. J. Ellingson, and A. J., Nano Letters **7**, 2506 (2007).

[13] R. D. Schaller , M. Sykora , J. M. Pietryga, and V. I. Klimov, Nano Lett. **6**, 424–429 (2006).

[14] L. A. Padilha , J. T. Stewart , R. L. Sandberg , W. K. Bae , W. Koh , J. M. Pietryga, and V. I. Klimov, Acc. Chem. Res., **46**, 1261-1269 (2013).

[15] M. Miritello, R. Lo Savio, P. Cardile, F. Priolo, Phys. Rev. B **81**, 041411 (2010).

[16] X. Huang, S. Han, W. Huang and X. Liu. Chem. Soc. Rev., **42**, 173—201 (2013).

[17] R. P. Feynman, There's Plenty of Room at the Bottom, Caltech

Engineering and Science, Vol 23:5, February 1960, pp 22-36

[18] M. Daniel and D. Astruc, Chem. Rev., **104**, pp 293–346 (2004).

[19] L. Pavesi, L. Dal Negro, C. Mazzoleni, G. Franzò, F. Priolo, Nature **408**, 440 (2000).

[20] J. Feng , V. S. Siu , A. Roelke , V. Mehta , S. Y. Rhieu , G. Tayhas R. Palmore , and D. Pacifici, Nano Lett., **12**, pp 602–609, (2012).

[21] M. Ferrari, Nature Reviews Cancer **5**, 161-171 (2005)

[22] G. Conibeer, Mater. Today **10,** 11 (2007).

[23] Nozik A.J., Nano Lett., **10**,2735-2741 (2010).

[24] P. W. Flanigan, A. E. Ostfeld, N. G. Serrino, Z. Ye, and D. Pacifici, Optics Express, **21**, pp. 2757-2776 (2013).

[25] Peter Y. Yu and Manuel Cardona, *“Fundamentals of Semiconductors”*, 4th Ed. Srpinger

[26] E. G. Barbagiovanni, “*Influence of Quantum Dot Structure on the Optical Properties of Group IV Materials Fabricated by Ion Implantation”*, PhD Thesis, The University of Western Ontario London, Canada (2012).

[27] G. Conibeer, M. Green, E. Cho, D. Konig, Y. Cho, T. Fangsuwannarak, G. Scardera, E. Pink, Y. Huang, T. Puzzer, S. Huang, D. Song, C. Flynn, S. Park, X. Hao, and D. Mansfield, Thin Solid Films **516**, 6748 (2008).

[28] M. A. Green, Physica E, **14**, 65 (2002)

[29] E.G. Barbagiovanni, D.J. Lockwood, P.J. Simpson, L.V. Goncharova, J. Appl. Phys. **111**, 034307 (2012).

[30] Martì A, Antolìn E, Stanley CR, Farmer CD, Lòpez N, Dìaz P, Cànovas E, Linares PG, Luque A, Phys. Rev. Lett., **97**, 247701 (2006)

[31] Chu-Wei Jiang and Martin A. Green, J. Appl. Phys. **99**, 114902 (2006)

[32] O. L. Lazarenkova and A. A. Balandin, J. Appl. Phys., **89**, 5509 (2001)

[33] W. Hu, M. Igarashi, M. Lee, Y. Li and S. Samukawa, Nanotechnology **24**, 265401 (2013).

[34] V. A. Belyakov, V. A. Burdov, R. Lockwood, and A.Meldrum, Advances in Optical Technologies, vol. 2008, Article ID 279502, 32 pages, 2008. doi:10.1155/2008/279502

[35] J. Bardeen and W. Brattain, Phys. Rev., **75**, pp.1208 (1949).

[36] C. Claeys and E. Simoen (2007): *“Germanium-Based Technologies: From Materials to Devices”*, (Elsevier, Amsterdam).

[37] K. Brunner, Rep. Prog. Phys. **65**, 27–72, (2002)

[38] J. Liu, M. Beals, A. Pomerene, S. Bernardis, R. Sun, J. Cheng, L. C. Kimerling and J. Michel, Nat. Photonics, **2**: 433-437 (2008).

[39] J. Liu, X. Sun, R. Camacho-Aguilera, L. C. Kimerling, and J. Michel, Opt. Lett., **35**, 679-681 (2010).

[40] J. Michel, J. Liu and L. C. Kimerling, Nat. Photonics **4**, 527 (2010)

[41] D. Ahn, C. Hong, J. Liu, W. Giziewicz, M. Beals, L. C. Kimerling, J. Michel, J. Chen and F. X. Kärtner, Opt. Express, **15**, 3916 (2007).

[42] Guter, W. ; Schone, Jan ; Philipps, S.P. ; Steiner, Marc et al., Appl. Phys. Lett. **94**, 223504 (2009).

[43] Y.M. Niquet, G. Allan, C. Delerue, M. Lannoo, Appl. Phys. Lett. **77**, 1182 (2000).

[44] A. Liu, R. Jones, L. Liao, D. Samara-Rubio, D. Rubin, O. Cohen, R. Nicolaescu and M. Paniccia, Nature **427**, 615–-618 (2004).

[45] D. A. B. Miller, D. S. Chemla, T. C. Damen, A. C. Gossard, W. Wiegmann, T. H. Wood and C. A. Burrus, Phus. Rev. Lett. **53**, 2173 (1984).

[46] Y. Kuo, Y. K. Lee, Y. Ge, S. Ren, J. E. Roth, T. I. Kamins, D. A. B. Miller and J. S. Harris Nature **437,** 1134-1136 (2005).

[47] J. E. Roth, O. Fidaner, R. K. Schaevitz, Y. Kuo, T. Kamins, J. S. Harris, and D. A. B. Miller, Opt. Express **15**, 5851 (2007).

[48] Chu-Hsuan Lin and Chee Wee Liu, Sensors, **10**, 8797-8826 (2010)

[49] B.-C. Hsu, S. T. Chang, T.-C. Chen, P.-S. Kuo, P. S. Chen, Z. Pei, and C. W. Liu, IEEE ELECTRON DEVICE LETTERS, **24**, 318 (2003)

[50] M. Elkurdi, P. Boucaud, S. Sauvage, O. Kermarrec, Y. Campidelli, D. Bensahel, G. Saint-Girons and I. Sagnes, Appl. Phys. Lett., **80**, 509, (2002).

[51] J.M. Shieh, Y.F. Lai, W.X. Ni, H.C. Kuo, C.Y. Fang, J.Y. Huang, C.L. Pan, Appl. Phys. Lett. **90** 051105 (2007).

[52] J. M. Shieh, W.C. Yu, J.Y. Huang, C.K.Wang, B.T. Dai, H.Y. Jhan, C.W.

Hsu, H.C. Kuo, F.L. Yang, C.L. Pan, Appl. Phys. Lett. **94**, 241108 (2009).

[53] S.S. Tseng, I.H. Chen, P.W. Li, Appl. Phys. Lett. **93**, 191112 (2008).

[54] S.S. Tzeng, P.W. Li, Nanotechnology **19**, 235203 (2008).

[55] S. Cosentino, Pei Liu, Son T. Le, S. Lee, D. Paine, A. Zaslavsky, D. Pacifici, S. Mirabella, M. Miritello, I. Crupi, A. Terrasi, Appl. Phys. Lett. **98**, 221107 (2011).

[56] Pei Liu, S. Cosentino, Son T. Le, S. Lee, D. Paine, A. Zaslavsky, D. Pacifici, S. Mirabella, M. Miritello, I. Crupi, A. Terrasi, J. Appl. Phys. **112,** 083103 (2012).

[57] E. Cho, S. Park, X. Hao, D. Song, G. Conibeer, S. Park and M. A Green, Nanotechnology **19**, 245201 (2008).

[58] T. Tayagaki, N. Usami, W. Pan, Y. Hoshi, K Ooi and Y- Kanemitsu, Appl. Phys. Lett. **101**, 133905 (2012).

[59] T. Tayagaki, Y. Hoshi and N. Usami, Nature scientific reports, **3**, 2703 (2013).

[60] N. Usami, W. Pan, T. Tayagaki, S. Chu, J. Li, T. Feng, Y. Hoshi and T. Kiguchi, Nanotechnology **23**, 185401 (2012).

[61] X. Lan et al., Adv. Mater., **25**, 1769–1773 (2013).

[62] E. H. Sargent, Nature photonics **6**, 133 , (2012).

[63] R. Yu, Q. Lin, S. Leung, Z. Fan, Nano Energy **1**, 57–72, (2012).

[64] C. Liu and U. R. Kortshagen, Nanoscale Res. Lett. **5**, 1253 (2010).

[65] J. Yun, Y. C. Park, J. Kim, H.-J. Lee, W. A. Anderson and J. Park, Nanoscale Research Letters, **6**, 287 (2011).

[66] C.Y. Liu, Z.C. Holman, U. Kortshagen, Nano Lett. **9**, 449 (2009).

[67] F. Zhang, B. Sun, T, Song, X. Zhu and S. Lee, Chem. Mater., **23**, 2084 (2011).

[68] Z. C. Holman, *“Germanium Nanocrystal Solar Cells”*, Ph.D. thesis, University of Minnesota (2010).

[69] F. Bassani, and G. Pastori Parravicini (1975) *“Electronic States and Optical Transitions in Solids”*, Ed. R.A. Ballinger, (Pergamon Press, Oxford).

[70] M. S. Dresselaus (1999), *“Solid State Physics – Part II – Optical*

*Properties of Solids"*, Lecture Notes Part 2. Available at: http://web.mit.edu/course/6/6.732/www/6.732-pt2.pdf

[71] A.G. Cullis, L.T. Canham, P.D.J. Calcott, J. Appl. Phys. **82**, 909 (1997).

[72] J. Faist, F. Capasso, C. Sirtori, D. L. Sivco, A. L. Hutchinson and A. Y. Cho, Nature, **387**, 777 (1997).

[73] J. S. Biteen, D. Pacifici, N. S. Lewis H. A. Atwater, Nano Lett., **5**, 1768 (2005).

[74] J. Belessa, V. Voliotis, R. Geousson, X. L. Wang, M. Ogura and H. Matsuhata, Phys. Rev. B, **58**, 9933, (1998).

[75] Y.H. Kuo and Y.S. Li, Phys. Rev. B, **79**, 245328 (2009).

[76] Y.H. Kuo and Y.S. Li, Appl. Phys. Lett. **94**, 121101 (2009).

[77] J. Tauc, *"Amorphous and liquid semiconductors"*, Ed. J. Tauc (London and New York: Plenum Press), p.175 (1974).

[78] S. Knief, W. von Niessen, Phys. Rev. B., **59**, 12940-12946 (1999).

[79] J. Tauc, T. Grigorovivi and A. Vancu, phys. stat. sol. **15**, 627 (1966)

[80] P. Hapala, K. Kusova, I. Pelant, and Pavel Jelınek, Phys. Rev. B **87**, 195420 (2013)

[81] Bittar A, Williams G. W. M. , Trodahl H.J., Phys. A, **157**, 411 (1987).

[82] J. A. Thornton, J. Vac. Sci. Technology **11**, 666 (1974).

[83] S. Cosentino, M. Miritello, I. Crupi, G. Nicotra, F. Simone, C. Spinella, A. Terrasi and S. Mirabella, Nanoscale Res. Lett., **8**, 128 (2013).

[84] Mirabella S, Agosta R, Franzò G, Crupi I, Miritello M, Lo Savio R, Di Stefano MA, Di Marco S, Simone F, Terrasi A, J. Appl. Phys. **106**, 103505 (2009).

[85] L. J. Pilione, K. Vedam, J. E. Yehoda, R. Messier, P. J. McMarr, Phys. Rev. B **35**, 9368 (1987).

[86] Röbner, G. Isella, and H. von Känel, Appl. Phys. Lett. **82**, 754 (2003).

[87] T. Takagahara and K. Takeda, Phys. Rev. B **46**, 15578 (1992).

[88] G. D. Sanders and Y. C. Chang, Phys. Rev B **31**, 6892, (1985).

[89] E. Gatti, E. Grilli, M. Guzzi, D. Chrastina, G. Isella, and H. von Känel, Appl. Phys. Lett. **98**, 031106 (2011).

[90] S. Takeoka, M. Fuji, S. Hayashi and K. Yamamoto, Phys. Rev. B **58**, 7921 (1998).

[91] Zacharias M, Fauchet PM, Appl. Phys. Lett., **71**, 380, (1997).

[92] C. Bostedt, T. van Buuren, T. M. Willey, N. Franco, L. J. Terminello, C. Heske, T. Moller, Appl. Phys. Lett., **84**, 4056 (2004).

[93] C. W. Teng, J. F. Muth, R. M. Kolbas, K. M. Hassan, A. K. Sharma, A. Kvit, and J. Narayan, Appl. Phys. Lett. **76**, 43 (2000).

[94] G. H. Shih, C. G. Allen, and B. G. Potter, Jr., Nanotechnology **23**, 075203 (2012).

[95] Y. Maeda, N. Tsukamoto, Y. Yazawa, Y. Kanemitsu, and Y. Masumoto, Appl. Phys. Lett. **59**, 3168 (1991).

[96] W. K. Choi, Y. W. Ho, S. P. Ng, and V. Ng, J. Appl. Phys., **89**, 2168 (2001).

[97] S. Mirabella, S. Cosentino, A. Gentile, G. Nicotra, N. Piluso, L. V. Mercaldo, F. Simone, C. Spinella, and A. Terrasi, Appl. Phys. Lett., **101**, 011911 (2012).

[98] S. Lee, S. Huang, G. Conibeer and M. Green, Journal of Crystal Growth, **383**, 36 (2013).

[99] C. Uhrenfeldt, J. Chevallier, A. N. Larsen, and B. B. Nielsen, J. Appl. Phys. **109**, 094314 (2011).

[100] S. Mirabella, S. Cosentino, M. Failla, M. Miritello, G. Nicotra, F. Simone, C. Spinella, G. Franzò, and A. Terrasi., Appl. Phys. Lett. **102**, 193105 (2013).

[101] K. Das, M. L. N. Goswami, A. Dhar, B. K. Mathur and S. K. Ray Nanotechnology **18**, 175301 (2007).

[102] Cosentino S., Mirabella S., Miritello M., Nicotra G., Lo Savio R., Simone F., Spinella C., Terrasi A., Nanoscale Res. Lett., **6**, 135, (2011).

[103] L. A. Nesbit, Appl. Phys. Lett., **46,** 38 (1985).

[104] W. Skorupa, L. REbohle, T. Gebel, Appl. Phys. A **76**, 1049 (2003).

[105] A. La Magna, G. Nicotra, C. Bongiorno, C. Spinella, M. G. Grimaldi E. Rimini, L. Caristia and S. Coffa, Appl. Phys. Lett. **90**, 183101 (2007).

[106] Mayer M: SIMNRA user's guide, report IPP 9/113 Garching: Max-Planck-Institut für Plasmaphysik; 1997.

[107] Franzò G, Miritello M, Boninelli S, Lo Savio R, Grimaldi MG, Priolo F,

Iacona F, Nicotra G, Spinella C, Coffa S, J. Appl. Phys., **104**, 094306 (2008).

[108] Skov Jensen J, Leervad Ledersen TP, Pereira R, Chevallier J, Lundsgaard Hansen J, Bech Nielsen B, Nylandsted Larsen A., Appl. Phys. A, **83**, 41 (2006).

[109] H. G. Chew, W. K. Choi, Y. L. Foo, F. Zheng, W. K. Chim, Z. J. Voon, K. C. Seow, E. A. Fitzgerald, and D. M. Y. Lai, Nanotechnology **17**, 1964–1968 (2006).

[110] Tognini P, Andreani LC, Geddo M, Stella A, Cheyssac P, Kofman R, Migliori A., Phys Rev B **53**, 6992, (1996).

[111] Nae-Man Park, Chel-Jong Choi, Tae-Yeon Seong, and Seong-Ju Park, Phys. Rev. Lett., **86**, 1355 (2001).

[112] R. Guerra and S. Ossicini, Phys. Rev. B **87**, 165441 (2013).

[113] K. Kusova, L. Ondic, E. Klimesova, K. Herynkova, I. Pelant, S. Danis, J. Valenta, M. Gallart, M. Ziegler, B. Honerlage and P. Gilliot, Appl. Phys. Lett. **101**, 143101 (2012).

[114] G. Allan and C. Delerue, Phys. Rev. B **75**, 195311 (2007).

[115] R. Baer and E. Rabani, J. Chem. Phys. **128,** 184710 (2008).

[116] F. Priolo, G. Franzò, D. Pacifici, V. Vinciguerra, F. Iacona, and A. Irrera, J. Appl. Phys. **89**, 264 (2001).

[117] R. Guerra, I. Marri, R. Magri, L. Martin-Samos, O. Pulci, E. Degoli and S. Ossicini, Phys. Rev. B **79**, 155320 (2009).

[118] J. F. Ziegler, J. P. Biersack, and U. Littmark, *"Stopping and Ranges of Ions in Matter"* (Pergamon, New York, 1984), Vol. 1.

[119] S. Lee, S. Huang, G. Conibeer, and M. A. Green, Energy Proc. **10**, 20 (2011).

[120] H. Schmidt, U. Geckle, and M. Burns, Phys. Rev. B **74**, 045203 (2006).

[121] J. K. Bording and J. Taftø, Phys. Rev. B **62**, 8098 (2000).

[122] S. Halas and T. Durakiewicz, J. Phys.: Condens. Matter **10**, 10815 (1998).

[123] J. Robertson, J. Vac. Sci. Technol. B **18**, 1785 (2000).

[124] B.L. Yang, P.T. Lai, H. Wong, Microelectronics Reliability **44,** 709

(2004) .

[125] B. H. Koh, E. W. H. Kan, W. K. Chim, W. K. Choi, D. A. Antoniadis and E. A. Fitzgerald, J. Appl. Phys. **97**, 124305 (2005).

[126] M. Ershov, V. Ryzhii, C. Hamaguchi, Appl. Phys. Lett. **67,** 3147 (1995).

[127] V. Letov, M. Ershov, S.G. Matsik, A.G.U. Perera, H.C. Liu, Z.R. Wasilewski, M. Buchanan, Appl. Phys. Lett. **79**, 2094 (2001).

[128] S. K. Zhang, W. B. Wang, F. Yun, L. He, H. Morkoç, X. Zhou, M. Tamargo and R. R. Alfano, Appl. Phys. Lett. **81**, 4862 (2002).

[129] S. Cosentino, S. Mirabella, Pei Liu, Son T. Le, M. Miritello, S. Lee, I. Crupi, G. Nicotra, C. Spinella, D. Paine, A. Terrasi, A. Zaslavsky, D. Pacifici, Thin Solid Films **548**, 551–555 (2013).

[130] G. Konstantatos and E. H. Sargent, Nature Nanotechnology **5**, 391 (2010) .

# List of Publications

This thesis is based on the following publications:

- **S. Cosentino**, S. Mirabella, M. Miritello, G. Nicotra, R. Lo Savio, F. Simone, C. Spinella, A. Terrasi, ***"The role of the surfaces in the photon absorption in Ge nanoclusters embedded in silica"***, *Nanoscale Research Letters* **6**, 135 (2011).
- **S. Cosentino**, Pei Liu, Son T. Le, S. Lee, D. Paine, A. Zaslavsky, S. Mirabella, M. Miritello, I. Crupi, A. Terrasi and D. Pacifici, ***"High-efficiency silicon-compatible photodetectors based on Ge quantum dots"***, *Applied Physics Letters* **98**, 221107 (2011).
- S. Mirabella, **S. Cosentino**, A. Gentile, G. Nicotra, N. Piluso, L. V. Mercaldo, F. Simone, C. Spinella, and A. Terrasi, ***"Matrix role in Ge nanoclusters embedded in $Si_3N_4$ or $SiO_2$"***, *Appl. Phys. Lett*. **101**, 011911 (2012).
- Pei Liu, **S. Cosentino**, Son T. Le, S. Lee, D. Paine, A. Zaslavsky, D. Pacifici, S. Mirabella, M. Miritello, I. Crupi, A. Terrasi – ***"Transient photoresponse and incident power dependence of high-efficiency germanium quantum dot photodetectors"***, *J. Appl. Phys.* **112**, 083103 (2012).
- **S. Cosentino**, M. Miritello, I. Crupi, G. Nicotra, F. Simone, C. Spinella, A. Terrasi and S. Mirabella, ***"Room-temperature efficient light detection by amorphous Ge quantum wells"***, *Nanoscale Research Letters* 2013, **8**, 128, (2013).
- S. Mirabella, **S. Cosentino**, M. Failla, M. Miritello, G. Nicotra, F. Simone, C. Spinella, G. Franzò, and A. Terrasi, ***"Light absorption enhancement in closely packed Ge quantum dots"***, *Appl. Phys. Lett*. **102**, 193105 (2013).

- **S. Cosentino**, S. Mirabella, Pei Liu, Son T. Le, M. Miritello, S. Lee, I. Crupi, G. Nicotra, C. Spinella, D. Paine, A. Terrasi, A. Zaslavsky, and D. Pacifici, *“**Role of Ge nanoclusters in the performance of Ge-based photodetectors**“*, *Thin Solid Films* **548**, 551–555 (2013).

- **Salvatore Cosentino**, Emel Sungur Ozen, Rosario Raciti, Antonio M. Mio, Giuseppe Nicotra, Francesca Simone, Rasit Turan, Antonio Terrasi, Atilla Aydinli, Salvo Mirabella, ***“Light harvesting with Ge quantum dots embedded in $SiO_2$ or $Si_3N_4$”*** (under review).

**BOOK CHAPTER:**

- Antonio Terrasi, **Salvatore Cosentino**, Isodiana Crupi, Salvo Mirabella, ***“Ge nanostructures for harvesting and detection of light.”***, chapter 8 of the book: **"Nanotechnology and Photovoltaic Devices: Light Energy Harvesting with Group-IV Nanostructures” -** Eds. J. Valenta and S. Mirabella - Pan Stanford Publishing (in press)

**OTHER PUBLICATIONS:**

- **S. Cosentino,** S. Knebel, S. Mirabella, M. Miritello, S. Gibilisco, F. Simone, A. Terrasi, H. Bracht and G. Wilde, *“**Light Absorption in Ge nanoclusters embedded in $SiO_2$: comparison between magnetron sputtering and sol-gel synthesis**“*, *Applied Physics A* (in press) - DOI 10.1007/s00339-013-8101-9

- P. Liu, S.T. Le, S. Lee, D. Paine, A. Zaslavsky, D. Pacifici, **S. Cosentino**, S. Mirabella, M. Miritello, I. Crupi, A. Terrasi, ***“Fast, high-efficiency Germanium quantum dot photodetectors”***, Lester Eastman Conference on High Performance Devices (LEC), 2012

- S. Mirabella, **S. Cosentino** and A. Terrasi, ***"Synthesis and Light Absorption Mechanism in Si or Ge Nanoclusters for Photovoltaics Applications"***, Solid State Phenomena, Vol. 205-206, pp. 465-474, 2014.

## Curriculum Vitae

Salvatore Cosentino was born on 24th of October 1984 in Giarre (Catania). He attained his Master Degree in Physics with full marks (110/110 cum laude) from the University of Catania in 2010. In November 2010 he started the Ph.D. course in Science and Technology of Materials at the University of Catania. He is currently working under the supervision of Prof. Antonio Terrasi and Dr. Salvo Mirabella at the Physics and Astronomy Department of the University of Catania and at the CNR-IMM MATIS group of Catania. The main scientific interests are focused on the investigation of group IV nanostructures for optoelectronics and PV applications. During his Ph.D. project he has been actively involved in several scientific collaborations with: CNR-IMM, Brown University, Bilkent University, Munster University and Varian Semiconductor Materials. He spent part of his research activity at Brown University (Providence, USA), under the supervision of Prof. D. Pacifici and at Bilkent University (Ankara, Turkey), under the supervision of Prof. A. Aydinli. He also attended the 2rd and 3rd SPIRIT (Support Of Public And Industrial Research Using Ion Beam Technology) tutorials on *"Ion Beam Surface Analysis"* and *"High Resolution Depth Profile"* held respectively in Zurich and Paris in 2011 and participated to the *47th and 52th Course of the International School of Solid State Physics on "Materials for Renewable Energy",* in 2010 and 2012 respectively. During the Ph.D. course he presented the results of his research activity, giving both oral or poster contributions, at the following international conferences: 2011 E-MRS spring meeting (Nice), 2011 MRS fall meeting (Boston), 2012 E-MRS spring Meeting (Strasbourg), 2012 MRS fall meeting (Boston), 2013 E-MRS spring Meeting (Strasbourg). He won the young scientist award at 2013 E-MRS conference and has been awarded with a grant by the Blanceflor Boncompagni-Ludovisi foundation for his research activity. Salvatore Cosentino is author or co-author of several articles, published in international referred scientific journals and also co-author of a book chapter.

# Acknowledgements

It is not so easy to find the right words to express all my gratitude to the people that I met during this "Ph.D. journey". Some of them have been really important for me, not just from a scientific point of view.

First of all, I'd like to thank my tutor, Prof. Antonio Terrasi. He accompanied me in all my academic career, from my Bachelor degree to this Ph.D. thesis. I am not grateful just for having given me the opportunity to work with him (that is basically what almost every grad. student says about his professor). I am also grateful for his human kindness, his patience and for his numerous advices. Feeling comfortable is the first step to work better and I am sure I did the best choice when I asked to work with him.

My sincere gratitude also goes to Dr. Salvo Mirabella, my supervisor. Actually, I cannot say that he has been just a "traditional" supervisor for me. He always stimulated me with many suggestions and pushed me to get beyond my limits, as a good supervisor has to do, expecting also the best results. However, I am even more grateful for the many opportunities, his numerous fraternal advices and the great support he gave me during these years.

A special thanks goes to Prof. Domenico Pacifici. He literally is one of the most brilliant person that I have ever met in my life. I really admire his passion for science, his dedication to research and his engaging enthusiasm. If all the people put into their work the same passion that Domenico puts, then we would live in a better world. Having the opportunity to work with Domenico has been one of the most formative experience for me.

My gratitude goes also to Prof. Francesco Priolo for the useful scientific discussion and for having involved me in his big group and to Prof. Emanuele Rimini, whose lessons have approached me to the world of material science. Many thanks also to Prof. Maria Grazia Grimaldi and Dr. Lucia Romano for their scientific support in RBS analysis, to Dr. Maria Miritello for her valuable help in sputtering deposition and to Prof. Francesca Simone for her suggestions on optical measurements. A special thanks goes to Dr. Isodiana Crupi for her suggestions on electrical measurements and, not less important, for her kindness and for our friendly discussions. My thanks goes also to Dr. Vittorio Privitera and Dr. Elena Bruno, two examples that human kindness and scientific rigour are not in conflict.

My sincere thanks goes also to Giorgia, Egidio, Paolo, Gabriele and Pietro. It was nice to share these years with you. I wish you all the best from life!

In these years I had the opportunity to work in a very stimulating environment, as MATIS group is. In this context, I had the opportunity to know many different people and everyone of them left me something. For this reason my sincere thanks goes to all of them.

I'll never forget the lab-time I spent at Brown University. Probably, it was the most formative period for me. For this reason a special thanks goes to my lab mates and friends at Brown: Patrick, Jing, Vince, Son and Cosmin and (last, but absolutely not the least) Pei. I learned a lot of things from them. I am particularly grateful also to Prof. Alexander Zaslavsky for the useful discussion and his insightful advices.

My sincere gratitude goes also to Dr. Emanuele Francesco Pecora. He demonstrated a truly friendship with his hospitality, generosity and many suggestions.

During my research activity I had also the opportunity to be involved in a bilateral collaboration between CNR (Italy) and TUBITAK (Turkey) and to know Prof. Rasit Turan from METU university and Prof. Attilla Aydinli from Bilkent University. I thank both them for this opportunity and also Dr. Emel Sungur Ozen and Dr. Serim Ilday for the stimulating scientific discussions and the fruitful research activity concerning PECVD deposition.

At this point, a special thanks goes to my inseparable colleagues and friends: Dario, Gigi, Adriano e Davide. A long time passed since we started our academic life...it has been a pleasure to share this path with you!

To my eternal friends Enrico and Gabriele. Someone says that friends are the family we choose. Your truly friendship has been really indispensable for my personal growth.

A special thought goes to those people that crossed my life and gave me  intense emotions and moments of pure joy and happiness. Thanks to them I had the opportunity to grow up and learn more about myself, becoming the person I am now. Although sometimes our life-paths split, I will keep jealously in my heart all the good times we had together as the most precious treasure.

Alla mia famiglia, per esserci sempre stata.